Magnetic exchange coupling in 3*d* and 4*f* complexes using radical tetrazine-based frameworks

By

Maykon Alves Lemes

Thesis submitted to the Faculty of Graduate and Postdoctoral Studies

University of Ottawa

in partial fulfillment of the requirement for the Ph. D. degree

in the Ottawa-Carleton Chemistry Institute

Abstract

High symmetry and low coordinated single-ion lanthanides have been a successful recipe to design high performance single molecule magnets (SMMs). However, enhancement of the magnetic properties of polymetallic SMMs is an important challenge. Therefore, this thesis describes the use of redox non-innocent tetrazine-based ligands and *d*- and *f*-elements in order to fine-tune the electronic structure of the resulting compounds to promote strong exchange interactions between the spin carriers. As reported in the literature, radical-bridged ligands represent a potential strategy to improve the magnetic properties of polymetallic SMMs. Thus, *chapter one* introduces principal concepts that govern the physical properties of metal complexes containing radical-bridged ligands.

Chapter two describes the magnetic properties of a unique air-stable tetratopic radical-bridged bpymtz$^{\bullet-}$ (3,6-bis(2-pyrimidyl)-1,2,4,5-tetrazine) templating four Ni(II) metal ions. The dc magnetic studies along with DFT calculations reveal strong ferromagnetic exchange coupling between the Ni– bpymtz$^{\bullet-}$ of J = 98 cm^{-1} with a spin ground state of S = 9/2.

Chapter three describes the application of another tetrazine-based ligand, bpytz (3,6-bis(3,5-dimethylpyrazolyl)-1,2,4,5-tetrazine) to probe magnetic exchange interactions in a {Co$^{II}_4$} supramolecular square. The modelling of dc susceptibility data shows significant Co(II) - bpytz$^{\bullet-}$ magnetic coupling of J = - 118 cm^{-1} for a spin ground state S_T = 4. While the non-reduced analog displays weak Co(II)-Co(II) exchange of J = - 0.64 cm^{-1} (S = 0 ground state). Additionally, the radical-radical magnetic exchange contribution was probed with an analogous {Zn$^{II}_4$} square, where a J = -15.9 cm^{-1} was found.

Chapter four extends the application of reduced tetrazine ligands to lanthanide systems. Here we demonstrate that the systematic reduction of the ligand with cobaltacene ($CoCp_2$) led to the formation of a strongly coupled bpytz$^{\bullet-}$–bpytz$^{\bullet-}$ bridging ligand. Magnetic measurements combined with *ab initio* calculations confirm unprecedented intramolecular π-dimerization preventing strong magnetic Dy(III)–bpytz$^{\bullet-}$ communication.

Chapter five describes the synthesis and characterization of $\{Ln^{III}_4\}$ (Ln = Dy, Gd and Lu) where the Ln(III) ions are bridged by peripheral $bpytz^{\bullet-}$. The oxophilicity and high coordination numbers preferred by lanthanides ions lead to the formation of a cubane core made up of metal ions bridged by hydroxy ligands (μ_3-OH^-). Experimental and computational studies were applied to verify the nature and strength of the magnetic interactions between the spin carriers.

Acknowledgements

- First of all, I would like to thank my supervisor Professor Muralee Murugesu for answer that email so fast that made a significant difference in choosing uOttawa for my graduate studies. Not only for this, but mainly for his guidance and mentorship, for all the knowledge and skills transferred, for the countless advices about life, science and how this business works. Thank you for being been an Obi-Wan Kenobi.
- I am grateful for my thesis committee Professor David Bryce and Professor Jaclyn Brusso for their valuable suggestions and advices and for being with me from my comprehensive exam until my thesis defense. I could not choose a better duo for my TAC (Thesis advisory committees). I am also thankful for Professor Melanie Pilkington for her amazing contribution with comments and discussion on my thesis. Finally, Professor Sean Barry for his contribution on my written thesis.
- I would like to thank all the professors and collaborators who made a huge impact in the process of building up my knowledge in the field of coordination chemistry and molecular magnetism. That includes, Professor Rodolphe Clérac, Professor Liviu Ungur, Professor Carine Michel, prof. Steven Hill.
- A special thank to Dr. Bulat Gabidullin for all the efforts measuring my crystals and solving my structures no matter day or time. Bulat, you are the real MVP!
- A special thank for the whole Murugesu group: Gabe, Yixin, Hilarie, Chris, Katie, Paul, Dylan, Tomasz, Riccardo, Fatemah, Irina, Amelie, Jaime, Tom, Becky. Thank you all not only for the good times but also for the help and support. I consider myself a very lucky person for had the opportunity to work with so many talent people.
- A huge thank to my Brazilian family in Ottawa; Jessica, Andrey, Thais, Felipe and Gustavo.
- A special thank to Pablo and the La Maison people for been supportive in our celebrations.

- I could not forget to thank the amazing people here at Ottawa and Quebec. They made a huge difference especially in winter times.
- I thank the Brazilian government and the program Science without boarders (CNPq) who gave me the opportunity to pursuit my graduate studies.
- I would like to thank my friends Aryana, Danilo, Lais, Livia, Carol, Jhonathan, François and my best friend Aurimar.
- Finally, thank you to my family in Brazil for the unlimited love and support. Divina, Edson and Lyvia, I love you all.

Merci! Thank you! Obrigado

Table of contents

Contribution statement

This project would not be successful without the contribution of the excellent team of collaborators along with the management and mentorship of Prof. Muralee Murugesu. Thus, in this thesis all the synthesis described were performed by me with the exception of compounds $[Co^{II}_4(bpytz)_4(CH_3CN)_6(H_2O)_2]\cdot 8(BF_4)\cdot CH_3CN$, $[Co^{II}_4(bpytz^{\bullet-})_4(PhCOO)_4]\cdot(C_2H_5)_2O\cdot(CH_3OH)\cdot 0.5(H_2O)$ and $[Dy^{III}_2(\mu\text{-}bpytz^{-})_2(TMHD)_4]$ which had the contribution of Hilarie Stein and Yixin Zhang, respectively. The magnetic characterization and data analysis of the compounds in Chapters 3 and 4 were performed by me. The crystallography structures were determined by Dr. Ilia Korobkov (Chapter 2), Dr. Bulat Gabidullin (Chapter 3, 4 and 5) and Dr. Koen Robeyns (Chapter 4). In Chapter 2, Gabriel Brunet contributed to magnetic measurements and data analysis. In Chapter 3, Prof. Rodolphe Clérac contributed with magnetic measurements and data analysis. Dr. Liviu Ungur (Chapter 2), Dr. Jani Moilanen (Chapter 4), Dr. Liviu Chibotaru, Dr. Veacheslav Vieru, and Dr. Naoya Iwahara (Chapter 5) contributed with computational calculations (DFT, *ab initio*). EPR measurements were carried out by Prof. Stephen Hill and Dorsa Komijani, while micro-SQUID characterization was performed by Prof. Wolfgang Wernsdofer and Dr. Yanhuan Lan. Finally, Dr. Jamie Frost and Dr. Amélie Pialat had a significant contribution with the magnetic characterization in Chapter 5. The involvement of this group of collaborators to pursue this project resulted in a series of scientific papers in which three of them are presented in this thesis.

Contributions

1. **M. Lemes**, A. Pialat, S. Steinmann, I. Korobkov, C. Michel, M. Murugesu, Study of a novel hepta-coordinated Fe(III) bimetallic complex with an unusual 1,2,4,5-tetrazine-ring opening. *Polyhedron* 108(2016), 163-168.
2. **M. Lemes**, G. Brunet, A. Pialat, L. Ungur, I. Korobkov, M. Murugesu, Strong ferromagnetic Exchange coupling in a $\{Ni^{II}_4\}$ cluster mediated through an air-stable tetrazine-based radical anion. *Chem. Commun*. 53(2017), 8660-8663.
3. **M. Lemes,** F. Magnan, B. Gabidullin, J. Brusso. Impact of nuclearity and topology on the single molecule magnet behaviour of hexaazatrinaphtylene-based cobalt complexes. *Dalton Trans.* 47(2018), 4678-4684.
4. **M. Lemes,** H. Stein, B. Gabidullin, K. Robeyns, R. Clérac, M. Murugesu. Probing magnetic exchange coupling in supramolecular squares based on reducible tetrazine-derived ligands. *Chem. Eur. J.* 24(2018), 4259-4263.
5. **M. Lemes,** H. Stein, B. Gabidullin, S. Steinmann, M. Murugesu. Tetrazine-based ligand transformation driving metal-metal bond and mixed-valent HgI/HgII. *ACS Omega.* 3(2018), 10273-10277.
6. E. Rodrigues, D. Galico, **M. Lemes**, J. Bettini, E. Neto, I. Mazali, M. Murugesu, F. Sigoli. One pot synthesis and systematic study of photophysical, magnetic properties and thermal sensing of α and β-phases $NaLnF_4$ and β-phases core@shell nanoparticles. *New J. Chem.* 42(2018), 13393-13405.
7. G. Brunet, M. Hamwi, **M. Lemes**, B. Gabidullin, M. Murugesu. A tunable lanthanide cubane plataform incorporating air-stable radical ligands for enhanced magnetic communication. *Communication Chemistry*. 1:88 (2018), 1-6.
8. **M. Lemes**, T. Witkowski, H. Stein, B. Gabidullin, M. Murugesu. Nitrogen-rich 1,2,4,5-tetrazine based ligand as a strategy for designing homotopic triple-stranded helicate supramolecular structures. *Manuscript in preparation*.

9. **M. Lemes,** Y. Zhang, J. Moilanen, B. Gabidullin, M. Murugesu. Intramolecular pancake bonding in an unprecedented air-stable {Dy_2} single-molecule magnet. *Manuscript in preparation.*

Authorization statement

The results reported in Chapters 2 and 3 have been published and the authorization to include them in this thesis has been granted from the Royal Society of Chemistry (Chapter 2) and Wiley and Sons (Chapter 3).

Chapter 1
Introduction

1.1. Overview of the role of radical-bridge ligands in coordination chemistry

Ligands are organic molecules that act as Lewis bases capable of binding to one or multiple metal ions (Lewis acids). These structures play a significant role in the design and synthesis of coordination compounds. Such importance stems from the capability of these linkers to create bonds with metal ions that provide exceptional properties due to the electronic rearrangement resulting from the ligand and metal orbital overlap.[1] Among many ligands reported in the literature, radical-bearing ligands have been shown to be a powerful framework for the preparation of new materials. These frameworks belong to a class of redox non-innocent ligands as they access multiple redox states, which allow them to uptake one or more electrons. Such electronic properties contribute to the enhancement of ligand basicity and also to the electronic communication between the metal centers. These essential characteristics make these frameworks applicable in different areas of science such as molecular magnetism, conductivity, and spectroscopy.[2]

1.2. General concepts of magnetism

In order to shed some light on the main physical properties investigated for the radical-based metal complexes in this work, some general concepts that involve magnetism will be qualitatively described in this section.

At the atomic level, the magnetic properties arise from the coupling of the electronic spin and its angular momentum along with the spin-spin interactions. In this way, based on the electronic configuration, the magnetic behaviour of materials can be considered as diamagnetic or paramagnetic.

Diamagnetism is a common type of magnetism found in nature and consist of atoms or materials that contain all electrons paired. In this case, the resultant magnetic moment

is zero and a negative magnetic susceptibility is observed when this material is exposed to an external field. In contrast, paramagnetic systems are composed of unpaired electrons that display positive magnetic susceptibility when in presence of an external field (parallel alignment of the spins with the field).[3]

1.2.1. Magnetic interactions

While at high temperatures the magnetic moment of the spins is randomly orientated (paramagnetic state), at low temperature the interaction of the spins results in three types of interactions which can be described as (Fig. 1.1):[4]

(a) Ferromagnetism: a type of interaction in which the magnetic moments are aligned parallel within the ordered state.

(b) Antiferromagnetism: consist of an interaction in which the magnetic moments are in an antiparallel arrangement.

(c) Ferrimagnetism: magnetic interaction with similar spin arrangement to antiferromagnetic system, however the magnitude of the antiparallel interactions is non-equivalent.

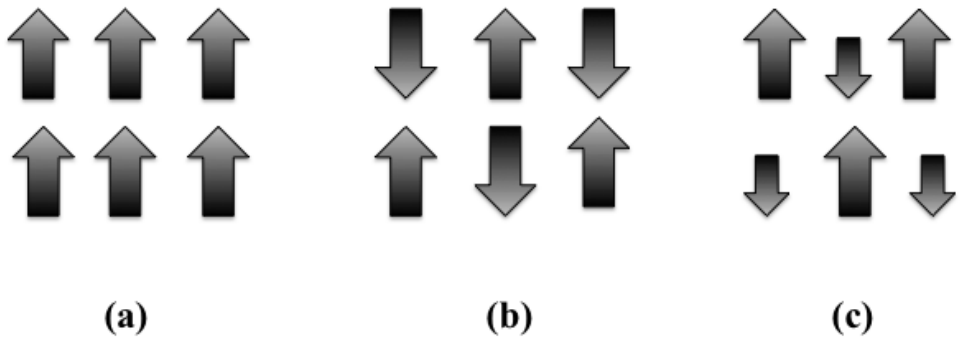

Figure 1.1. Neighbouring magnetic moment interactions of spins. The black arrows indicate the direction and magnitude of the interaction. (a) Ferromagnetic, (b) antiferromagnetic and (c) ferrimagnetic system.

In some special cases, for example, in clusters or metal oxides (ferrites) the spin projections can adopt a different position due to antisymmetric and weak magnetic interactions. Instead of a parallel or antiparallel alignment, the spins can assume a direction in which the angle between them are no longer perpendicular. In this case, the spins are tilted by an angle through their axis, as depicted in Fig. 1.2, which characterizes a spin canting system.[5a,6]

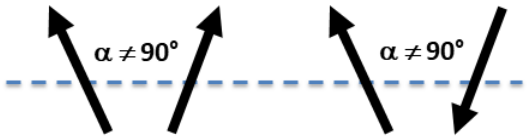

Figure 1.2. Ferromagnetic (left) and antiferromagnetic (right) spin interactions where the spin projections are canted by an angle α within a horizontal axis (dashed blue line).

1.2.2. Magnetic susceptibility

The magnetic response of 1 mol of sample measured under a homogeneous applied field follow the relation described in eq. 1.1.

$$M=\chi*H \tag{1.1}$$

In this equation, M is the magnetization, χ is the molar magnetic susceptibility and H the applied field. Therefore, the magnetic susceptibility can be defined by isolating χ from eq. 1.1.

$$\chi=M/H \tag{1.2}$$

If H is too weak, the magnetic susceptibility is independent and can be obtained straightforward from eq. 1.1.

In the molecular magnetism community, the commonly unit system used for χ is the cgs emu (cm, gram, seconds, electromagnetic unit) instead of SI (International System) with the volume magnetic susceptibility being emu/cm^3 or only cm^3. However, currently the most used is volume magnetic susceptibility per mol of molecules (cm^3 mol^{-1}) or

expressed in terms of the product of the molar susceptibility by the temperature: cm^3 K mol^{-1}. Another unit that is conventional in this field of science is Oersted for applied magnetic field (H) and Bohr magneton (μ_B) for magnetization (M).[5a]

1.2.3. Direct current (dc) magnetometry

In the next four chapters of this thesis, dc susceptibility measurements will be extensively employed to describe the magnetic properties of the complexes. These measurements consist of applying a static dc field followed by the measurement of any change of the magnetic moment of the sample (Here, dc field means the electric current is constant through the coils which results in an invariable and unidirectional magnetic field). The observed change in the magnetic moment is detected by induction as consequence of sample moving up and down throughout the superconducting pickup coils in the SQUID (Superconducting Quantum Interference Device) magnetometer. The reason why this magnetometry method is essential to the studies presented in this thesis is because of the kind of information that can be extracted from the data that can be plotted as (a) magnetic molar susceptibility product (χT *vs.* T) and (b) the field dependence of magnetization (M *vs.* H). In fact, there are other variations of plots which include χ^{-1} *vs.* T and χ *vs.* T (Fig. 1.3 and 1.4). However, since χT *vs.* T is the one established in the molecular magnetism community and represents a better way for the qualitative and quantitative analysis of the magnetic exchange coupling, then such format will be adopted in this thesis.

Essentially, two information can be obtained from the χT *vs.* T plot (Fig. 1.4). First, the qualitative information about the nature of the magnetic exchange coupling of spins at low temperatures. For clarification, in this case, spins mean total spin (S) of each metal center not S_T from the molecule (S = n*1/2; n = number of unpaired electrons). Then, in a plot of χT *vs.* T for paramagnetic samples, at high temperatures (100 – 300 K) the magnetic susceptibility remains constant. At this range of temperature, it is expected higher degrees of freedom for the spins with a minimum or negligible interaction. Therefore, this step consists of a paramagnetic state where the populations of spins are randomly orientated.

As a result, a flat line will be observed (χT constant) in the χT *vs.* T and the constant that describes the magnetic coupling (J) is equal to zero. With the decreasing of the temperature the spins start becoming frozen. Then, the degrees of freedom of the spins decrease and consequently increases the interaction between the metal ions (spins). At this point, two types of spins interactions can be possible: Ferromagnetic or antiferromagnetic. If the interaction of the spins is ferromagnetic, the magnetic moment of the spins is aligned in the same direction (↑↑), and thus, an increase of the χT product is observed ($J > 0$). However, if the interaction is antiferromagnetic the spins are aligned in opposite direction (↑↓) and a decrease of the χT is observed in the plot ($J < 0$). In addition, the χT *vs.* T plot at low temperature can provide some information regarding crystal field effect and zero-field splitting. In this case, the χT at lowest temperature (1.9 K) indicates the spin ground state, or the total spin at lowest level of energy which can allow some conclusion of the electronic structure of the system. Thus, the shape of the curve in the χT *vs.* T results in an important qualitative information regarding the dominant interactions in the system (Fig. 1.4). Finally, quantitative information can also be extracted from the χT *vs.* T plot by fitting the curve using an appropriate spin-Hamiltonian or the Heisenberg-Dirac-Van Vleck (*vide infra*) equation. This approach allows to obtain parameters of the magnetic exchange coupling constant (J) that describe the nature and strength of the spins magnetic communication, along with the g-factor which is the parameter related to the shape of the spins (ratio of the magnetic moment and angular moment) and the zero-field splitting (D).[5,7]

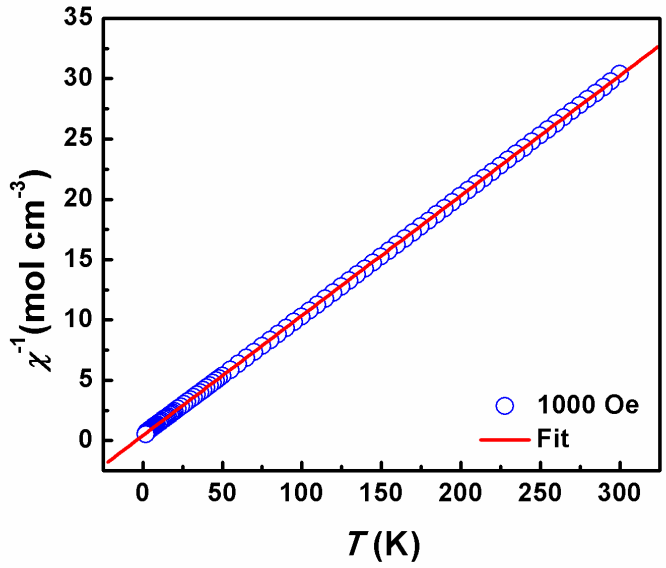

Figure 1.3. Temperature dependence of χ^{-1} of a paramagnetic sample measured under applied field of 1000 Oe. The solid line indicates the fit using the Curie-Weiss law $\chi^{-1} =$ (T–θ)/C. The Weiss parameter θ extracted from this fit determines the dominant magnetic exchange interaction in the system. If $\theta > 0$, ferromagnetic and $\theta < 0$, antiferromagnetic. In this example, $\theta =$ - 2.9 K, then the magnetic exchange interaction is antiferromagnetic (spins aligned antiparallel).

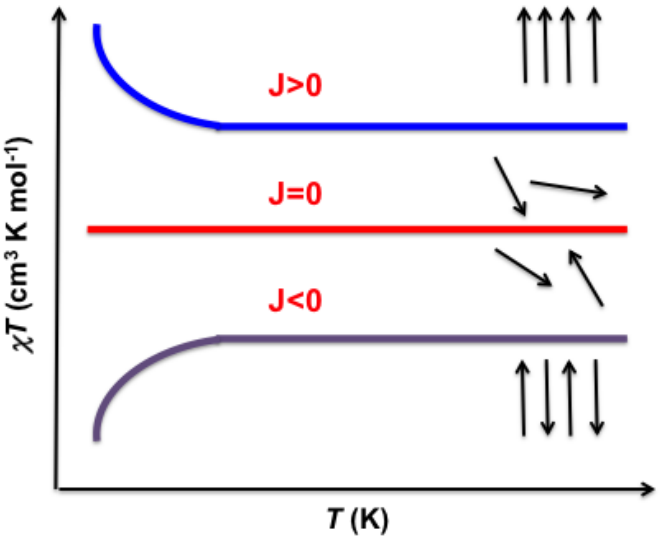

Figure 1.4. Plot of temperature dependence of the molar χT product highlighting the different types of spin interactions. Qualitative observation of ferromagnetic ($J > 0$, blue curve), paramagnetic ($J = 0$, red line) and antiferromagnetic ($J < 0$, purple curve) interactions can be easily verified in the plot of χT *vs.* T at low temperatures.

The field dependence of the magnetization is another form of data obtained from dc measurements and plotted as *M vs*. *H*. This data gives information about the behavior of the sample based on the magnetization with the increasing of the dc field. In fact, such behavior can be described using two plots. First, the *M vs. H*, where the measurements are performed under different temperatures and the shape of the isotherms describe how the sample magnetize at the fixed temperature with the increase of *H*. Here, the terms isotropic and anisotropic characteristic of the systems can be analyzed. Essentially, if the system is isotropic, it will be expected at lower temperature (usually 1.9 K) a rapid magnetization at lower fields followed by saturation at higher fields. To understand this behavior, the Gd(III) which possesses an electronic configuration of $4f^7$ and **L** = 0 (**L** = total orbital angular momentum) will be described as example.

Since all the *f* orbitals of Gd(III) are equally occupied, there is no difference of energy for each spins (degenerate state). Therefore, all 7 electrons will experience same magnetic field and will magnetize simultaneously independently of the level of energy

(temperature). As a result, when the temperature dependence is removed (*M vs*. *H/T*) all the isotherms will overlap (Fig. 1.5). Therefore, such experimental analysis confirm the isotropic nature of Gd(III). Nevertheless, the same observation is not observed for Dy(III) which possesses a significant spin-orbit contribution (**L** = 5, **J** = 15/2; **J** describes the total angular momentum). In this way, all the spins have different energy levels, and then will interact differently with the applied magnetic field. As a result, no saturation will be observed in *M vs. H* at low temperature and the isotherms in *M vs. H/T* will not overlap. Therefore, confirming the anisotropic nature of Dy(III) system.[5]

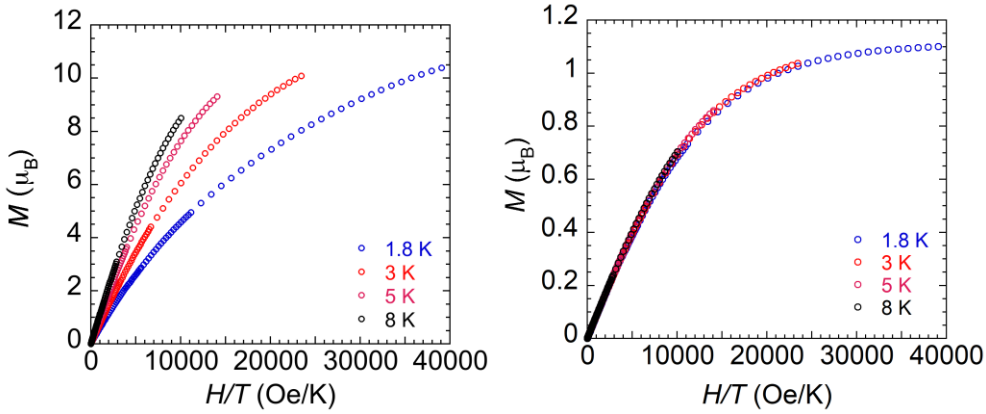

Figure 1.5. Magnetization as a function of HT^{-1} for an anisotropic system (left) and isotropic system (right). Note the isotherm do not overlap and no saturation of magnetization at 1.8 K are observed in the first plot.

1.2.4. Alternating current (ac) magnetometry

A common magnetometry technique to verify slow relaxation of the magnetization or single-molecule magnet behavior is through ac susceptibility measurements. This method consists of applying an alternating ac magnetic field with the simultaneous observation of the change of the magnetic moment of the sample with the change of the orientation of the external ac magnetic field, that is detected by a second coil (in this case, the sample is placed between two coils and an electric current flows in different frequencies resulting in a small oscillation of the magnetic field orientation). In this way, if any delay

is detected in this process, then the sample can hold the magnetization (SMM behavior). Thus, the ac susceptibility can be described as eq. 1.3.

$$\chi_{ac} = \partial M/\partial H \tag{1.3}$$

The small oscillation of the ac field in a range of 0.1 and 1488 Hz results in two components of the χ_{ac}: out-of-phase susceptibility (χ'') and in-phase susceptibility (χ') signal. Here, the out-of-phase component is the dissipative process measured in the sample while, the in-phase component is the slope of *M/H* curve. In general, the analysis of SMM behavior is performed in the χ'' *vs.* ν plot, which is used to study the dynamics of the magnetization of samples. In fact, χ'' can be measured not only in terms of frequency dependence but also temperature and magnetic field. However, the frequency dependency measurements are more popular in this field of science. In this way, these plots provide significant information, such as, the indication of thermal relaxation, where the peaks of the χ'' susceptibility at different temperatures shift towards low frequency. On the other hand, peaks shifting to higher and constant frequencies with the increase of the temperature indicate quantum tunneling of the magnetization (QTM) or long-range relaxation (relaxation due to intermolecular interactions). In terms of quantitative analysis, fitting the maximum of the isotherms in χ'' *vs.* ν plot (where the maximum peak corresponds to $\tau = 1/2\pi\nu$) gives information related to the relaxation process/mechanisms (*vide infra*). Moreover, parameters, such as, the energy barrier (U_{eff}) and relaxation time values (τ) can also be extracted by using the Arrhenius law ($\tau = \tau_0 \, exp \, (U_{eff}/K_B T)$). In this case, the values of τ (maximum peaks) are plotted as function of the inversion of the temperature (T^{-1}) and the data fitted using the Arrhenius equation.

In fact, the τ *vs.* T^{-1} plot displays essential information regarding the dynamic of magnetization. In this plot, the linear behavior of the data at higher temperatures indicates thermal relaxation and it is attributed due to Orbach relaxation processes. However, any deviation from this, it is attributed to other relaxation mechanisms such as QTM, that is observed at low temperatures. Thus, the slope of the plot represents the U_{eff} and from the Arrhenius equation, τ_0 gives the information of the rate of the spin transition, in which must

be in the order of 10^{-6} -10^{-12} to be considered SMM. Therefore, both dc and ac measurements offer a tremendous amount of data/information to give support in the investigation of the magnetic properties of paramagnetic materials at molecular level.[7]

1.2.5. Magnetic exchange coupling in discrete molecules

The magnetic communication between paramagnetic units or spin carriers can occur in different pathways, which include exchange through a diamagnetic bridge (superexchange), through space (dipolar interactions), and direct exchange.[5]

a) Superexchange: The magnetic communication between the metal ions occurs through a diamagnetic bridging ligand. This exchange is the most commonly observed and effective pathway in complexes.
b) Direct Exchange: Here, the magnetic coupling is a consequence of the direct overlap of the magnetic orbitals. As a result, these neighbouring interactions represent the strongest magnetic exchange-coupling pathway.
c) Dipolar interactions: Consist of through space magnetic interactions propagated via weak intermolecular forces, for instance, hydrogen bonds, dipole and van der Waals forces. Although weak, interactions of this nature can be significant at low temperatures.

1.2.6. Spin polarization mechanism

The nature of the magnetic exchange interactions in ferromagnetic complexes can be estimated before performing a magnetic characterization by using the spin polarization approach. This method proposed from the molecular orbital model for organic polyradicals systems suggests that the unpaired electrons in two orthogonal orbitals induce alternant spin density on the intervening atoms. Fig. 1.6 displays the paramagnetic unit (metal ion) inducing polarization of the spin density of atoms in the pathway through the bridging ligand towards to the opposite metal ion.[8]

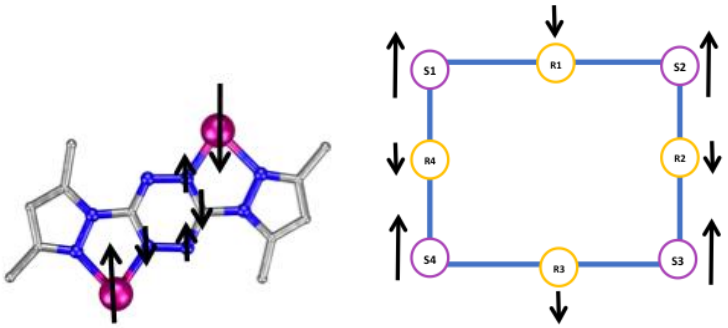

Figure 1.6. Spin polarization method representation (left) between two metal ions separated by a diamagnetic bridging ligand and (right) in a {Co_4} square molecule. The purple circles/spheres indicate Co(II) with $S = 3/2$ and the yellow circles are radical-bridge ligands with $S = ½$.[8,14d]

1.2.7. Spin-orbit coupling

A simple definition of a spin-orbit coupling (SOC) is the interaction of the spin and the angular momentum of the electron. In an atom, the collective interactions of the spin-obit results in the total angular momentum **J** that is described by the sum of the total orbital angular momentum (**L**) and the total spin momentum (**S**). Thus, all possible values of **J** is given by (**L**+**S**), (**L**+**S-1**), … ,|**L-S**|. For transition metals, such interaction contributes to split the energy levels into 2**S**+1 microstate, which is weaker than the ligand field interaction. That can be explained due to the *d*-orbital being superficial, and then the overlap of the *p*-*d* orbitals (ligand-metal) is stronger and quenches the half-filed *d*-orbitals. Thus, spin-orbit coupling ends up being less operational compared to the observed in *f*-orbitals (core orbitals). In the case of lanthanides, the SOC is stronger than crystal field splitting and contributes to the splitting of the ground multiplets.[4]

1.2.8. Modeling of magnetic exchange interactions

In polynuclear complexes the strength of the exchange interaction (the magnitude of *J*) between the paramagnetic units dictates the separation of spin ground state and excited states. For metallic complexes that behave as magnets, the separation between the energy states defines the efficiency of these materials in retaining their magnetization. One approach to evaluate the magnitude of the magnetic exchange coupling is using an appropriate isotropic spin Hamiltonian. Here, the term isotropic means that the interaction is only spin-spin (unidirectional) and other interactions (SOC, for example) are not considered. Thus, this model works well for transition metals since the magnetic *d* orbitals and the *p* orbitals (ligand) overlap quite strongly, and thus a simple Hamiltonian can describe the nature and strength of this communication. In the case of the magnetic coupling of lanthanide metal ions, solving the Hamiltonian becomes more complex due to the significant spin-orbit coupling contribution.[5,7]

Therefore, a pedagogical method or a simple system to describe the application of isotropic Hamiltonian to estimate the nature and strength of a magnetic exchange interaction is using a dinuclear S_1=S_2= ½ system as a model. For instance, a Cu(II) dimer where each ion has a $3d^9$ configuration with one single unpaired electron. Thus, the interaction of two S = 1/2 Cu(II) ions (A and B, Fig. 1.7) separated through a diamagnetic bridge can be formally described in terms of spin operators $\hat{S}_A$ and $\hat{S}_B$ with J being the constant that represents the magnetic exchange coupling between ions **A** and **B** (Fig. 1.7).[5,7]

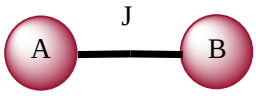

Figure 1.7. Representation of the magnetic exchange coupling between A and B in a system where S_A= S_B= ½.

Then, the phenomenological Hamiltonian using a *-2J* formalism for two interacting metal ions can be written as (Note that in the literature, *J* and 2*J* can be used for the spin-Hamiltonian formula. Here, 2 is just a factor that multiplies *J*):

$$H = -2J\hat{S}_A \cdot \hat{S}_B \quad (1.4)$$

Where the total spin of the system is described as:

$$\hat{S}_T = \hat{S}_A + \hat{S}_B \quad (1.5)$$

Squaring the terms in both sides of eq. 1.5:

$$\hat{S}_T^2 = \hat{S}_A^2 + \hat{S}_B^2 + 2\hat{S}_A \cdot \hat{S}_B \quad (1.6)$$

Rearranging eq.1.6, then eq. 1.7 can be written as:

$$2\hat{S}_A \cdot \hat{S}_B = \hat{S}_T^2 - \hat{S}_A^2 - \hat{S}_B^2 \quad (1.7)$$

Replacing eq. 1.7 in eq. 1.4, the spin Hamiltonian is then given by eq.1.8:

$$H = -2J(\hat{S}_T^2 - \hat{S}_A^2 - \hat{S}_B^2) \quad (1.8)$$

Where the energy of the possible states is associated to S_T, S_A and S_B and given by a modified form of eq. 1.8. This approach takes in consideration the eigenvalues (energies) of the Hamiltonian of form $\hat{S}^2\psi$ for $S(S+1)\psi$ that leads to the zero-order term (E_n^0):

$$E(S_T) = -2J[S_T(S_T + 1) - S_A(S_A + 1) - S_B(S_B + 1)] \; ; \quad (1.9)$$

All the possible S_T, once $\hat{S}_T = \hat{S}_A + \hat{S}_B$, can be found by:

$$S_T = |S_A + S_B| + |S_A + S_B - 1| + \cdots + |S_A - S_B| \quad (1.10)$$

1.2.9. Magnetic anisotropy

Magnetic anisotropy is the preference of the spins to align with the magnetic field, and thus, the magnetic properties of the material depend on the direction of their measurement. However, when a collective of spins in metallic complexes is involved, this definition needs more information to explain the variables that dictate the magnetic anisotropy in paramagnetic compounds. Essentially, there are many types of anisotropy

such as shape anisotropy, exchange anisotropy, magnetocrystalline and so on. However, in the next two paragraphs magnetocrystalline anisotropy will be discussed since this property is intrinsic to the crystal instead of induced anisotropy, which is dominant in the other types.[3]

The physical origin of the magnetocrystalline anisotropy comes from the spin-orbit coupling. Here, the word coupling means interactions. In this way, another possibility to name the magnetic exchange interaction between two nearby spins is spin-spin coupling. Such interaction can be strong depending of the distance and the pathway for the magnetic communication and works to make the spins to align with each other in parallel and antiparallel direction. However, the energy associated to this interaction is isotropic which means that is related only to the angle between the magnetic moment vectors of the spins. Thus, the other directions of the spin axis within the crystal lattice is not taking in account, consequently this kind of interaction does not contribute to the magnetocrystalline anisotropy.[3]

Therefore, another type of coupling is the interaction of the spin of the electron with its orbital momentum (*vide supra*), which in fact, contributes to the magnetocrystalline anisotropy. In this way, if a sample is placed under external applied magnetic field, the spins orientation as well as their orbit will try to reorient with the magnetic field. However, since the orbit is strongly coupled to the crystal lattice, the spin axis will resist to the change of the direction. Consequently, the energy necessary to reorient the spin easy-axis direction (anisotropy energy) it is essentially the energy needed to surpass the spin-orbit coupling. This kind of interaction is considerably weak, where a small applied field (~100 Oe) is enough to change the direction of the spin axis.[3]

For discrete metallic complexes, the local magnetic anisotropy (Local anisotropy = metal ion total spin; Global anisotropy = complex total spin) arises through the zero-field splitting (ZFS). In this case, the ligand field dictates the spatial splitting of the energy states that yields the easy-axis ($D < 0$), where the spins are easily magnetized along of the z axis or easy-plane ($D > 0$), with the spins being easily magnetized along of the x-y plane. Noteworthy, the ZFS is more operational for transition metals complexes. For lanthanides,

SOC and crystal field perturbation command the direction of local anisotropy. While SOC perturbation removes the degeneracy of the spins multiplets, crystal field symmetry interactions guide the orientation of the local magnetic moment. In other words, the spatial distribution (coordination symmetry) of the anionic charges around the electronic structure of the metal ion governs the magnetic anisotropy. For the sake of clarity, ligand field and crystal field have different definitions here. Whereas ligand field is the theory that describes the overlap of the orbitals to form bonding and antibonding orbitals, crystal field is an electrostatic model to describe the interaction of the ligand field with the electronic structure of the metal ion.[3,5]

An example of magnetocrystalline anisotropy in SMMs is the Mn(III) from the famous Mn_{12} complex. In that case, Mn(III) is a $3d^4$ electronic configuration and placed in a tetragonal coordination environment. In such system, a ZFS perturbation splits the $^5A_{2g}$ ground term in $M_s = \pm 2$ microstates, where the $M_s = \pm 1, 0$ states are depopulated at lower temperatures. Thus, in the ground $M_s = \pm 2$ states, the spins alignment preference is along to the *z* axis, therefore resulting in an easy-axis of magnetization along of that axis.[3]

1.3. Single-Molecule Magnets (SMMs)

A general definition of an SMM is a molecule that remains magnetized in the absence of an external magnetic field. The fact that this property is completely molecular in its origin makes these systems promising materials for storing and processing high-density of digital information. This is because a magnetic domain to code information (for example, 0 or 1) could be represented by one single molecule instead of millions of atoms as presented in current materials (hard drives) using iron oxides. The origin of magnetic properties in SMMs arises from the large spin-ground state (*S;* same as S_T) and uniaxial magnetic anisotropy (*D;* the preference of the spins magnetization is along of a single direction, easy-axis (z) or easy-plane (x-y)), which results in an anisotropy energy barrier (*U*). In the literature the definition of *U* is given by $U = |D|S^2$, for integer spins and $U = |D|(S^2 - ¼)$ for half integer spins. One of the well-known models to represent this phenomenon

is the double-well energy diagram, which describes the pathways for magnetization and the relaxation of spins (Fig. 1.8).[9,10]

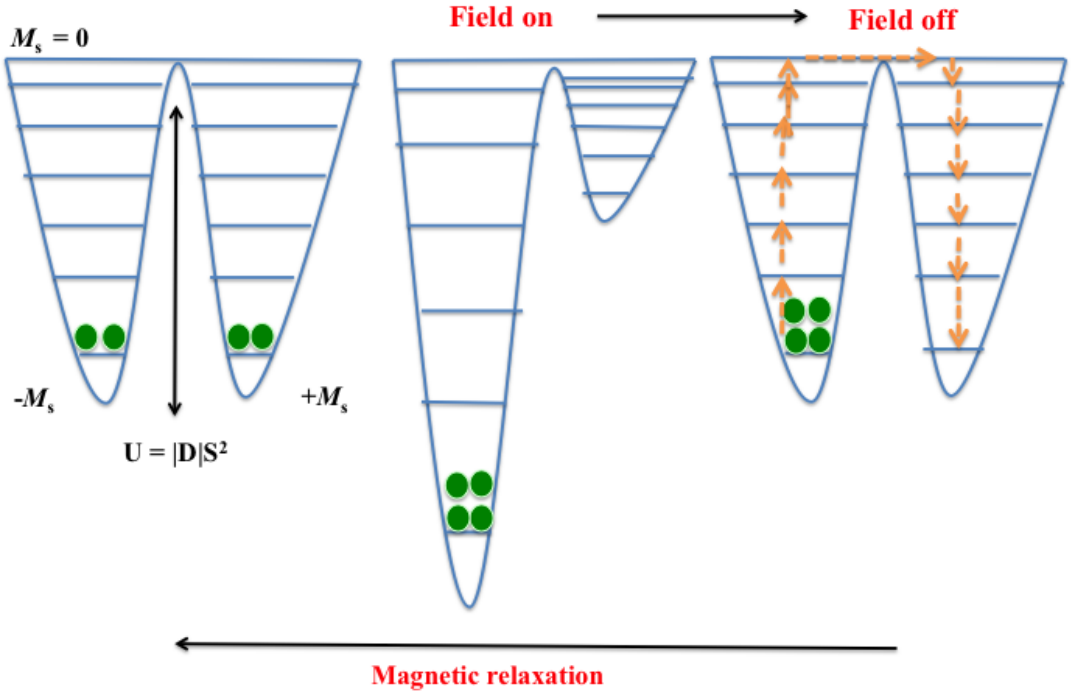

Figure 1.8. Diagram describing the magnetization and relaxation process for SMMs. (Picture inspired from Neese *et al*, 2011).[10a] Each well represent the M_s microstates with $-M_s$ and $+M_s$ being the two possible states for $-S_T$ and $+S_T$. At $H = 0$ the energy states are in equilibrium (left double-well) as the $H \neq 0$ (applied magnetic field) the equilibrium is dislocated towards the magnetized state $-M_s$ (middle double-well). After removing the applied magnetic field, the system will return to the initial equilibrium (right double-well) through magnetic relaxation.

Under an applied magnetic field, the magnetic anisotropy barrier (U) arises as a result of the non-equivalent lifting of the degeneracy of the microstates ($\pm M_s$ states that range from $-S_T \; to \; +S_T$) due to the Zeeman effect. As the external field is removed the states stabilize at the same energy level with the spin population returning to its original state (spin reversal). Such process can occur through different pathways. In Fig. 1.9 (right), an ideal pathway of thermal relaxation it is described. However, in addition to this relaxation process, other mechanisms are possible. For instance, quantum tunnelling of the

magnetization (QTM), direct, Raman and Orbach processes (*vide infra*). Nevertheless, with the exception of QTM, all the other mechanisms occur through a spin-lattice relaxation process.[9,10]

While QTM is a ground state spin reversal through the energy barrier, the spin-lattice process arises when the relaxation is provoked due to elastic perturbation along the crystal lattice, resulting in a destabilization of the magnetized spins (Fig. 1.9). The spins transition through these mechanisms occurs on account of the absorption and/or release of a phonon. Therefore, the direct mechanism is described as a spin transition from the ground microstate to an excited state and is induced by phonon absorption. In the case of Raman and Orbach processes the spin relaxation occurs *via* absorption followed by the release of phonon with the difference that the transition *via* Raman occurs through virtual excited state as depicted in Fig. 1.9 (purple lines).[10]

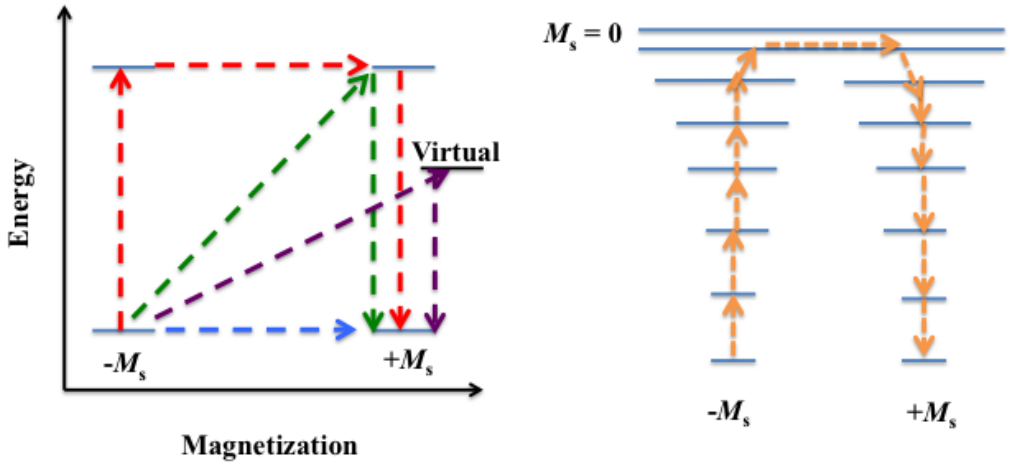

Figure 1.9. Graphical representation of magnetic relaxation mechanisms in SMMs at low-level energy (left). Ideal pathway for the spin reversal (right). Color code: Thermally activated QTM (red horizontal top), ground QTM (blue), Direct (red vertical) Orbach (green), and purple (Raman). (Figure inspired from Murugesu *et al*., 2016).[10b]

1.4. Kramers doublets

In molecular magnetism the time reversal of the angular momentum of spins at a given energy state is a crucial point to assign single-molecule magnet behavior. In fact, the reversal of time under symmetry is one of essential symmetries of nature, since the physics laws that govern that system do not change through the process of $t \rightarrow -t$.[11]

If no external magnetic field is applied, the Hamiltonian that describes the physical properties of a particle is unchanged through the process of time-reversal, then, the energy of the system remains constant. This will only be possible if the wavefunctions that describe the two states are equal and in the same level of energy. However, if the system possesses non-integer spins, these wavefunctions will no longer be equal and the system is doubly degenerate. The result of this operation is known as Kramers degeneracy. In this way, a system with an odd number of unpaired electrons (Kramers ions) placed in a low symmetry environment and under perturbation of the crystal field will split in doublets or Kramers doublets. The same is not expected for metal ions with even number of unpaired electrons (Non-Kramers ions), only in case of specific symmetries or crystal field effects (For example Tb(III) which has $S = 3$). Overall, Kramers's theorem is an approach used in molecular magnetism to explain the time-reversal of the spins (magnetized and demagnetized states) at same level of energy. Under an applied magnetic field this theory is no longer applicable, since the Zeeman effect can mix and lift the degeneracy of the Kramers doublets.[11]

1.5. Broken Symmetry method in density functional theory (DFT) calculations

The most used method to calculate difference of energy is through the broken symmetry (BS) formalism. This method consists of calculating the difference in energy between the high-spin (HS) and low-spin (LS) states and HS and BS states of a system. Essentially, in DFT calculations a HS state is given as magnetic moment of spins $M_S = M_{S1} + M_{S2}$ and low spin $M_S = |M_{S1} - M_{S2}|$. Where, for two coupling total spin $S1$ and $S2$, M is the projection of the spins and S is the total spin that is in function of the spin density (for

a spin only system; no SOC is taken in account). When two magnetic orbitals or sites are related by symmetry, the LS solution in general have lower symmetry, which end up being called broken symmetry (BS) solution. This approach is a result of the inefficiency of the functional exchange correlation to optimize the LS solution by adding insufficient static correlation energy to correct the spin state.[12]

The necessity to properly impose the spin symmetry on BS solution by employing the exchange-coupling constant, from the difference of energy of E_{BS} - E_{HS}, has been proposed to be explained as Ising states. Such a relationship can be written as the following Hamiltonian, that takes in account only the *z* component of the local spins:

$$H_{ising} = -J_{ab}S_{za}S_{zb} \quad (1.11)$$

For a HS and BS being eigenstates, the diagonal elements of the Hamiltonian above represent the energies of these states. Thus, the exchange coupling constant can be obtained from their energies. Additionally, the fact that the spins in eq. 1.11 are related to each magnetic site makes this approach advantageous and applicable to multinuclear systems. Therefore, the exchange coupling constant can be written as:[12]

$$J_{ab} = E_{BS} - E_{HS}/2S_aS_b \quad (1.12)$$

1.6. Radical ligands

In coordination chemistry, the electronic properties of the complexes are mostly associated the electronic structure of the metal center. In this scenario, the ligand is a closed-shell framework with no contribution to the overall charge balance or the complex redox reaction ("innocent ligand"). However, in case when the organic ligand is an open-shell electronic configuration, the formal oxidation number and the electronic properties of the complex are associated due to the feature of the redox active ligand (radical). Thus, for example, in case of an oxi-reduction reaction the organic ligand become the main source for transferring or uptake electrons rather than the metal ion. In this way, the versatility of radical ligands allows such structures of being applicable in different areas of chemistry, such as, catalysis,[13] semiconductors,[14] and magnetism.[15]

In the field of catalysis, the advantage of using such frameworks, as stated by Chirik and Wieghardt,[13b] is the fact that the redox reactions in complexes containing organic radical lead to the oxidation changes in the ligands while the electronic configuration of the metal ion and the complex structure remain stable. In fact, Chirik and co-workers already have demonstrated this with Fe-based complexes containing redox active ligands that assist multi-electron catalysis.[16] In the work reported, the bis(imino)pyridine (PDI) is employed as a non-innocent ligand which displays four accessible oxidation states that participate in the multiple-electron process. The [Fe(PDI)Cl_2] catalyst precursor is reduced by sodium amalgam under N_2 which generates the radical-based catalyst (Fig. 1.10). In this process, the two-electron reduction occurs in the ligand rather than the Fe(II). The resultant [Fe(PDI^{2-})(N_2)$_2$] was used as a hydrosilylation catalyst for inactivated olefins. Notable is the Fe(II) oxidation state as well as the coordination geometry remained constant during the whole process. Another example of significant contribution of redox-active ligands (radical ligand) in catalysis is reported by Cui and Liu.[17] In their report, it is described the application of radical ligands in metal-organic framework (MOF). The strategy adopted by them consist of incorporating (2,2,6,6-tetramethyl-piperidin-1-yl)oxyl (TEMPO) radicals to prepare a multifunctional MOF catalysts (Fig. 1.11). Such approach resulted in a 3D structure with active sites functionalized with TEMPO that allowed oxidation and efficient asymmetric catalysis (conversion up to 98%) in cyanation reaction of alcohols and aldehydes. After the catalysis reaction, the catalyst MOF could be easily recovered and reused without damage in the active sites or its structure.[13]

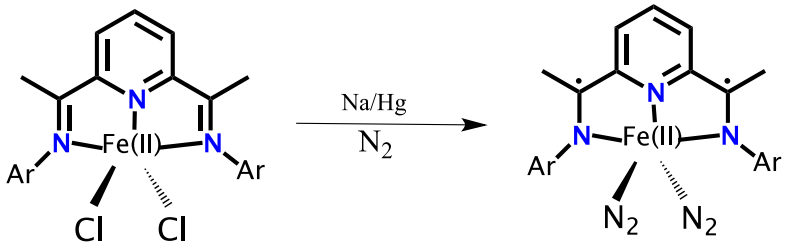

Figure 1.10. Reduction of [Fe(PDI)Cl_2] (left) using sodium amalgam in presence of N_2. Adapted from ref. 16.[16]

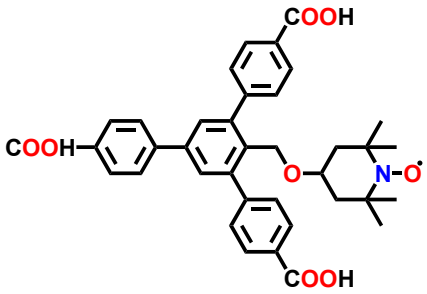

Figure 1.11. Representation of the organic linker functionalized with TEMPO radical utilised to prepare a MOF catalyst described.[17]

Beyond radical ligands in coordination chemistry, the chemistry of free radicals represents also another interesting science that has rendered fascinating studies. In a report presented by Oakley and co-workers,[18] free organic radicals of 1,3,2-dithiazolyl (DTA) derivatives were employed to prepare radical-based materials which show similar magnetic properties to those observed in 3*d* complexes (Fig. 1.12). In such structures, the paramagnetic contribution of the radical molecules is observed as a result of the localized unpair electron and the molecule crystal packing arrangement through the π-stack structures. In this report, it is notable the magnetic bistability presented in the radical polymorph pyrazine-based DTA observed through hysteresis measurements at high temperatures. Another interesting work on free radicals is also reported by Roesky which consist on controlling the stability of free radical containing different main groups substituents.[19] Because of the lack of stability of radical frameworks containing main group elements, Roesky and co-workers have develop the strategy to delocalize the radical spin density over the whole molecule by employing N-heterocyclic carbenes (Fig. 1.12). Such strategy has shown to be successful on isolating stable free radicals beyond preventing dimerization which quenches the electronic properties of paramagnetic radicals. In the following section, employment of radical-based ligands in metallic complexes to achieve/improve single molecule magnets will be discussed.

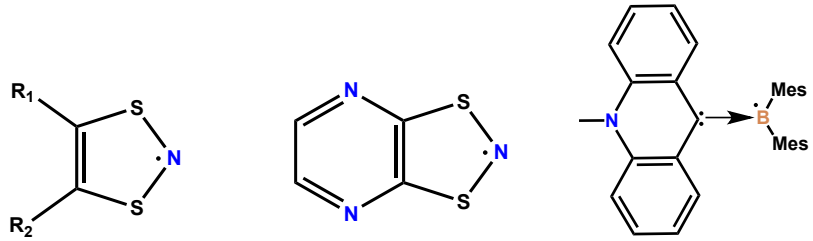

Figure 1.12. Free radical ligands. DTA (left) precursor and PDTA (middle) and an example of carbine stabilizing a main element radical-based molecule (right).[18,19]

1.6.1. Radical ligands in molecular magnetism

The fine-tuning of magnetic properties of SMMs remains a significant challenge for polynuclear compounds. In this way, one of the main problems in such systems is controlling the fast relaxation processes or the quantum tunnelling of magnetization (QTM), which decreases the height of the energy barrier. Thus, one of the synthetic strategies to minimize QTM is using radical-bridging ligands to mediate strong magnetic coupling between the metal ion and the radical. In fact, such strong interaction that arises due to the direct overlap of the metal-radical orbitals promotes a large separation (high values of *J* coupling) between the spin ground state and excited states. Thus, preventing or minimizing the mix of energy levels.[20] In this way, when organic radical ligands are employed to design polymetallic radical-bridged complexes, it is expected higher values of the magnetic exchange coupling constant (*J*), when compared to interactions through a diamagnetic bridging ligand.[20,21]

For 3*d*-based complexes, the magnetic exchange interaction yields coupling constants of substantial magnitude as a result of the direct magnetic exchange interaction of *d* orbitals and the radical spin density. For instance, the work published by Brook *et al.* where the combination of oxoverdazyl radicals (Fig. 1.13) mediate the exchange interaction in a mononuclear complex of Mn(III) and Ni(II) to afford values of J_{Mn} = - 62.5 cm^{-1} and J_{Ni} = +193 cm^{-1}.[22a] In 2013, Harris *et al* reported a record for magnetic exchange coupling for transition metal complexes exhibiting SMM behaviour. The radical-bridged (Fig. 1.14) complex $[Fe^{II}_2 (^{NPh}L^{3-\bullet})]^+$ displays a remarkable exchange coupling constant of

$|J| \geq 900$ cm^{-1} for an $S = 7/2$ ground state and $U_{eff} = 50(1)$ cm^{-1}.[22b] Murray and co-workers described a unique example of a radical ligand contribution on magnetic properties.[23] They reported a hybrid magnetic molecule obtained by reacting $Co^{II}(NO_3)\bullet 6H_2O$ with the nitroxide 4,4-dimethyl-2,2-di(2-pyridyl) oxazolidine *N*-oxide ($L^{\bullet}$) that yields $[Co^{II}(L^{\bullet})_2](NO_3)_2$. The resultant octahedral Co(II) complex displays multiple magnetic properties such as strong intramolecular Co-radical ferromagnetic coupling ($J = +63.8$ cm^{-1}), spin crossover and field induced SMM behaviour. Moreover, it is also observed that the ligand induces Co(II) oxidation which gives $[Co^{III}(L^{-})_2](BPh_4)$. Despite the strong magnetic coupling found in radical-containing transition metal complexes described in the literature, SMMs with energy barriers and blocking temperatures comparable to those 4*f*-SMMs have not been yet observed.[20,24]

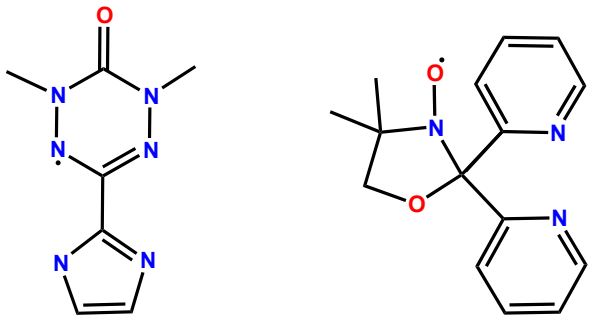

Figure 1.13. Radical ligands oxoverdazyl (left)[15a] and the *N*-oxide ($L^{\bullet}$) (right)[16]

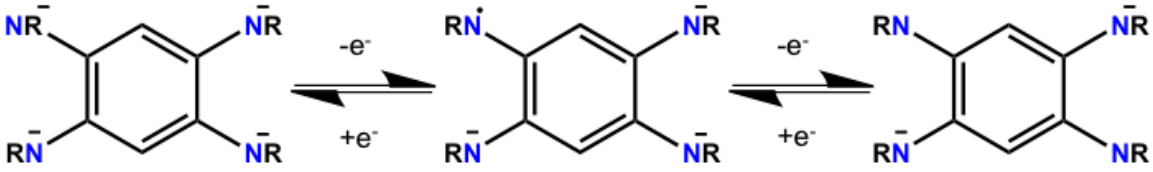

Figure 1.14. Three oxidation state of the benzoquinonoid ligand reported by Harris *et al.*[15b] From the left to right $^{NPh}L^{4-}$, $^{NPh}L^{3-\bullet}$ and $^{NPh}L^{2-}$. In the picture R = Ph.

For lanthanide-based systems, the use of radical ligands has shown substantial impact towards obtaining high performance SMMs or improvement of their magnetic properties. An example of this potential approach is presented by Long *et al.* which

demonstrated a significant increase of the energy barrier and blocking temperature when a reduced $N_2^{3\cdot-}$ bridge is introduced into a dilanthanide complex [K(18-crown-6)(THF)$_2$][{[(Me$_3$Si)$_2$N)$_2$(THF)Tb}$_2$(μ-η^2:η^2 -N$_2$)]. For such system, ac measurements demonstrated that the non-radical complex presents a U_{eff} = 18 cm^{-1} while an improvement is observed in the radical analog with an energy barrier of U_{eff} =123 cm^{-1}. Such results are attributed due to the presence of the radical minimizing zero-field QTM, which favours thermal relaxation at a relatively higher temperature (T_B of 14 K).[25a] Notable is the fitting of the dc susceptibility of the Gd(III) analog which yields a value of J = -27 cm^{-1}. To date, this is the highest coupling constant value reported for Gd-radical magnetic coupling.[25b] In fact, the higher SMM performance expected for lanthanide complexes that contain radical-bridge arises from the diffuse nature of the radical spin density that penetrates the *f*-core orbitals, which are shielded by the 5*s* and 5*p* orbitals, thereby promoting an effective magnetic exchange coupling.[20]

Although the reduced radical ligand $N_2^{3\cdot-}$ has shown to be a powerful framework to promote strong coupling, other examples of organic radical ligands also have shown to be interesting for such application. That is the case of 2,2-bipyrimidyl radical anion (bpym$^{\bullet-}$) containing in complexes of formula, [(Cp*$_2$Ln)$_2$(μ-bpym$^{\bullet}$)]$^+$ (Ln = Gd, Tb, Dy) (Fig. 1.15). In this system, the magnitude of the interaction between the radical anion and lanthanide ions gives a value of J = -10 cm^{-1} (H = -2$JS_{Radical}S_{Gd}$). Even though this interaction appears to be weaker than the previous example, this value is still large for a Gd-Radical interaction. Additionally, the Tb and Dy analogs display slow relaxation of magnetization probed through hysteresis loop and ac susceptibility measurements, where the energy barrier of U_{eff} = 44 cm^{-1} and U_{eff} = 87.8 cm^{-1} were extracted through Arrhenius fit for Tb and Dy respectively.[25c] Thiazyl radical ligands represent also another potential framework employed to design multinuclear lanthanide radical-based complexes. In 2013, Clérac and Preuss reported the supramolecular system [Dy(hfac)$_3$(boaDTDA)]$_2$ (boaDTA = benzoxozal-2'-yl)-1,2,3,5-dithiadiazolyl) which displays SMM behavior attributed due to the individual metal ions yielding a U_{eff} of 71 cm^{-1} (Fig.1.15).[20] Despite thiazyl radical ligand promoting strong exchange coupling in 3*d*-based complexes, here the presence of the radical does not contribute to the magnetic properties.[20c,21h]

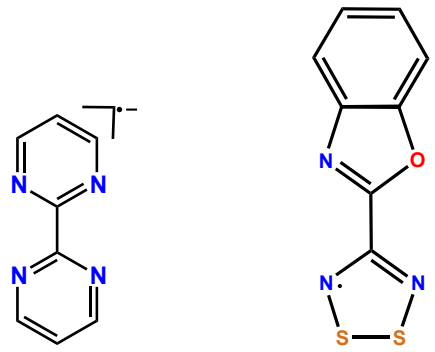

Figure 1.15. bpym (left) and boaDTA (right) radical ligand described in the text.

1.7. Tetrazine-based chelates

Among the many organic chelates used in coordination chemistry, molecules containing tetrazine rings represent an interesting bridging ligand on account of their unique structural and electronic properties. For these reasons, such molecules have been used for many applications, for example, luminescence, photocatalysis, energetic materials and molecular magnetism.[26]

Tetrazine-based frameworks are N-rich molecules that are redox non-innocent ligands; i.e. these ligands do not only coordinate to metals but also contribute to the oxidation state of the complexes. Such molecules are composed of a six-membered ring with four nitrogen atoms at 1,2,4, and 5 positions followed by substituents at positions 3 and 6 (Fig. 1.16). The presence of the heteroatom (nitrogen) in the ring contributes to the ligand electronic properties. In fact, the electronegative nitrogen atoms result in a π-electron deficient ring and a low-lying π* molecular orbital which contributes to reduction at low redox potentials besides significant low-energy transfer absorption, electrical conductivity and mix-valence intermediates. Additionally, their multiple binding sites allow the formation of polynuclear coordination compounds.[26]

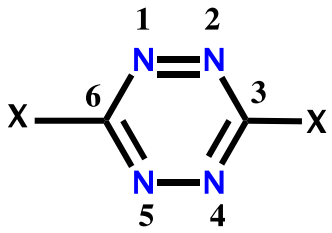

Figure 1.16. Structure of 1,2,4,5-tetrazine where **X** is the substituent (e.g. Aryl, halides)

In this thesis, two tetrazine-based organic molecules (3,6-bis(2-pyrimidyl)-1,2,4,5-tetrazine) (bpymtz) and (3,6-bis(3,5-dimethylpyrazolyl)-1,2,4,5-tetrazine) (bpytz) prepared according to literature procedures,[27] were chosen to pursue this work (Fig. 1.17). The electrochemistry of the ligands was evaluated using cyclic voltammetry (CV), as shown in Fig. 1.18. As observed in the plots (Fig. 1.15), the low redox-potential of -0.79 V and -0.69 V for bpymtz and bpytz, respectively, reinforce their potential to synthesize radical-based complexes.[27]

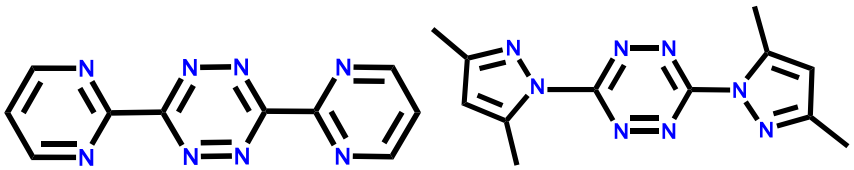

Figure 1.17. Structural representation of the ligands bpymtz (left) and bpytz (right) used in this work.

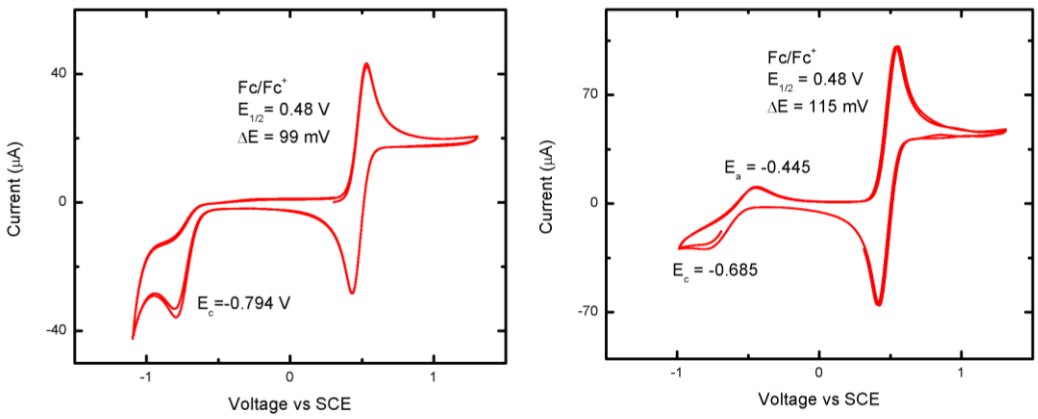

Figure 1.18. Cycle voltammetry for the ligands bpymtz (left) and bpytz (right) in DCM solution.

1.7.1. Tetrazine based ligands in coordination chemistry

The coordination chemistry of tetrazine-based ligands has been initially exploited by Professor Wolfgang Kaim in the 1980s. Using electron rich metal complexes, they have studied the electrochemical properties, showing the influence of such frameworks on the ligand-metal electronic dynamics.[26] Another significant contribution from their work was demonstrating the facile reduction of tetrazines through the discovery of the first air stable tetrazine radical complex $[(Ph_3P)_2Cu(\eta^4,\mu\text{-bptz}^{\bullet-})Cu(PPh_3)_2](BF_4)$; (bptz = 3,6-bis(2-pyridyl)-1,2,4,5-tetrazine).[28] This was the first example without the deliberate addition of a reducing agent, which also was demonstrated later by Patra and co-workers the same tetrazine ring reduction in $[\{(p\text{-cym})Ru^{II}Cl\}_2(\mu\text{-bpytz}^{\bullet-})]^+$.[29]

Another interesting characteristic reported in the literature regarding complexes containing tetrazine ring is the ligand transformation driven by a ring opening, catalyzed by metal ions in presence of water. This phenomenon has been previously observed by Bu *et. al.* where the reaction of Cu(II) with dptz (3,6-di-2-pyridyl-1,2,4,5-tetrazine) results in three complexes with the new bridging ligands bis(2-pyridyl)-1,3,4-oxodiazole (L^1) and *N,N'*-bis(α-hydroxyl-2-pyridyl)ketazine (H_2L^2) generated from a ligand transformation of dptz driven by hydrolysis. In addition, our group has recently reported a ring opening in the resultant complexes from the reactions of Fe(III) and Hg(II) with bpymtz that gave $[Fe^{III}_2(1,2\text{-}L^{2-})(NO_3)_2(H_2O)_4](NO_3)_2$ and $[Hg^{I}_2Hg^{II}_2(L^-)_2(CH_3COO)_4(DMF)_2]\cdot(DMF)$ respectively. Notably, the ligand transformation observed in the mercury complex resulted in a structure with mix of valences Hg(II)/Hg(I) with a central Hg(I)-Hg(I) bond.[30]

In the history of the coordination chemistry of tetrazine-based ligands, it is notable the work of the Dunbar group. By applying these ligands to design supramolecular structures, they have successfully probed the use of the anion-π interactions approach as strategy to promote coordination-driven self-assembly of molecules in different geometries. In 2013,[31a] they demonstrated in detail through a series of physical characterizations that the tetrahedral $[BF_4]^-$ and $[ClO_4]^-$ anions template the assembly of

molecular squares, while the $[SbF_6]^-$, $[AsF_6]^-$ and $[PF_6]^-$ anions template the formation of molecular pentagons. Another significant contribution describes the magnetic properties of the first air-stable tetrazine-based radical-bridged complexes isolated as $\{Cp_2Co\}\{[Dy(tmhd)_3]_2(bptz^{\bullet-})]\}$ and its neutral congener $[Dy(tmhd)_3]_2(bptz)$, in which, both complexes exhibit SMM behaviour under zero applied field. Recently, the Dunbar group was also able to isolate an unprecedented radical-bridged lanthanide metallacycle $[Dy_3(Hfac)_6(bptz^{\bullet-})_3]$. In this work, the magnitude of the magnetic exchange coupling of a delocalized radical with Dy(III) estimated through *ab initio* calculations gives a value of J = -6.62 cm^{-1}.[31] This represents the only study reporting the strength of the magnetic interaction between a tetrazine-radical and lanthanide metal ions.

1.8. Conclusion

Employment of organic radical ligands as a rational design to synthesize polymetallic complexes (3*d* or 4*f* systems) has been shown to be a powerful strategy to enhance magnetic properties in such systems. Therefore, this thesis describes the application of redox non-innocent tetrazine-based ligands to prepare strongly magnetic coupled systems in order to evaluate and understand, at a fundamental level, the contribution of radical frameworks to the physical properties of the resultant complexes. The next two chapters (chapters 2 and 3) will describe the findings of combining the versatile tetrazine-based ligands and transition metal ions. More specifically, it will explore how the ligand topology along with its electronic properties contribute to the fine-tune of the properties of complexes to achieve polymetallic systems with large spin ground state and strong magnetic exchange coupling. Chapters 4 and 5 will describe in detail the synthesis and magnetic properties of polymetallic lanthanide complexes using the bpytz ligand. In chapter 4, crystallographic results along with *ab initio* calculations revealed a dinuclear dysprosium complex showing the first coordination induced intramolecular π-dimerization. Furthermore, field-induced SMM behaviour is observed and its origin attributed to the magnetic anisotropy of each individual metal ion. Finally, magnetic studies including ac/dc susceptibility and hysteresis loop measurements of radical-bridged cubane-like $\{Ln_4\}$ complexes obtained under aerobic condition without reducing agent will be detailed in chapter 5. Overall, the properties of the complexes investigated in this thesis are the results of a series of experimental synthesis and magnetic measurements combined with computational calculations to probe the reduction of the tetrazine-based ligands, magnetic susceptibility, the nature and strength of the magnetic exchange coupling, SMM behavior, and the origin of the SMM behaviour.

References

1 S. F. A. Kettle, *Physical Inorganic Chemistry: A Coordination Chemistry Approach*; Spektrum Academic Publishers. Canada. 1996.

2 (a) W. Kaim, B. Schwederski, *Coord. Chem. Rev*., 2010, **254**, 1580. (b) W. Kaim, *Inorg. Chem*., 2011, **50**, 9752. (c) J. L. Brusso, K. Cvrkalj, A. A. Leitch, R. T. Oakley, R. W. Reed, C. M. Robertson, *J. Am. Chem. Soc*., 2006, **128**, 15080.

3 B. D. Cullity, C. D. Graham, *Introduction to Magnetic Materials*; 2nd ed.; Wiley. IEEE Press. New Jersey. 2009.

4 R. L. Carlin, *Magnetochemistry*; 1st ed.; Spring-Verlag. Germany. 1986.

5 (a) O. Kahn, *Molecular Magnetism*; 1st ed.; VCH Publishers Inc.: New York, 1993. (b) E. Sinn, *Coord. Chem. Rev*., **5**, 1970,313.

6 T. Moriya, in Magnetism, Academic Press, London, 1963,1,85.

7 E. Moreno-Pineda, L. E. Nodaraki, F. Tuna; *Novel Magnetic nanostructures*; 1st ed.; Elsevier; Netherlands, United Kingdom, United States, 2018.

8 (a) V. Â. Ung, A. M. W. C. Thompson, D. A Bardwell, D. Gatteschi, J. C. Jeffery, J. A. McCleverty, F. Totti, M. D. Ward, *Inorg. Chem*., 1997, 36, 3447. (b) F. Lloret, G. De Munno, M. Julve, J. Cano, R. Ruiz, A. Caneschi, *Angew. Chem. Int*. *Ed*., 1998, **37**, 135.

9 D. Gatteschi, O. Kahn, J. S. Miller, F. Palacio, *Magnetic Molecular Materials*; 1st ed.; Spring Science:Italy, 1990.

10 (a) F. Neese, D. A. Pantazis, *Faraday Discuss*, 2011, **148**, 229. (b) J. M. Frost, K. L. M. Harriman, M. Murugesu, *Chem. Sci*., 2016, **7**, 2470. (c) D. N. Woodruff, R. E. P. Winpenny, R. A. Layfield, *Chem. Rev*., 2013, **113**, 5110. (d) S. G. McAdams, A-M. Ariciu, A. K. Kostopoulos, J. P. S. Walsh, F. Tuna, *Coord. Chem. Rev*., 2017, **346**, 216.

11 (a) R. Shankar, *Principles of Quantum mechanics*; 2nd ed.; Springer; New Delhi, India,1994. (b) P. Alonso, J. Martinez, *J. Magn. Reason*., **2015**, 255, 1.

12 (a) I. P. R. Moreira, F. Illas, *Phys. Chem. Phys*. **2006**, 8, 1645. (b) W. Koch, M. C. Holthausen, *A Chemist's Guide to Density Functional Theory*; 2nd ed.;

Wiley-VCH; Weinheim, Germany, 2001. (c) O. Gunnarsson, B. I., B. I. Lundqvist, *Phys. Rev. B*, **1976**, 13, 4274. (d) D. Dai, M. -H. Whangbo, *J. Chem. Phys*., **2003**, 118, 29.

13 (a) P. Chaudhuri, C. N. Verani, E. Bill, E. Bothe, T. Weyhermuller, K. Wieghardt, *J. Am. Chem. Soc.* 2001, **123**, 2213. (b) P. J. Chirik, K. Wieghardt, *Science*, 2010, **327**, 794. (c) V. K. K. Praneeth, M. R. Ringenberg, T. R. Ward, Angew. Chem. Int. Ed., 2012, **51**, 10228. (d) O. R. Luca, R. H. Crabtree, *Chem. Soc. Rev.*, 2013, **42**, 1440.

14 (a) Z. Sun, Q. Ye, C. Chi, J. Wu, Chem. Soc. Rev., 2012, **41**, 7857 (b) A. Mailman, J. W. L. Wong, S. M. Winter, R. C. M. Claridge, C. M. Robertson, A. Assoud, W. Yong, E. Steven, P. A. Dube, J. S. Tse, S. Desgreniers, R. A. Secco, R. T. Oakley, *J. Am. Chem. Soc*. 2017, **139**, 1625.

15 X. Ma, E. A. Suturina, M. Rouzieres, M. Platunov, F. Wilhelm, A. Rogalev, R. Clerac, P. Dechambenoit, *J. Am. Chem. Soc.*, 2019, DOI: 10.1021/jacs.9b03044.

16 K. T. Sylvester, P. J. Chirik, *J. Am. Chem. Soc*., 2009, **131**, 8772.

17 Z. Li, Y. Liu, X. Kang, Y. Cui, *Inorg. Chem.*, 2018, **57**, 9786.

18 J. L. Brusso, O. P. Clements, R. C. Haddon, M. E. Itkis, A. A. Leitch, R. T. Oakley, R. W. Reed, J. F. Richardson, *J. Am. Chem. Soc.*, 2004, **126**, 8256.

19 S. Kundu, S. Sinhababu, V. Chandrasekhar, H. W. Roesky, *Chem. Sci*., 2019, DOI: 10.1039/C9SC01351B.

20 (a) S. Demir, I-R. Jeon, J. R. Long, T. D. Harris, *Coord. Chem. Rev.* 2015, **289**, 149. (b) C. Benelli, D. Gatteschi, *Chem. Rev*. 2002, **102**, 2369. (c) K. E. Preuss, *Coord. Chem. Rev*. 2015, **289**, 49.

21 (a) G. A. Abakumov, V. K. Cherkasov, V. I. Nevodchikov, V. A. Kuropatov, G. T. Yee, C. G. Pierpont, *Inorg. Chem*. 2001, **40**, 2434. (b) D. J. Sullivan, R. Clerac, M. Jennings, A. J. Lough, K. E. Preuss. *Chem. Commun*, 2012, **48**, 10963. (c) T. J. Woods, M. F. Ballesteros-Rivas, S. M. Ostrovsky, A. V. Palii, O. S. Reu, S. I. Klokishner, K. R. Dunbar, *Chem. Eur. J*. 2015, **21**, 10302. (d) M. A. Lemes, H. N. Stein, B. Gabidulin, K. Robeyns, R. Clerac, M. Murugesu, *Chem. Eur. J*. 2018, **24**, 4259. (e) C. Das, A. Upadhyay, M. Shanmugam, *Inorg.*

Chem. 2018, **57**, 9002. (f) I. S. Morgan, A. Mansikkamaki, G. A. Zissimou, P. A. Koutentis, M. Rouzieres, R. Clerac, H. M. Tuononen. *Chem. Eur. J*. 2015, 21, 15843. (g) S. Demir, M. I. Gonzalez, L. E. Darago, W. J. Evans, J. R. Long, *Nature Commun*. 2017, **8**, 2144. (h) E. M. Fatila, M. Rouzières, M. C. Jennings, A. J. Lough, R. Clérac, K. E. Preuss, *J. Am. Chem. Soc*. 2013, **135**, 9596.

22 (a) L. Norel, F. Pointillart, C. Train, L-M. Chamoreau, K. Boubekeur, Y. Journaux, A. Brieger, D. J. R. Brook, *Inorg. Chem.* 2008, **47**, 2396. (b) I-R. J. G. Park, D. J. Xiao, T. D. Harris, *J. Am. Chem. Soc.*, 2013, **135**, 16845.

23 I. A. Gass, S. Tewary, A. Nafady, N. F. Chilton, C. J. Gartshore, M. Asadi, D. W. Lupton, B. Moubaraki, A. M. Bond, J. F. Boas, S-X. Guo, G. Rajaraman, K. S. Murray, *Inorg. Chem.* 2013, **52**, 7557.

24 (a) T. M. Barclay, R. G. Hicks, M. T. Lemaire, L. K. Thompson, *Chem. Commun*, 2000, **0**, 2141. (b) J. A. DeGayner, l-R. Jeon, T. D. Harris, *Chem. Sci.*, 2015, **6**, 6639.

25 (a) J. D. Rinehart, M. Fang, W. J. Evans, J. R. Long, *J. Am. Chem. Soc.* 2011, **133**, 14243. (b) K. R. Meihaus, J. F. Corbey, M. Fang, J. W. Ziller, J. R. Long, W. J. Evans, *Inorg. Chem*., 2014, **53**, 3099. (c) S. Demir, J. M. Zadrozny, M. Nippe, J. R. Long, *J. Am. Chem. Soc.* 2012, **134**, 18546.

26 W. Kaim, *Coord. Chem. Rev*., 2002, **230**, 127.

27 (a) W. Kaim, J. Z. Fees, *Naturforsch.* ***B*** **50b**, 1995, 123. (b) M. D. Coburn, G. A. Buntain, B. W. Harris, M. A. Hiskey, K. –Y. Lee, D. G. Ott, *J. Heterocyclic Chem*. 1991, **28**, 2049.

28 M. Schawach, H-D. Hausen, W. Kaim, *Inorg. Chem*. 1999, **38**, 2242.

29 S. K. Tripathy, M. va der Meer, A. Sahoo, P. Laha, N. Dehury, S. Plebst, B. Sarkar, K. Samanta, S. Patra, *Dalton Trans*., 2016, **45**, 12532.

30 (a) X-H. Bu, H. Liu, M. Du, L. Zhang, Y-M. Guo, *Inorg. Chem*., 2002, **41**, 1855. (b) S. Maiji, B. Sarkar, S. Patra, J. Fiedler, S. M. Mobin, V. G. Puranik, W. kaim, G. K. Lahiri. (c) M. A. Lemes, A. Pialat, S. N. Steinmann, I. Korobkov, C. Michel, M. Murugesu, 2015, **108**, 163. (d) M. A. Lemes, H. N. Stein, B. Gabidullin, S. N. Steinmann, M. Murugesu, *ACS Omega*, 2018, **3**, 10273.

31 (a) H. T. Chifotides, I. D. Giles, K. R. Dunbar, *J. Am. Chem. Soc*., 2013, **135**, 3039 (b) B. L. Schottel, H. T. Chifotides, K. R. Dunbar, *Chem. Soc. Rev*., **2008**, 37, 68. (c) B. S. Dolinar, S. G.-Coca, D. I. Alexandropoulos, K. R. Dunbar, *Chem. Commun*., 2017, **53**, 2283. (d) B. S. Dolinar, D. I. Alexandropoulos, K. R. Vignesh, T. James, K. R. Dunbar, *J. Am. Chem. Soc.* 2018, **140**, 908.

Chapter 2

Strong ferromagnetic exchange coupling in a $\{Ni^{II}_4\}$ cluster mediated through an air-stable tetrazine-based radical anion

2.1. Abstract

A planar tetradentate 3,6-bis(2-pyrimidyl)-1,2,4,5-tetrazine (bpymtz) templating chelate affords the formation of an unprecedented bpymtz$^{\bullet-}$ radical anion bridged $\{Ni^{II}_4\}$ complex. Detailed magnetic measurements performed on the isolated air stable $[Ni^{II}_4(bpymtz^{\bullet-})Cl_6(DMF)_8]Cl{\cdot}0.5(H_2O)$ compound reveal strong ferromagnetic Ni^{II}-bpymtz$^{\bullet-}$ interactions with a coupling constant of $J = 98.84$ cm^{-1}. The results of this studies have been published in: Lemes, M. A.; Brunet, G.; Pialat A.; Ungur, L.; Korobkov, I.; Murugesu, M. *Chem. Commun*. **2017**, 53, 8660 – 8663. Permission to include this paper in the thesis has been granted by Royal Society of Chemistry.

2.2. Introduction

Chelating ligands play a vital role in coordination chemistry; they provide ideal environments for metals to bind and form stable compounds. Since the development of coordination complexes, chemists have designed and synthesized chelates with various donor atoms in order to isolate discrete metal complexes. Through careful design strategies, it is possible to target and isolate mono-,[1] di-,[2] and trinuclear metal complexes.[3] However, discrete polymetallic complexes with one single templating ligand remain extremely rare. Chelates with multiple coordination pockets still require more than one ligand to isolate cluster aggregates.[4] This is mainly due to the difficulty in the synthesis and stabilization of the resulting metal complexes.

Polymetallic complexes are highly sought after owing to their catalytic,[5] bio-mimicking[6] and magnetic properties,[7] to name a few. In molecular magnetism, investigation of polymetallic transition metal complexes is an active area of research since the discovery of a $\{Mn_{12}\}$ complex that exhibits magnet-like behavior of slow relaxation of the magnetisation.[8] Such discrete molecules are termed Single-Molecule Magnets

(SMMs). Several thousand polymetallic complexes have been reported since then, in an attempt to obtain SMM behavior at high temperatures. The vast majority of these complexes are frequently synthesized *via* a directed, yet serendipitous approach.[9] One common goal in the isolation of these magnetic cluster aggregates is the promotion of ferromagnetic interactions, i.e. parallel alignment of the spins, to achieve high-spin molecules. Often, carefully selected ligands such as N_3^- led to the formation of self-assembled clusters with large spin ground states.[10] However, in these molecules, the magnetic exchange between the metal ions occurs *via* superexchange pathways. These interactions tend to be weak and difficult to control or predict. Thus, recent focus has shifted towards radical-bridged systems where strong exchange coupling can be expected. For instance, quinones and verdazyl radical bridging ligands can afford considerable coupling constants with magnitudes greater than 200 cm^{-1}, thanks to the presence of an unpaired electron on the bridging moiety.[3]

With these goals in mind, we have focused our attention on synthesizing a rigid ligand framework that offers a unique template in which coordination pockets are centered around a central tetrazine bridging motif (Figure 2.1). Tetrazines are strong π-acceptors due to the presence of a low-lying π* LUMO arising from the four nitrogen atoms in the cycle leading to the electrophilic nature. As a result of this unique characteristic, it can be easily reduced and act as an electron reservoir.[11] Interestingly, the bpymtz may be isolated in metal complexes as both neutral species and the radical anion. Such that, our recent work with Ag^+ ions and bpymtz yielded 1- and 2-dimensional anion templated networks while the bpymtz ligand remained a neutral.[12] Moreover, attempts to isolate paramagnetic species with Fe(III) centers led to the cleavage of the central tetrazine moiety.[13] Also notable is the work by Kaim, Dunbar and co-workers, who reported six examples of bpymtz-based complexes, however, none of these molecules exhibit full occupancy of bpymtz's coordination pockets.[14] Herein, we present the first example of a strategically designed tetrametallic Ni(II) complex templated around the bpymtz radical. Notable for being synthesized and isolated under aerobic conditions.

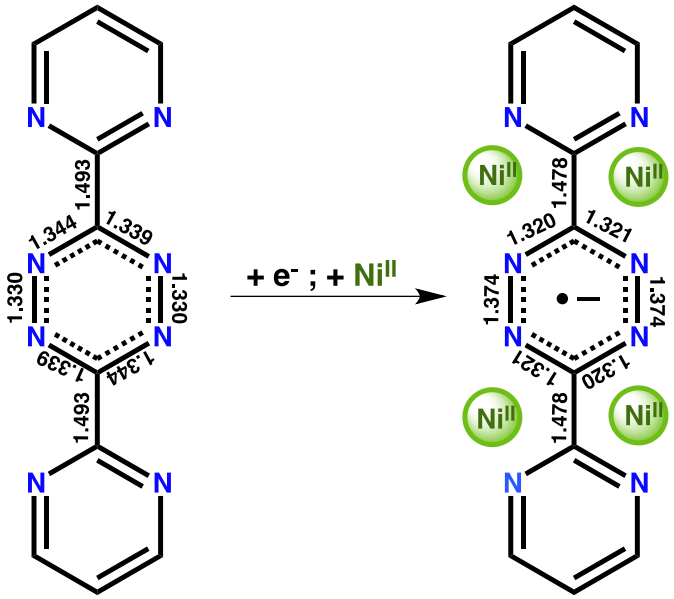

Figure 2.1. Selected bond distances (Å) for the neutral bpymtz (left) and the bpymtz$^{\bullet-}$ (right) highlighting structural changes of the ligand upon metal ions coordination.

2.3. Experimental

2.3.1. Materials

All manipulations were carried out under aerobic/ambient conditions. Chemicals were purchased from TCI, Alfa Aesar, and Stream Chemicals, and used without further purification.

2.3.2. Synthesis

3,6-bis(2-pyrimidyl)-1,2,4,5-tetrazine (bpymtz):

The ligand was prepared according to a modified procedure and exhibit spectral data identical to a previous report.[11]

To a dark yellow solution of 2-cyanopyrimidine (3 g, 28 mmol, 1 eq) and hydrochloric acid (4.5 mL, 55 mmol, 2 eq) in THF (40 mL) was added drop wise hydrazine hydrate (79%) (10.2 mL, 160 mmol, 6 eq). The resulting mixture was stirred under reflux over 4 h, then 40 mL of water was added to hydrolyze the reaction. THF was removed under reduced pressure and the product was extracted several times with CH_2Cl_2. The organic phase was combined, and the solvent was removed under reduced pressure to

afford H_2bpymtz as a bright orange solid. The compound was used in the next step without further purification. H_2bpymtz was dissolved in DMF and NO_2 gas was bubbled through the solution over 30 min. The gas was generated by the reaction of concentrated HNO_3 with copper turnings. Upon bubbling, a bright purple precipitated was formed and the solid was filtrated off and washed with cold water to afford 4.5 g of bpymtz in 68 % yield. ^{1}H NMR (400 MHz; $CDCl_3$) δ 9.18 (d, J = 4.9 Hz, 4H), 7.63 (t, J = 4.9 Hz, 2H).

$[Ni^{II}_4$(bpymtz)$(Cl)_6(DMF)_8]Cl_2$ (1):

To a purple solution of bpymtz ligand (59 mg, 0.25 mmol) in DMF (20 mL) was added $NiCl_2 \cdot 6H_2O$ (237.69 mg, 1 mmol). After being stirred for 1 min the solution turned dark green. The mixture was placed in a sealed vial. Orange rectangular crystals of **1** (yield = 30%) were collected by filtration after several days. Selected IR (cm^{-1}) 3233.69 (s), 1643.55 (s), 1590.16 (m), 1497.71 (m), 1436.65 (m), 1378.44 (s), 1251.30 (m), 1204.48 (m), 1108.05 (s), 1056.52 (m), 1030.94 (w), 760.98 (m), 682.95 (m), 661.21 (m). Elemental Analysis: Expected: C 31.06% H 4.83% N 17.04% Found: C 31.21% H 4.63% N 16.96%.

2.3.3. Physical measurements

X-ray crystallography

Suitable crystals were mounted on a glass fiber. A Bruker APEX-II CCD device was used to collect unit cell and intensity data using graphite Mo Kα radiation (λ = 0.71073). The data reduction included a correction for Lorentz and polarization effects, with an applied multiscan absorption correction (SADABS). The crystal structure was solved and refined using the SHELXTL program suite.[15] Direct methods yielded all non-hydrogen atoms, which were refined with anisotropic thermal parameters. All hydrogen atom positions were calculated geometrically and were riding on their respective atoms.

FTIR spectroscopy

Solid-state infrared spectra were obtained on a Varian 640 FT-IR spectrometer in the 400-4000 cm^{-1} range.

Magnetic measurements

Variable temperature magnetic susceptibility and magnetization measurements were performed on a crushed polycrystalline sample of **1** using a Quantum Design MPMS-XL7 SQUID magnetometer equipped with a 7 T dc magnet, in the temperature range 1.8 - 300 K for dc applied fields up to 7 T. An *M vs*. *H* measurement was performed at 100 K to confirm the absence of ferromagnetic impurities. Diamagnetic corrections were applied to the sample holder and to the observed paramagnetic susceptibility of **1** using Pascal constants.

2.4. Results and Discussion

The reaction of $NiCl_2{\cdot}6H_2O$ (4 equiv.) with bpymtz (1 equiv.) in N,N-dimethylformamide (DMF) gave a dark green solution. After several days, pale orange rectangular block-shaped crystals of $[Ni^{II}_4(bpymtz^{\bullet-})Cl_6(DMF)_8]Cl{\cdot}0.5(H_2O)$ (**1**) were isolated in 30% yield. Complex **1** crystallizes in the monoclinic space group C2/c (Figure 2.2). Crystallographic data and selected bond lengths and angles are summarized in Tables 2.1–2.3. The structure of the centrosymmetric complex **1** consists of a central $bpymtz^{\bullet-}$ radical acting as a template for four Ni(II) ions to bind to all four bpym-like coordination pockets (bpym = 2,2'-bipyrimidine). Two Cl atoms (Cl1, Cl1') act as bridges between Ni1 and Ni2, as well as their symmetrically equivalents Ni1' and Ni2' atoms. Two axially coordinating DMF molecules fill the remainder of the octahedral coordination sites for each Ni(II) ion. The side view of the molecular unit shown in Figure 2.2b and Figure 2.3 highlights that all four Ni(II) ions lie perfectly in the plane formed by the $bpymtz^{\bullet-}$ radical. The overall charge of the complex is balanced by one Cl^- anion located in the crystal lattice. Close inspection of the packing arrangement reveals that the closest Ni---Ni separation occurs at a distance of 7.28 Å, which likely precludes any significant intermolecular magnetic interactions (*vide infra* Figure 2.4). Although initially predicted by Kaim and co-workers,[11] this is the first time four metal ions occupancy is reported on the $bpymtz^{\bullet-}$ radical.

Table 2.1. Crystallography data of the complex **1**

Empirical formula	$C_{34}H_{63}Cl_7N_{16}Ni_4O_{8.5}$
Formula weight	1314.91
Crystal system	Monoclinic
Space group	C2/c
a/Å	11.7191(4)
b/Å	23.4564(7)
c/Å	21.6135(7)
α/ °	90
β/ °	91.4944(14)
γ/ °	90
V/ Å^3	5939.27
Z	4
T/K	200(2)
Radiation	Mo-K_α
Wavelength	0.71073
D_C/mg m^{-3}	1.470
μ/mm^{-1}	1.619
Reflections collected	7335
Goodness-of-fit on F^2	1.021
R1,wR2 (>2σ(I))[a]	0.0406, 0.1266

Table 2.2. Selected bond lengths (Å) for **1**.

Ni(1)-N(1)	2.0530(17)
Ni(1)-O(1)	2.0602(16)
Ni(1)-O(2)	2.0740(16)
Ni(1)-N(4)#1	2.1667(19)
Ni(1)-Cl(2)	2.3352(6)
Ni(1)-Cl(1)	2.4044(6)
Ni(2)-N(2)	2.0481(17)
Ni(2)-O(3)	2.0695(16)
Ni(2)-O(4)	2.0731(16)
Ni(2)-N(3)	2.1635(19)
Ni(2)-Cl(3)	2.3179(6)
Ni(2)-Cl(1)	2.4115(6)

Table 2.3. Selected angles (°) for **1**.

N(1)-Ni(1)-O(1)	86.59(7)	C(15)-O(4)-Ni(2)	126.97(16)
N(1)-Ni(1)-O(2)	85.25(7)	C(1)#1-N(1)-Ni(1)	117.47(14)
O(1)-Ni(1)-O(2)	168.85(7)	N(2)-N(1)-Ni(1)	126.75(12)
N(1)-Ni(1)-N(4)#1	77.52(7)	C(1)-N(2)-Ni(2)	117.43(14)
O(1)-Ni(1)-N(4)#1	84.78(7)	N(1)-N(2)-Ni(2)	127.00(12)
O(2)-Ni(1)-N(4)#1	86.05(7)	C(2)-N(3)-Ni(2)	112.60(14)
N(1)-Ni(1)-Cl(2)	170.93(5)	C(3)-N(3)-Ni(2)	131.09(16)
O(1)-Ni(1)-Cl(2)	93.62(5)	C(2)-N(4)-Ni(1)#1	112.79(14)
O(2)-Ni(1)-Cl(2)	93.25(5)	C(5)-N(4)-Ni(1)#1	130.65(16)
N(4)#1-Ni(1)-Cl(2)	93.46(5)	O(3)-Ni(2)-Cl(3)	95.02(5)
N(1)-Ni(1)-Cl(1)	90.39(5)	O(4)-Ni(2)-Cl(3)	93.73(5)
O(1)-Ni(1)-Cl(1)	94.83(5)	N(3)-Ni(2)-Cl(3)	94.08(5)
O(2)-Ni(1)-Cl(1)	92.80(5)	N(2)-Ni(2)-Cl(1)	90.28(5)
N(4)#1-Ni(1)-Cl(1)	167.91(5)	O(3)-Ni(2)-Cl(1)	93.23(5)
Cl(2)-Ni(1)-Cl(1)	98.62(2)	O(4)-Ni(2)-Cl(1)	95.35(5)
N(2)-Ni(2)-O(3)	84.72(7)	N(3)-Ni(2)-Cl(1)	168.01(5)
N(2)-Ni(2)-O(4)	85.21(7)	Cl(3)-Ni(2)-Cl(1)	97.86(2)
O(3)-Ni(2)-O(4)	166.79(7)	Ni(1)-Cl(1)-Ni(2)	105.56(2)
N(2)-Ni(2)-N(3)	77.77(7)	C(6)-O(1)-Ni(1)	125.78(15)
O(3)-Ni(2)-N(3)	84.69(7)	C(9)-O(2)-Ni(1)	122.59(18)
O(4)-Ni(2)-N(3)	84.83(7)	C(12)-O(3)-Ni(2)	125.50(17)
N(2)-Ni(2)-Cl(3)	171.85(5)		

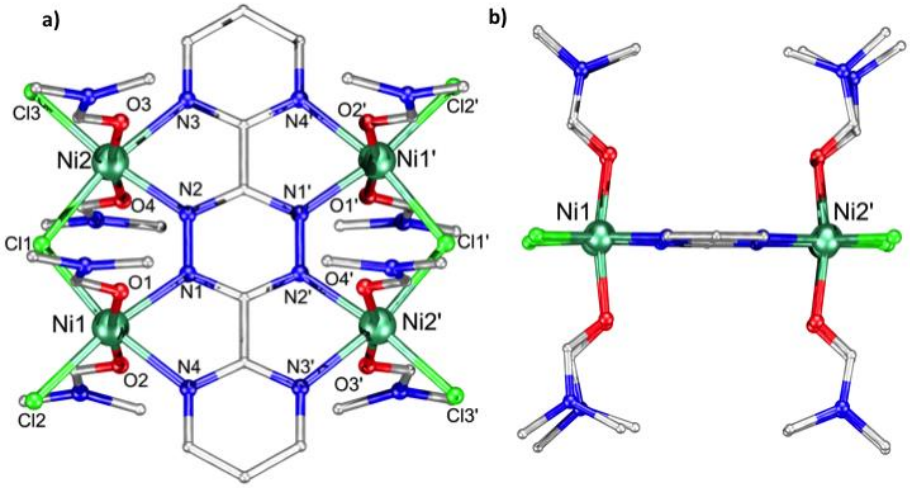

Figure 2.2. a) Ball–and–stick representation of the molecular structure of **1** with (b) side view of the molecule. Colour code: Ni (green), N (blue), O (red), Cl (light green) and C (grey). Hydrogen atoms, counter anions and lattice water molecules are omitted for clarity.

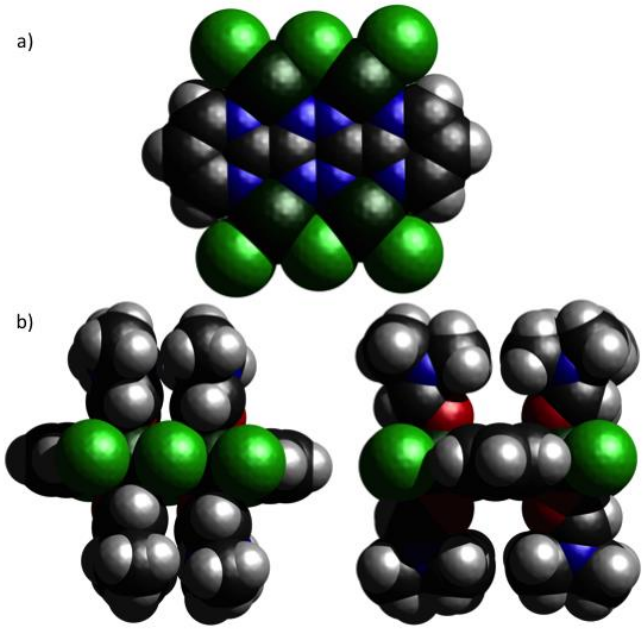

Figure 2.3. Space-filling model of the molecular structure of **1** highlights the featuring of the metal ions, chlorine atoms in the equatorial and DMF solvent molecule in the axial position of the coordination environment. a) Top view of the structure. In the center of the picture is placed the ligand bpymtz. The DMF solvent molecules were omitted to emphasize the metal accommodation in the ligand pocket. b) Side (right) and front (left)

views of the complex. Atom colors: Ni (dark green), H (light grey), C (dark grey), N (blue), O (red) and Cl (light green).

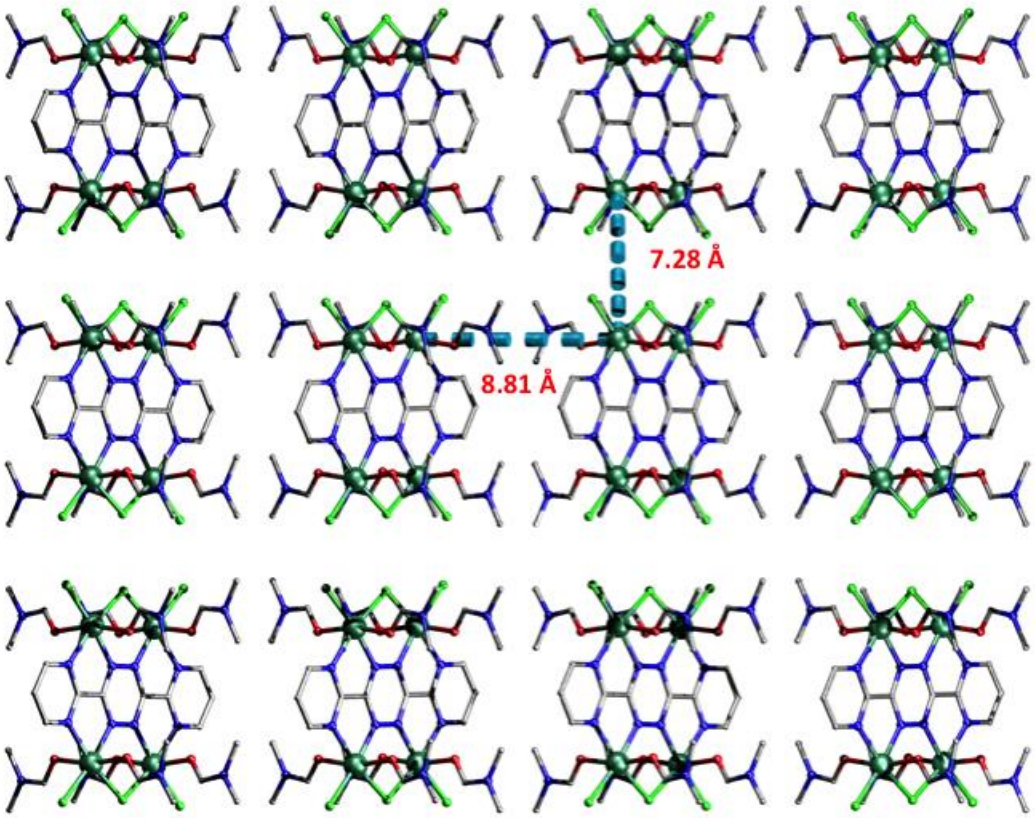

Figure 2.4. Crystal packing diagram of **1** along the *a* axis of the unit cell showing the metal-metal distance along the *b* and *c* axis.

FT-IR spectroscopy studies (Figure 2.5) reveal an asymmetric doublet that are at 1590 and 1567 cm^{-1} almost suppressed by the strong absorption peak at 1643 cm^{-1}, assigned to coordinated DMF molecules. These quasi-symmetrical peaks are assigned to the ring-stretching of the bpym-type coordination mode. For non-coordinated bpymtz, bpym ring-stretching is observed at lower wavenumbers of 1566 and 1557 cm^{-1}. Nevertheless, the doublet observed at relatively higher wavenumbers in the spectra of **1** is indicative of chelating bpym ligand.[16] A strong absorption band centered at 3400 cm^{-1} can also be observed due to the presence of lattice water molecules.

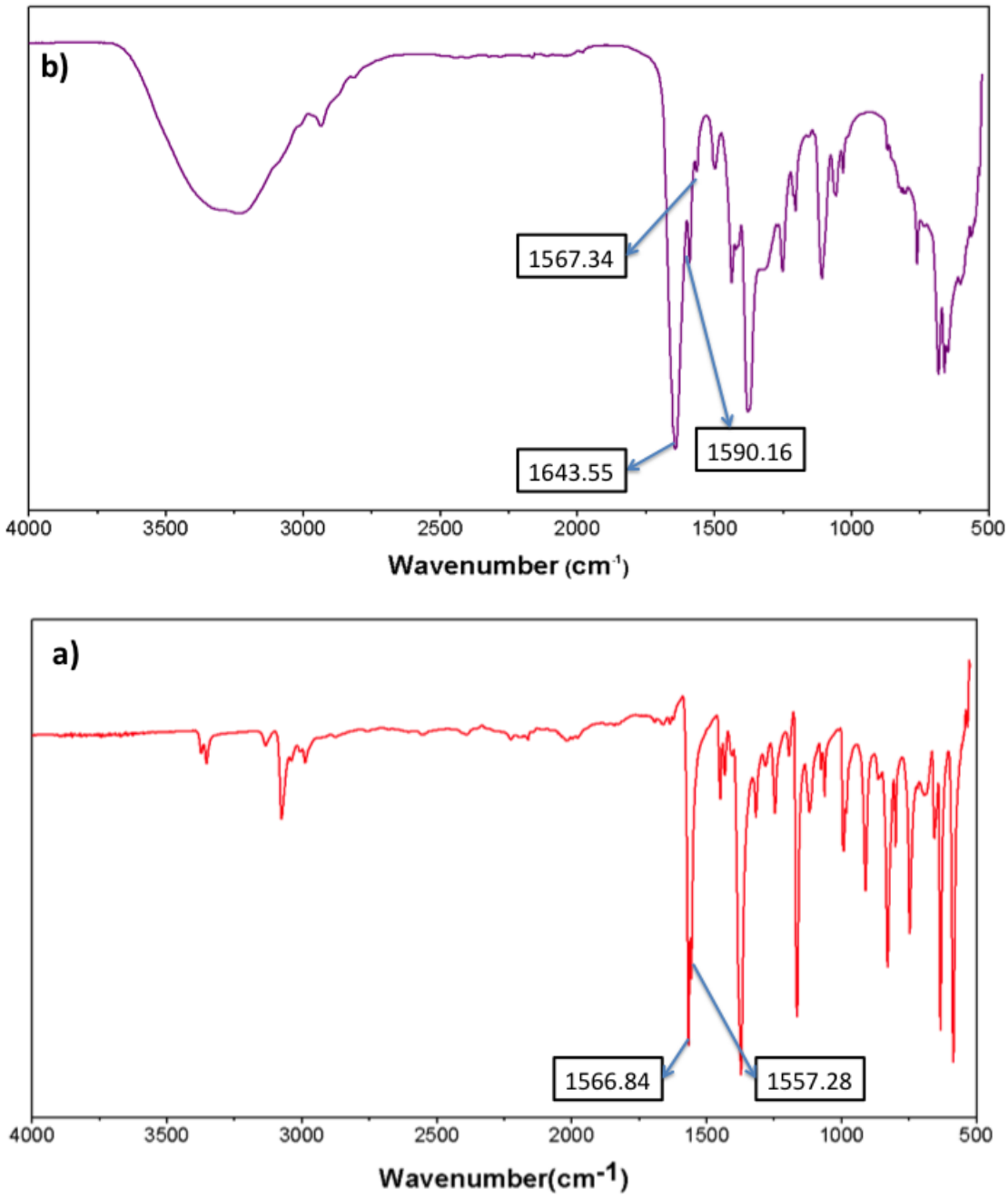

Figure 2.5. FT-IR spectra of ligand a) and complex b) at room temperature. The doublet at 1566.84 and 1557.28 cm^{-1} in a) indicates bpym ring-stretching while in b) the doublet at 1590.16 and 1567.34 cm^{-1} indicates bpym-bridged ligand. In the plot b) DMF absorption peak is characterized by the strong intensity at 1643.55 cm^{-1}.

Close inspection of the tetrazine motif indicates the reduction of tetrazine upon chelation. Elongation between the azo N=N bond length by 0.04 Å (*vide supra* Figure 2.1) suggest reduction. This type of elongation is commonly observed in several tetrazine-based ligand radical anions.[14b,14e,17] In addition, Bond Valence Sum (BVS) calculations on nickel ions (Ni1/Ni1' = 2.06; Ni2/N2' = 2.04) along with charge balance consideration corroborates well with the presence of central radical anion. DFT calculations confirm the reduced nature of the bpymtz in **1** (*vide infra*). Such presence of bridging radical unit in molecular frameworks is anticipated to lead to strong magnetic exchange.[18]

Therefore, to probe the magnetic interactions between the various spin carrying units, we have measured the direct current (dc) magnetic susceptibility of **1** over the temperature range of 1.8–300 K and under an applied field of 1000 Oe. The corresponding χT *vs.* T curve is presented in Figure 1.6. The room temperature χT value of 6.98 cm^3 K mol^{-1} is significantly higher than the expected value of 4.94 cm^3 K mol^{-1} for four $S = 1$ and one $S = ½$ independent spins, corresponding to four Ni(II) ions with $g = 2.14$ and the central tetrazine-based radical, respectively. Such behavior is consistent with nickel complexes magnetically coupled to radical ligands even at room temperature suggesting strong interaction.[19,3d] Upon decreasing temperature, the χT product increases monotonically up to a maximum value of 13.80 cm^3 K mol^{-1} at 9.0 K, where further cooling results in a drop to 12.20 cm^3 K mol^{-1} at 1.8 K. The drastic increase of the χT product with decreasing temperature is indicative of strong ferromagnetic coupling between the spin carriers.[20] Indeed, the strength of the ferromagnetic interactions is clearly evident even at room temperature, where the χT product is appreciably higher than the aforementioned theoretical value. In addition to the structural parameters that suggest that the tetrazine ring in bpymtz is in fact a radical anion (*vide infra*), another viable method to confirm the presence of an additional spin carrier consists of evaluating the χT value at key points of interest. The maximum value of χT (13.80 cm^3 K mol^{-1}) is in strong agreement with a large spin ground state of $S = 9/2$, where the expected χT value is 14.17 K cm^3 mol^{-1} with $g = 2.14$. A scenario involving the absence of a radical species ($S = 4$), would yield an approximate χT value of 11.39 K cm^3 mol^{-1}, which has been observed in a number of previously described ferromagnetic tetranuclear Ni(II) complexes.[21] The final decrease of

the χT curve below 9 K can be explained by zero-field splitting effects since intermolecular antiferromagnetic interactions can be precluded due to the large Ni-Ni separations (> 7.28 Å). Alternating current (ac) measurements were also performed, however no out-of-phase (χ'') signal was observed at zero or 1000 Oe applied static field.

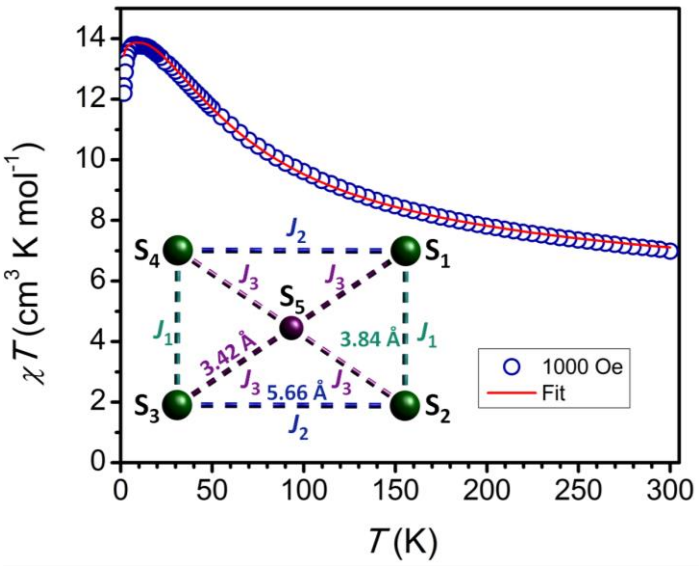

Figure 2.6. Temperature dependence of the χT product at 1000 Oe for **1**. The solid red line corresponds to the best fit using the magnetic model described in the text. Inset: schematic representation of the exchange coupling in the Ni_4 core of **1** with principal exchange pathways J_1, J_2 and J_3.

Initial attempts to fit the magnetic susceptibility data was carried out assuming an equivalent exchange interaction between all four Ni^{II} ions, however no appropriate fit could be obtained. Thus, to more accurately quantify the intramolecular magnetic exchange interactions, the magnetic data (susceptibility and magnetization) were fit using the *PHI* program,[22] according to the Hamiltonian: $H = -2J_1(S_1 \cdot S_2 + S_3 \cdot S_4) - 2J_2(S_1 \cdot S_4 + S_3 \cdot S_4) - 2J_3(S_1 \cdot S_5 + S_2 \cdot S_5 + S_3 \cdot S_5 + S_4 \cdot S_5)$ as shown in the inset of Figure 3. It is important to note that the isotropic *g*-factors were allowed to vary, while single ion anisotropy due to the ligand field was also taken into account. The best fit obtained led to the following parameters: $J_1 = -13.28$ cm^{-1}, $J_2 = -0.55$ cm^{-1}, $J_3 = 98.84$ cm^{-1}, $g = 2.14$, and $D = 2.81$ cm^{-1}. From these values, we can conclude that the interaction between the Ni(II) ions and

radical ligand spins is ferromagnetic (J_3), corroborating the S = 9/2 spin ground state. Field-dependent magnetic properties were also investigated between 1.9 and 7 K, and up to fields of 7 T (Figure 2.7). The magnetization (M) *vs.* field (H) data could be fit simultaneously with the magnetic susceptibility and supports the aforementioned parameters. The value of M at 1.9 K and 7 T of 9.44 μ_B is in strong agreement with the expected value of 9.63 μ_B using $g = 2.14$ and $S_T = 9/2$. The M *vs.* H/T plot shows non-saturation and non-superposition of the magnetization curves indicating the presence of low-lying excited states even at the low temperature region (Figure 2.7).

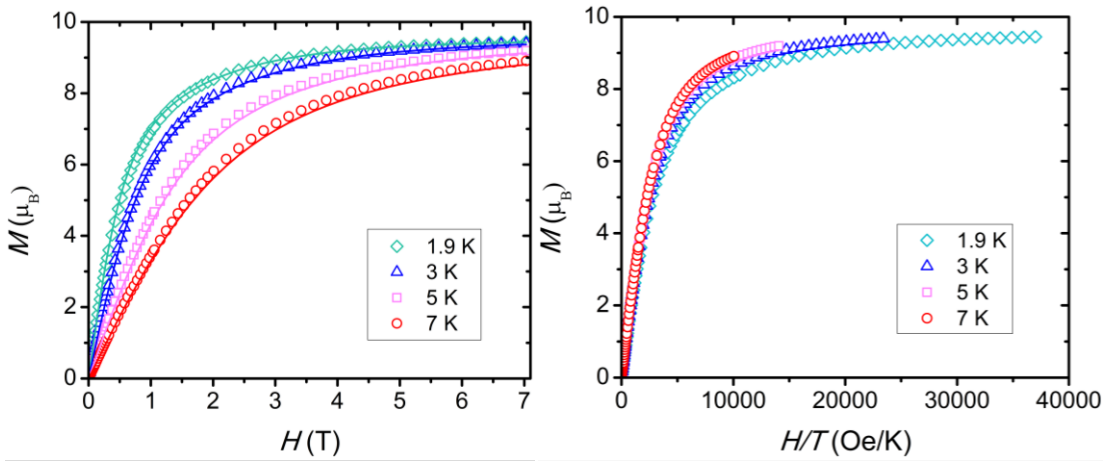

Figure 2.7. M *vs.* H (left) and M *vs.* H/T (right) plots for **1** between 1.9 and 7 K. Solid lines in the M *vs.* H plot correspond to the best fit obtained using the model described in the text.

To corroborate the experimental magnetic behavior of **1**, we have performed Broken-Symmetry DFT calculations, which confirm the strong ferromagnetic interaction between all Ni(II) sites and the bpymtz$^{\bullet-}$ radical anion (>200 cm^{-1}, for BP and B3LYP functionals). The large calculated coupling constant is not surprising give the significant amount of the equally distributed spin density on the nitrogen atoms of the tetrazine core (Figure 2.8). For the sake of comparison, a TD-DFT calculations was also performed for the neutral and the anionic ligand. The results show the bpymtz$^{\bullet-}$ would promote a more effective exchange coupling within metal ions in virtue of the much lower excited states compared with its neutral version (bpymtz) (Table 2.4). The strong ferromagnetic exchange

between Ni(II) ions and the tetrazine radical is probably due to the orthogonality of the magnetic orbitals in the system, preventing antiferromagnetic exchange mechanisms from being operational in this system. Such remarkable observation of ferromagnetic interactions is exceptional and uncommon. To the best of our knowledge, this is the first example of a ferromagnetic interaction involving a tetrazine radical. The presence of radicals in molecular frameworks that have led to ferromagnetic exchange interactions have been previously observed in verdazyl-based complexes,[3c,d] however it is unprecedented in tetrazinyl-based systems. Future work will be devoted towards a deeper understanding of the origin and mechanism of the magnetic exchange in this compound.

Table 2.4. TD-DFT results for the energy states (cm^{-1}) in the neutral and reduced version of the ligand

	Neutral ligand		**Reduced ligand**
1	11227.6	1	1981.1
2	17152.3	2	7332.3
3	21384.0	3	9017.3
4	23404.2	4	10290.0
5	23988.9	5	14123.9
6	24756.0	6	15788.3
7	26044.7	7	16416.5
8	26293.7	8	18680.6

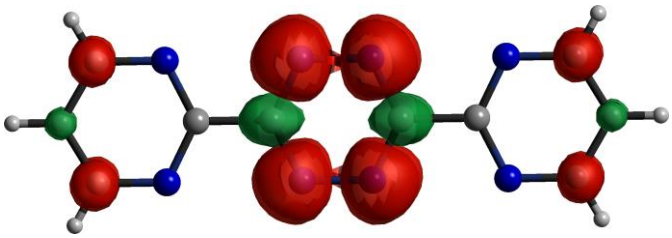

Figure 2.8. Distribution of the spin density of the bpymtz$^{\bullet-}$ radical anion in **1**. Colour code: N (blue), C (grey). Note the antiferromagnetic coupling of the spin densities on N and C of the central C_2N_4 unit of the tetrazine. The red and green colors indicate the sign of the spin density.

2.5. Conclusion

The use of bpymtz as a template for four Ni(II) metal ions has yielded the first example of a fully coordinated tetrazine-based ligand. The crystallographic and the magnetic investigations reveal evident ligand reduction upon coordination. Moreover, the magnetic properties unequivocally demonstrate strong intramolecular ferromagnetic interactions between the Ni(II) ions and the tetrazine radical anion, with a large coupling constant of $J = 98.84\ cm^{-1}$. DFT calculations confirm the dc measurements and the strength of the Ni(II)-bpymtz$^{\bullet-}$ interactions in the system through which multinuclear metal complexes can be obtained with strong ferromagnetic interactions. Overall, this work demonstrates the spontaneous reduction of a tetrazine-based ligand in the presence of metal ions, leading to an air-stable tetrametallic complex, which eliminates the need for exhaustive air-free conditions or reducing agents. Such unexpected ligand reduction of tetrazine-based ligands has been previously observed and are closely associated with the reaction conditions, where even diamagnetic starting metal salts were seen to be oxidized.[14c,e,16b] Thus, the results reported herein open a new avenue for designing and synthesizing air-stable radical-based complexes in the field of molecular magnetism .

2.6. References

1 C. R. Benson, A. K. Hui, K. Parimal, B. J. Cook, C-H. Chen, R. L. Lord, A. H. Flood and K. G. Caulton, *Dalton Trans*., 2014, **43**, 6513.

2 C. S. Araújo, M. G. B. Drew, V. Félix, L. Jack, J. Madureira, M. Newell, S. Roche, T. M. Santos, J. A. Thomas and L. Yellowlees, *Inorg. Chem*., 2002, **41**, 2250.

3 (a) J. O. Moilanen, N. F. Chilton, B. M. Day, T. Pugh and R. A. Layfield, *Angew. Chem. Int. Ed.,* 2016, **55**, 5521. (b) A. A. Zolotukhin, M. P. Bubnov, A. S. Bogomyakov, N. A. Protasenko, G. K. Fukin, I. D. Grishin and V. K. Cherkasov, *Inorg. Chim. Acta*, 2016, **440**, 16. (c) R. G. Hicks, M. T. Lemaire, L. K. Thompson, and T. M. Barclay, *J. Am. Chem. Soc*., 2000, **122**, 2261. (d) D. J. R. Brook, C. J. Richardson, B. C. Haller, M. Hundley and G. T. Yee, *Chem. Commun*. 2010, **46**, 6590.

4 (a) K. Chainok, S. M. Neville, C. M. Forsyth, W. J. Gee, K. S. Murray and S. R. Batten, *CrystEngComm*, 2012, **14**, 3717. (b)L. Rosenberg, E. J. Gabe, F. L. Lee and L. K. Thompson, *J. Chem. Soc. Dalton Trans.,* 1986, **1**, 625.

5 J. A. Flores, N. Komine, K. Pal, B. Pinter, M. Pink, C-H. Chen, K. G. Caulton and D. J. Mindiola, *ACS Catal.* 2012, **2**, 2066.

6 F. J. Rizzuto, W-Y. Wu, T. K. Ronson and J. R. Nitschke, *Angew. Chem. Int. Ed.,* 2016, **55**, 7958.

7 (a) G. Brunet, F. Habib, C. Cook, T. Pathmalingam, F. Loiseau, I. Korobkov, T. J. Burchell, A. M. Beauchemin and M. Murugesu, *Chem. Commun.*, 2012, **48**, 1287. (b) P. S. Perlepe, L. Cunha-Silva, K. J. Gagnon, S. J. Teat ,C. Lampropoulos, A. Escuer, and T. C. Stamatatos, *Inorg. Chem*., 2016, **55**, 1270.

8 R. Sessoli, D. Gatteschi, A. Caneschi, and M. A. Novak, *Nature*, 1993, **365**, 141.

9 (a) R. E. P. Winpenny, *J. Chem. Soc., Dalton Trans.,* 2002, **1**, 1. (b)R. Shaw, I. S. Tidmarsh, R. H. Laye, B. Breeze, M. Helliwell, E. K. Brechin, S. L. Heath, M. Murrie, S. Ochsenbein, H-U Güdel and E. J. L. McInnes, *Chem. Commun*.,

2004, **12**, 1418. (c) M. Murrie, H. Stoeckli-Evans and H. U. Güdel, *Angew. Chem. Int. Ed*. 2001, **40**, 1057.

10 (a) M. Murugesu, M. Habrych, W. Wernsdorfer, K. A. Abboud, and G. Christou, *J. Am. Chem. Soc*., 2004, **126**, 4766. (b) A. M. Ako, I. J. Hewitt, V. Mereacre, R. Clérac, W. Wernsdorfer, C. E. Anson and A. Power, *Angew. Chem. Int. Ed*., 2006, **45**, 4926. (c) G. S. Papefstathiou, A. K. Boudalis, T. T. Stamatatos, C. J. Milios, C. G. Efthymiou, C. P. Raptopoulou, A. Terzis, V. Psycharis, Y. Sanakis, R. Vincente, A. Escuer, J.–P. Tuchagues, and S. P. Perlepes, *Polyhedron,2007,* **26**, 2089-2094

11 (a) W. Kaim and J. Fees, *Z. Naturforsch,* 1995, **50b**, 123. (b) W. Kaim, *Coord. Chem. Rev*., 2002, **230**, 127. D. A. Safin, A. Pialat, A. A. Leitch, N. A. Tumanov, I. Korobkov, Y. Filinchuk, J. Brusso and M. Murugesu, *Chem. Commun*., 2015, **51**, 9547.

12 M. A. Lemes, A. Pialat, S. N. Steinmann, I. Korobkov, C. Michel and M. Murugesu, *Polyhedron*, 2016, **108**, 163.

13 (a) I. D. Giles, H. T. Chifotides, M. Shatruck and K. R. Dunbar, *Chem. Commun.*, 2011, **47**, 12604. (b) T. J. Woods, M. F. Ballesteros-Rivas, S. M. Ostrovsky, A. V. Palii, O. S. Reu, S. I. Klokishiner and K. R. Dunbar, *Chem. Eur. J.,* 2015, **21**, 10302. (c) S. Frantz, W. Kaim, J. Fiedler, C. Duboc and *Inorg. Chim. Act*., 2004, **357**, 3657. (d) M. Ketterle, J. Fiedler and W. Kaim, *Chem. Commun*., 1998, **16**, 1701. (e) M. Glöckle, K. Hubler, H.-J. Kümmerer, G. Denninger and W. Kaim, *Inorg. Chem*., 2001, **40**, 2263. (f) M. Glöckle, J. Fiedle and W. Kaim, *Z. Anorg. Allg. Chem*., 2001, **627**, 1441.

14 Sheldrick, G. M. *Acta Crystallographica Section A*, **2008**, 64, 112-122.

15 I. Castro, M. Julve, G. De Munno, G. Bruno, J. A. Real, F. Lloret and J. Faus, *J. Chem. Soc. Dalton Trans*., 1992, **1**, 1739.

16 (a) M. Schwach, H-D. Hausen and W. Kaim, *Inorg. Chem.,* 1999, **38**, 2242. (b) S. M. Tripathy, M. van der Meer, A. Sahoo, P. Laha, N. Dehury, S. Plebst, B. Sarkar, K. Samanta and S. Patra. *Dalton Trans*., 2016, **45**, 12532. (c) K.

Parimal, S. Vyas, C-H. Chen, C. M. Hadad and A. H. Flood, *Inorg. Chim. Acta*, 2011, **374**, 620.

17 S. Demir, I-R. Jeon, J. R. Long, and T. D. Harris, *Coord. Chem. Rev.* 2015, **149**, 289.

18 (a) T. M. Barclay, R. G. Hicks, M. T. Lemaire and L. K. Thompson, *Chem. Commun.*, 2000, 2141. (b) K. Osanai, A. Okazawa, T. Nogami and T. Ishida, *J. Am. Chem. Soc.*, 2006, **128**, 14008. (c) F. M. Romero, D. Luneau and R. Ziessel, *Chem. Commun.*, 1998, **5**, 551.

19 (a) T. M. Barclay, R. G. Hicks, M. T. Lemaire and L. K. Thompson, *Inorg. Chem.*, 2001, **40**, 5581. (b) D. Luneau, F. M. Romero and R. Ziessel, *Inorg. Chem.*, 1998, **37**, 5078.

20 (a) T. K. Karmakar, S. K. Chandra, J. Ribas, G. Mostafa, T. H. Lu and B. K. Ghosh, *Chem. Commun.*, 2002, 2364. (b) R. W. Saalfrank, S. Trummer, U. Reimann, M. M. Chowdhry, F. Hampel and O. Waldmann, *Angew. Chem. Int. Ed.*, 2000, **39**, 3492. (c) B. Kersting, G. Steinfeld and D. Sibert, *Chem. Eur. J.*, 2001, **7**, 4253.

21 N. F. Chilton, R. P. Anderson, L. D. Turner, A. Soncini and K. S. Murray, *J. Comput. Chem.*, 2013, **34**, 1164.

Chapter 3

Probing magnetic exchange coupling in supramolecular squares based on a reducible tetrazine-derived ligand

3.1. Abstract

Reducible 3,6-bis(3,5-dimethyl-pyrazolyl)1,2,4,5-tetrazine was employed to isolate supramolecular [Co_4] and [Zn_4] squares, which were achieved via careful selection of counter ions rather than the use of reducing agents. Magnetic susceptibility studies reveal a strong radical-Co(II) exchange coupling ($J_{rad\text{-}Co}$/hc= -118 cm^{-1}, -2*J* formalism) with a spin ground state of S = 4, while the unreduced analogue reveals negligible coupling between the Co centers ($J_{Co\text{-}Co}$= -0.64 cm^{-1}). Radical-radical coupling was probed in the [Zn_4] congener, which led to $J_{rad\text{-}rad}$/hc = -15.9(5) cm^{-1}. These results highlight the versatile coordination chemistry of tetrazine and the importance of exploiting easily reducible delocalized radical to promote strong exchange coupling between spin carriers. Lemes, M. A.; Stein, H. N.; Gabidullin, B.; Robeyns, K.; Clérac, R.; Murugesu, M. *Chem. Eur. J.,* **2018**, 24, 4259-4263. Permission to include this paper in the thesis has been granted by John Wiley and Sons (License number: 4540220966549).

3.2. Introduction

The field of supramolecular chemistry continues to fascinate scientists due to the array of elegant and intricate structures with functionalities exhibiting sensing, optical, magnetic and catalytic properties, as well as the development of molecular machinery.[1] The power of such chemistry lies in the ability to tailor unique chemical and physical properties through weak supramolecular interactions.[2] For instance, in biology supramolecular interactions dominate the formation of macromolecules such as proteins, DNA and RNA due to the dynamic reversibility of non-covalent bonds.[3] The functionalities of such systems are largely determined by the manner in which weak interactions, such as

disulphide bridges, hydrogen bonding as well as van der Waals forces, dictate the structural arrangement.[3-5]

In molecular systems, these same short-contacts influence and drive the formation of specific supramolecular architectures based on interactions induced by the presence of solvent, counter ions and guest molecules.[6] Exploiting these interactions results in the facile and convergent synthesis of supramolecular polygons, chains, layers and 3 D networks, along with a multitude of other complex structures.[7] As structure directing agents, solvent can influence the crystal growth and morphology.[8] It has been reported in several cases that modifying the solvent system has resulted in drastic changes in topology; from octagonal to decagonal compounds,[7] square nets to honeycomb crystallization,[8] and even zigzag chains to helices.[9] Such transformations seem to be the result of changing the polarity and/or bulkiness of the solvent system. This has the capacity to alter the presence/absence of hydrogen bonds, anion-π interactions as well as the volume occupancy within the crystal structure.[8, 10, 11]

The ability to control molecular self-organization by manipulating non-covalent bonds and subsequently to fine-tune its properties is a key challenge in supramolecular chemistry. With this in mind, we have decided to implement the coordination chemistry of tetrazine-based ligands. These frameworks represent ideal candidates for supramolecular architectures, due to their easily reducible electrophilic tetrazine core (Tz), ability to bridge metal ions and also to induce weak anion-π interactions with guest molecules.[11] Furthermore, previous reports have demonstrated that tetrazine radical-metal direct exchange affords significant coupling constants.[12] Indeed, several studies have elegantly described the efficiency of metal-radical direct magnetic coupling over metal-metal superexchange pathways.[13]Thus employment of the highly delocalized 3,6-bis(3,5-dimethyl-pyrazolyl)1,2,4,5-tetrazinyl (bpytz$^{\bullet-}$; Scheme 3.1) radical anion can be ideal for the isolation of molecular complexes that act as one single entity with a large spin ground state. To that end, we herein report the development of novel molecular square architectures templated by a solvent molecule *via* supramolecular interactions.

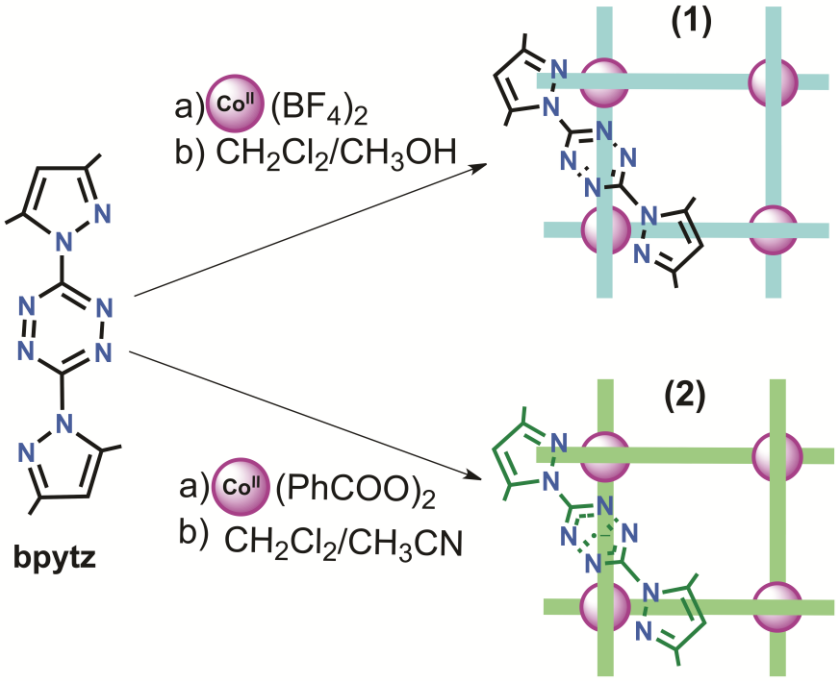

Scheme 3.1. Reaction conditions for the formation of the present molecular squares. The green ligand in **(2)** indicates the reduced form of bpytz.

3.3. Experimental Procedures

3.3.1. Materials

All manipulations were carried out under aerobic/ambient conditions. Chemicals were purchased from TCI, Alfa Aesar, and Stream Chemicals, and used without further purification.

3.3.2. Synthesis

3,6-bis(3,5-dimethyl-pyrazolyl)1,2,4,5-tetrazine (bpytz):

The ligand was prepared according to a previous report (For more information, please see Reference 27 in Chapter 1).

$[Co^{II}_4(bpytz)_4(CH_3CN)_6(H_2O)_2](BF_4)_8 \cdot (CH_3CN)$ (1):

The synthesis of (1) was carried out using $Co(BF_4)_2$ in CH_2Cl_2/CH_3CN 1:1 (20 mL) and then added to a coral solution of bpytz (0.125 mmol, 0.034 g). The mixture resulted in the formation of a dark brown solution. Diethyl ether diffusion produced brown needle crystals that were suitable for single-crystal X-ray crystallography. Yield = 50%. Selected IR (cm^{-1}): 1584.65 (s), 1497.12 (s), 1459.78 (m), 1442.21 (m), 1409.83 (m), 1375.10 (s), 1282.93 (s), 1095.83 (w), 1039.78 (b), 983.94 (m), 830.32 (m), 774.17 (m), 592.22 (w), 578.65 (m). Elemental Analysis: Calcd: C, 31.70%; H, 3.43%; N, 23.35%; Exp: C, 31.32%; H, 3.53% N, 22.94%;

$[Co^{II}_4(bpytz^{\bullet-})_4(PhCOO)_4] \cdot (C_2H_5)_2O \cdot CH_3OH \cdot 0.5H_2O$ (2):

A coral solution of bpytz (0.125 mmol, 0.034 g) in CH_2Cl_2 (10 mL) was added with stirring to a light pink solution of $Co(PhCOO)_2$ (0.125 mmol, 0.037 g) in CH_2Cl_2/CH_3OH 1:1 (10 mL) which immediately formed a dark brown mixture. After being stirred for 30 s, the solution was filtered under gravity and placed into a diethyl ether bath to promote crystallization. Block-shaped black crystals suitable for single-crystal X-ray crystallography were collected after 24 hours from a now dark purple solution. Yield = 30%. Selected IR (cm^{-1}): 1593(w), 1575(m), 1538(m), 1480(w), 1409(s), 1368(m), 1271(m), 1154(b), 1103(m), 1053(w), 1037(w), 982(m), 852(m), 809(w), 774(w), 723(s), 683(m), 659(w), 645(w), 612(m), 589(w). Elemental Analysis: Calcd: C, 61.80%; H, 5.70%; N, 5.34% Exp: C, 61.58%; H, 5.45%; N, 5.30%.

$[Zn^{II}_4(bpytz^{\bullet-})_4(CH_3COO)_4] \cdot (1.67(CH_6CH_4O) \cdot 3.83(PhCH_3)$ (3):

The synthesis of this compound was similarly performed as (1), however using toluene (20mL) and $Zn(CH_3COO)_2$ which resulted in the formation of a black solution. Within 24 hours, black block-shaped crystals were obtained by diethyl ether diffusion. Yield = 30%. Selected IR (cm^{-1}): 1709(w), 1571(s), 1480(w), 1403(s), 1371(w), 1284(m), 1222(w), 1117(s), 1056(m), 984(m), 933(w), 795(w), 777(w), 733(m), 696(w), 678(m), 653(w),

615(m), 593(w), 539(w), 530(w). Elemental Analysis: Calcd: C, 52.29%; H, 5.66%; N, 21.81%; Exp: C, 52.25%; H, 5.16%; N, 21.12%.

3.3.3. Physical measurements

X-ray crystallography

Suitable crystals were mounted on a glass fiber. A Bruker APEX-II CCD device was used to collect unit cell and intensity data using graphite Mo Kα radiation (λ = 0.71073 Å). The data reduction included a correction for Lorentz and polarization effects, with an applied multiscan absorption correction (SADABS). The crystal structure was solved and refined using the SHELXTL program suite. Direct methods yielded all non-hydrogen atoms, which were refined with anisotropic thermal parameters. All hydrogen atom positions were calculated geometrically and were riding on their respective atoms.

FTIR spectroscopy

Solid-state infrared spectra were obtained on a Varian 640 FT-IR spectrometer in the 400-4000 cm^{-1} range.

Magnetic measurements

Variable temperature magnetic susceptibility and magnetization measurements were performed on a crushed polycrystalline sample of 1, 2 and 3 using a Quantum Design MPMS-XL7 SQUID magnetometer in the temperature range 1.8 - 300 K for dc applied fields up to 7 T. An *M vs*. *H* measurement was performed at 100 K to confirm the absence of ferromagnetic impurities. Diamagnetic corrections were applied to the sample holder and to the observed paramagnetic susceptibility of 1, 2 and 3 using Pascal constants.

3.4. Results and discussion

The stoichiometric reaction of $Co(BF_4)_2{\cdot}2(H_2O)$ with bpytz in a mix of CH_2Cl_2/CH_3CN (1:1), followed by diffusion of diethyl ether resulted in the formation of brown needles of $[Co^{II}_4(bpytz)_4(CH_3CN)_6(H_2O)_2]{\cdot}8(BF_4){\cdot}CH_3CN$ **(1)** in 50% yield.

Similarly, the reaction of $Co(PhCOO)_2$ and bpytz in a mix of CH_2Cl_2/CH_3OH (3:1) produced brown plate-shaped crystals of $[Co^{II}_4(bpytz^{\bullet-})_4(PhCOO)_4]\cdot(C_2H_5)_2O\cdot(CH_3OH)\cdot0.5(H_2O)$ **(2)** in 30% yield after diffusion of diethyl ether. In both cases, a mixture of solvents was utilized in order to control the reaction solubility. Combining $Zn(CH_3COO)_2\cdot2(H_2O)$ and bpytz in toluene, and diffusing diethyl ether affords black block crystals of $[Zn^{II}_4(bpytz^{\bullet-})_4(CH_3COO)_4]\cdot1.67(CH_6CH_4O)\cdot3.83(PhCH_3)$ **(3)** in 30% yield.

Single-crystal X-ray studies reveal that **1** and **3** crystallize in the monoclinic *C2/c* space group, while **2** crystallizes in the chiral tetragonal *I4* space group (see Table 3.1 for parameters and Table 3.3 and 3.4 for selected bond lengths and angles). The asymmetric unit of **1** contains two symmetrically related Co(II) ions, two bpytz, two CH_3CN and one partially occupied H_2O with a disordered CH_3CN in the same position. Conversely, due to the four-fold symmetry, the asymmetric unit in **2** only contains one crystallographically independent Co(II) ion, one bpytz ligand and one $PhCOO^-$ ligand. Lastly, the asymmetric unit of **3** is composed of four independent Zn(II) ions. Despite the different symmetry, all three compounds form a molecular square where four metal ions reside at the vertex, which are linked via four tetrazine moieties, with terminal ligands (CH_3CN/H_2O for **1**; $PhCOO^-$ for **2**; CH_3COO^- for **3**) filling the coordination environment (Figure 3.1 and 3.2). Enclosed within the cage, compound **1** shows disordered $[BF_4]^-$ ions displaying anion-π interactions with the tetrazine ligands. On the other hand, compounds **2** and **3** contain disordered diethyl ether solvent molecules displaying non-covalent interactions with the bpytz ligands (Figure 3.4). These subtle interactions lead to a supramolecular templating effect in the cyclization and stabilization of a molecular square rather than affording polymeric structures. Reactions performed using different conditions (co-ligands, counter-ions, solvent, temperature) failed to yield molecular complexes.

Table 3.1. Crystallography data of complexes **1-3**

	1	**2**	**3**
Empirical formula	$C_{60.76}$ $H_{78.38}$ B_8 Co_4 F_{32} $N_{38.38}$ $O_{1.62}$	C_{81} H_{89} Co_4 N_{32} O_{12}	$C_{89.49}$ $H_{115.34}$ N_{32} $O_{9.67}$ Zn_4
Formula weight	2302.61	1938.56	2055.56
Crystal system	Monoclinic	Tetragonal	Monoclinic
Space group	*C* 2/*c*	*I*4	*C* 2/*c*
a/Å	22.716(3)	17.1494(14)	56.92(3)
b/Å	20.473(3)	17.1494(14)	22.526(9)
c/Å	23.565(3)	15.5811(15)	15.755(7)
α/ °	90	90	90
β/ °	90.232(2)	90	97.601(9)
γ/ °	90	90	90
V/ Å^3	10959(2)	4582.4(9)	20025(15)
Z	4	2	8
T/K	200(2)	200(2)	200(2)
Radiation	Mo-Kα	Mo-Kα	Mo-Kα
Wavelength	0.71073	0.71073	0.71073
D_C/mg m^{-3}	1.396	1.405	1.364
μ/mm^{-1}	0.704	0.788	1.018
Reflections collected	52808	8025	44882
Goodness-of-fit on F^2	1.076	1.096	1.099
R_1, wR_2 ($I>2\sigma(I)$)[a]	0.0773, 0.1976	0.0970, 0.1982	0.0700, 0.1795

[a] $R_1 = \Sigma||F_0| - |F_c||/\Sigma|F_0|$. $wR_2 = (\Sigma[w(F_0^2 - F_c^2)^2]/\Sigma[w(F_0^2)^2])^{1/2}$.

Based on charge balance considerations, interatomic distances (Table 2.3) and bond valence sum (BVS) calculations (Table 3.2), all Co(II) ions in **1** and **2** adopt a +2 oxidation state.[14] In these three complexes, the Co(II) and Zn(II) ions adopt distorted octahedral environments, with bpytz/bpytz$^{\bullet-}$ ligands coordinated in a *trans* anti-orientation fashion to minimize the steric related stress (Figure 2.1). This up-down-up-down pattern of the ligands is consistent across all three complexes and allows the metal pockets to line up in a square conformation. The Co···Co cross ligand distance in **1** is ~7.03 Å and the cross-cavity distance is ~9.84 Å (Figure 3.2). The Co···Co···Co vertex angle in the range of 88.70°– 91.26° suggests a near perfect square geometry. The packing arrangement demonstrates extensive anion-π interactions, which are dictated by the tetrafluoroborate anions. Such supramolecular interactions likely govern the arrangement of the molecular square throughout the unit cell, which leads to self-assembly of the square architecture.[6] In the case of **2**, the adjacent Co···Co distance is ~6.76 Å and the cross-cavity distance is

~9.57 Å (Figure 3.2). The Co···Tz···Co angle is 171.9° for all four sides of the molecular square by symmetry, demonstrating minor bending, potentially due to the considerable non-covalent interactions with the encapsulated solvent molecule. Notably, the Co···Co···Co vertex angles correspond to a perfect square (90°). The topology dimensions described for **2** demonstrate a structural assembly resulting in a perfect molecular square with point symmetry *C4*. The packing arrangement of **2** reveals extensive short contacts benzoate/pyrazolyl/tetrazinyl groups, resulting in a regular 3D packing network with identical compound orientation and chirality (Figure 3.3).[15] Mostly, these contacts are driven by non-covalent C-H···π interactions in a distance range of 2.67 – 3.36 Å.

Table 3.2. Bond-Valence Sum (BVS) calculations for **1**, **2** and **3**.

Metal	**1**	**2**	**3**
Co^{II}	2.07(5)	2.10(4)	-
Zn^{II}	-	-	2.01(3)

Table 3.3. Selected bond lengths (Å) for complexes **1** - **3**

1		**2**		**3**			
Co(1)-O(1)	2.019(8)	Co(1)-N(6)	2.023(9)	Zn(1)-O(2)	2.088(6)	Zn(3)-O(5)	2.072(6)
Co(1)-N(16)	2.096(4)	Co(1)-N(3)	2.036(9)	Zn(1)-N(29)	2.101(7)	Zn(3)-N(12)	2.095(7)
Co(1)-N(13)	2.172(4)	Co(1)-N(1)	2.07(2)	Zn(1)-N(6)	2.102(6)	Zn(3)-N(19)	2.110(5)
Co(1)-N(1)	2.114(4)	Co(1)-O(2)	2.244(9)	Zn(1)-N(1)	2.141(6)	Zn(3)-N(17)	2.120(7)
Co(1)-N(17)	2.070(5)	Co(1)-N(8)	2.14(2)	Zn(1)-N(32)	2.154(7)	Zn(3)-N(16)	2.134(7)
Co(1)-N(3)	2.191(4)	Co(1)-O(1)	2.121(9)	Zn(1)-O(1)	2.333(7)	Zn(3)-O(6)	2.398(7)
Co(2)-N(5)	2.169(4)			Zn(2)-O(3)	2.072(7)	Zn(4)-O(7)	2.063(6)
Co(2)-N(8)	2.093(6)			Zn(2)-N(4)	2.100(6)	Zn(4)-N(21)	2.091(5)
Co(2)-N(11)	2.210(4)			Zn(2)-N(14)	2.102(7)	Zn(4)-N(27)	2.104(7)
Co(2)-N(9)	2.096(4)			Zn(2)-N(8)	2.118(6)	Zn(4)-N(25)	2.132(7)
Co(2)-N(20)	2.092(5)			Zn(2)-N(9)	2.126(6)	Zn(4)-N(24)	2.148(7)
Co(2)-N(19)	2.11(1)			Zn(2)-O(4)	2.426(7)	Zn(4)-O(8)	2.423(7)

Table 3.4. Selected angles (°) for complexes **1** - **3**

1		**2**		**3**	
N(17)-Co(1)-O(1)	90.5(3)	N(1)-Co(1)-O(23)	92.8(6)	O(2)-Zn(1)-N(29)	104.8(2)
N(17)-Co(1)-N(1)	91.2(2)	N(1)-Co(1)-O(22)	100.3(6)	O(2)-Zn(1)-N(6)	151.9(2)
N(17)-Co(1)-N(3)	85.1(2)	N(1)-Co(1)-N(3)	76.1(6)	N(29)-Zn(1)-N(6)	102.4(2)
N(17)-Co(1)-N(13)	176.4(2)	N(3)-Co(1)-O(23)	102.9(6)	O(2)-Zn(1)-N(1)	96.1(2)
N(17)-Co(1)-N(16)	102.1(2)	O(23)-Co(1)-O(22)	59.7(5)	N(29)-Zn(1)-N(1)	94.5(2)
O(1)-Co(1)-N(16)	96.6(3)	N(3)-Co(1)-O(22)	162.3(6)	N(6)-Zn(1)-N(1)	74.5(2)
O(1)-Co(1)-N(1)	99.0(3)	O(22)-Co(1)-N(6)	94.6(5)	O(2)-Zn(1)-N(32)	96.5(2)
O(1)-Co(1)-N(3)	171.6(3)	N(6)-Co(1)-N(3)	103.0(6)	N(29)-Zn(1)-N(32)	74.5(2)
O(1)-Co(1)-N(13)	91.4(3)	N(6)-Co(1)-O(23)	153.8(6)	N(6)-Zn(1)-N(32)	97.5(2)
N(1)-Co(1)-N(3)	74.0(2)	N(3)-Co(1)-N(8)	94.7(6)	N(1)-Zn(1)-N(32)	165.0(2)
N(1)-Co(1)-N(13)	91.5(2)	N(6)-Co(1)-N(8)	77.3(6)	O(2)-Zn(1)-O(1)	58.4(2)
N(1)-Co(1)-N(16)	159.3(2)	N(8)-Co(1)-O(22)	90.6(6)	N(29)-Zn(1)-O(1)	161.1(2)
N(3)-Co(1)-N(13)	93.4(1)	N(8)-Co(1)-O(23)	96.3(6)	N(6)-Zn(1)-O(1)	95.6(2)
N(3)-Co(1)-N(16)	91.3(2)	N(8)-Co(1)-N(1)	168.3(7)	N(1)-Zn(1)-O(1)	95.8(2)
N(13)-Co(1)-N(16)	74.6(2)	Co(1)-Co(1)-Co(1)	90.0(0)	N(32)-Zn(1)-O(1)	97.6(2)
Co(2)-Co(1)-Co(2')	91.2(6)			Zn(3)-Zn(2)-Zn(1)	90.37(2)
Co(1)-Co(2)-Co(1')	88.7(1)			Zn(2)-Zn(1)-Zn(4)	89.64
				Zn(1)-Zn(4)-Zn(3)	90.32(2)
				Zn(4)-Zn(3)-Zn(2)	89.62(2)

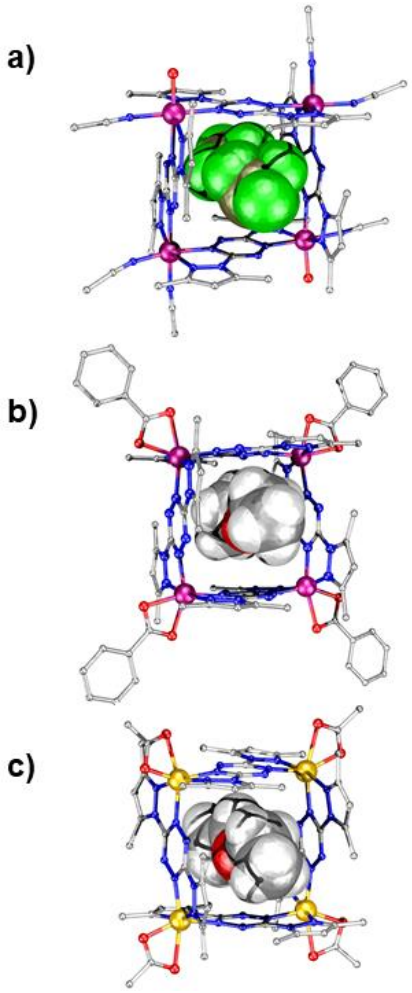

Figure 3.1. Molecular structure of **1** (a), **2** (b) and **3** (c) highlighting the molecule architecture and guest molecules, where two BF_4^- anions are placed inside cavity of **1** and diethyl ether molecules in **2** and **3**. The metal ions at the edge of the molecular square in **1** and **2** are Co(II) while **3** is Zn(II). Hydrogen, solvent and counter ions were omitted for clarity.

In **3**, the Zn metal ions are crystallographically independent, thus resulting in slightly different interatomic distances and angles. This is evident in the Zn···Zn···Zn angles, which range from 89.62° – 90.37°; slightly deviating from the perfect square seen in compound **2** but consistent with **1** (Table 3.4). The packing arrangement of **3** is also governed by non-covalent interactions of C-H···π, between pyrazolyl and acetate groups as well as interactions between the tetrazine rings and toluene solvent molecules.

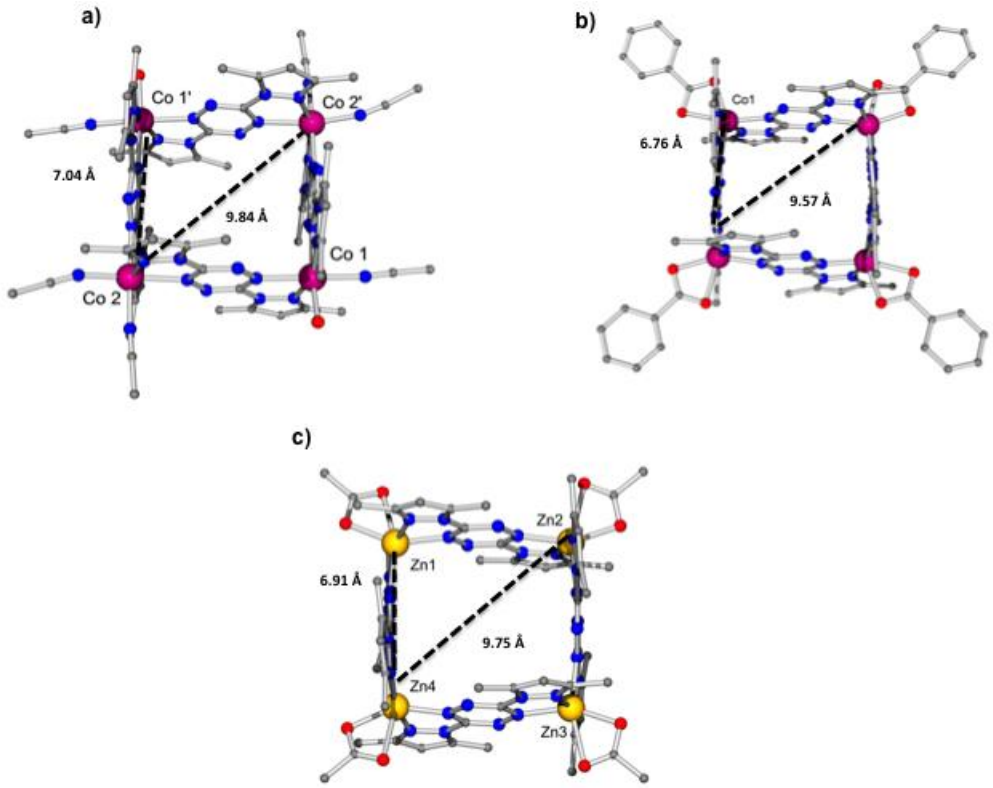

Figure 3.2. Ball-and-stick molecular structure of **1**(a), **2**(b) and **3**(c) emphasizing the cage topology and dimensions. The dashed lines indicate the distance between the metal ions through the ligand and across the cavity. H-atoms and solvent molecules were omitted for clarity. Code color: Co: pink, Zn: yellow, C: grey, N: blue, O: red.

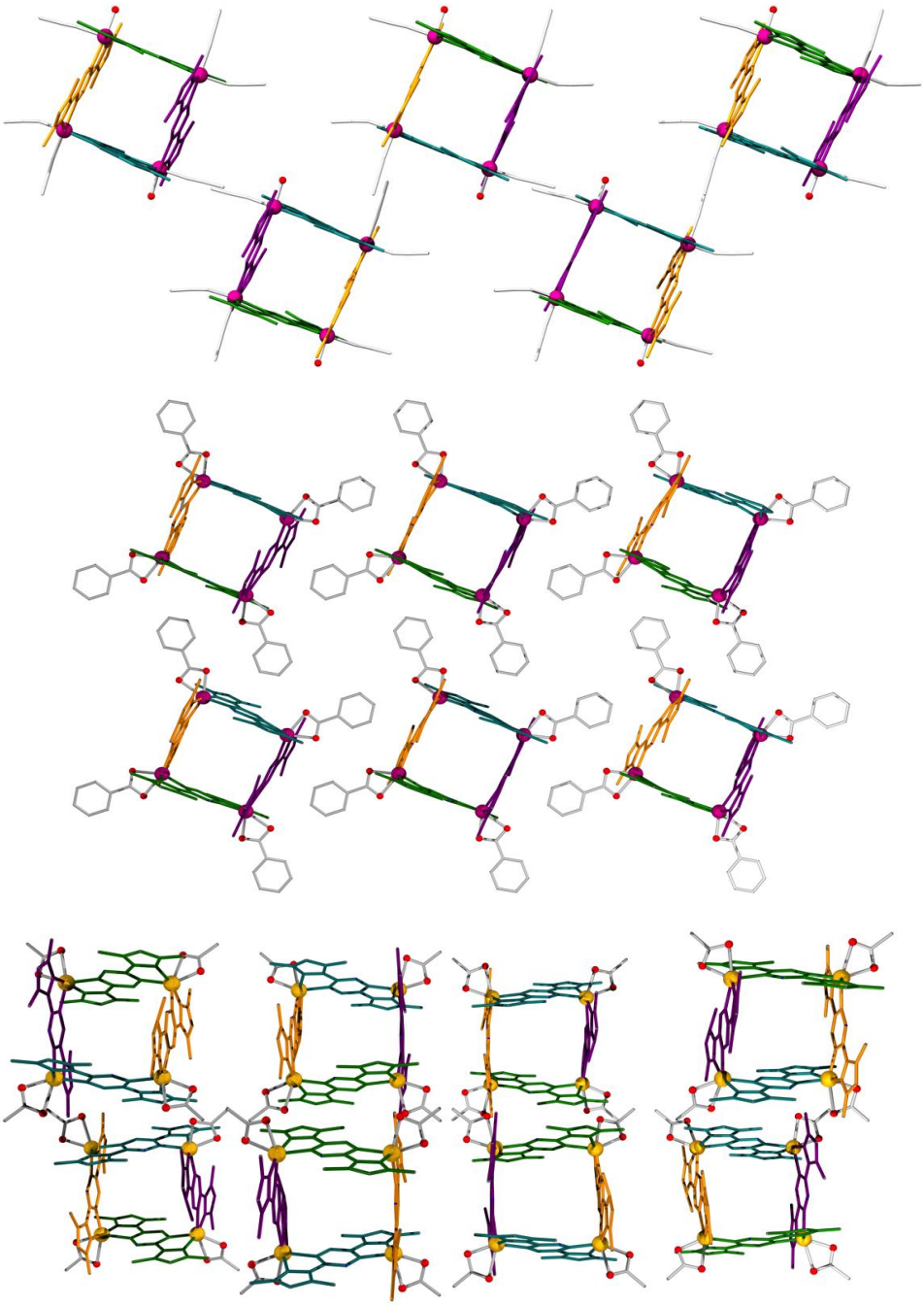

Figure 3.3. Ball-and-stick packing crystal structure of **1** (top), **2** (middle) and **3** (bottom) along the *c*-axis. The ligand colours help to highlight the crystal chirality. H-atoms and solvent molecules were omitted for clarity. Code color: Co: pink, Zn: yellow, O: red.

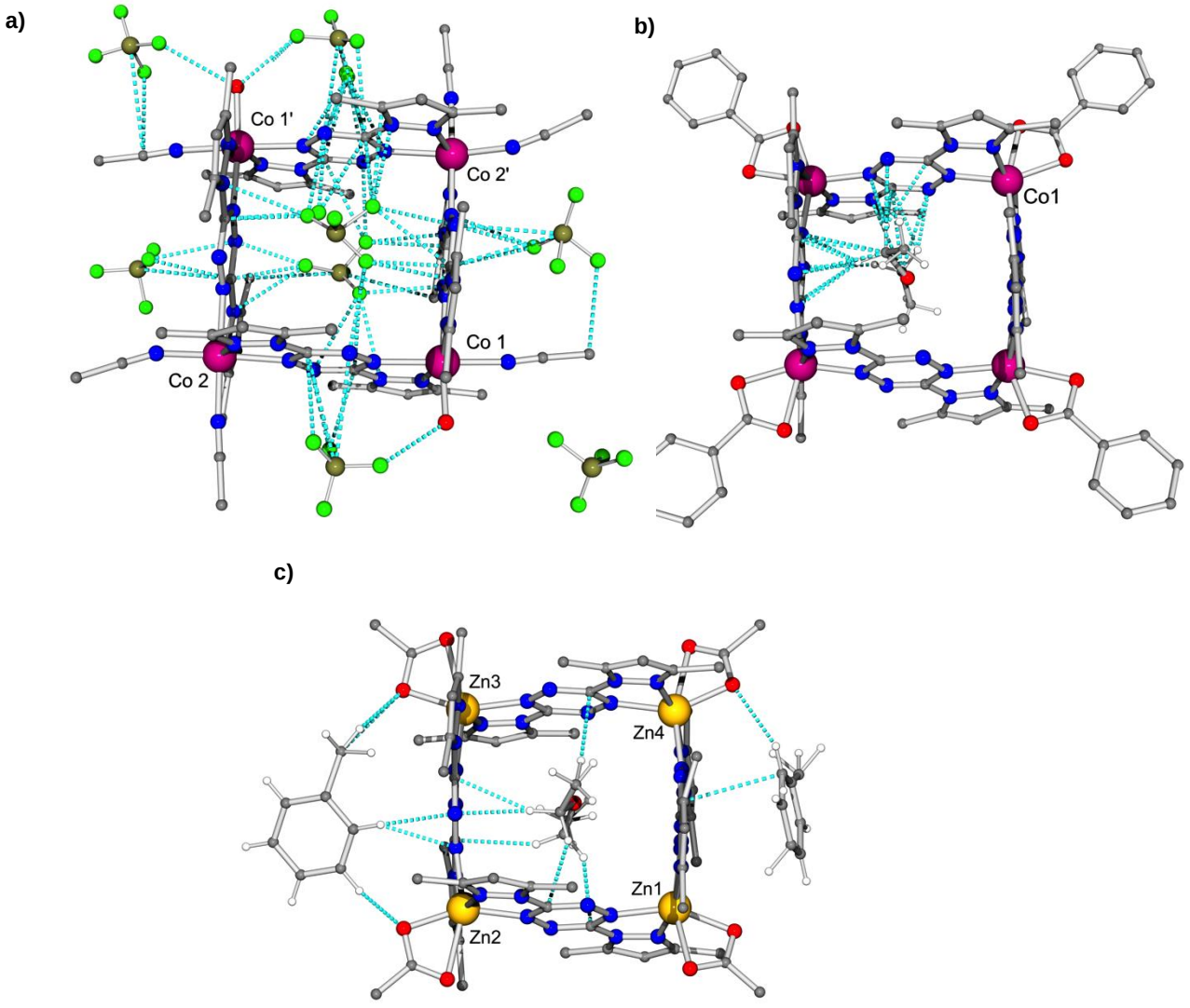

Figure 3.4. Ball-and-stick view of **1** (a), **2** (b) and **3** (c) replace A highlighting the critical role of short contacts in cage formation. The blue dashed lines indicate the non-covalent interactions. Code color: Co: pink, Zn: yellow, C: grey, N: blue, O: red, F: light green, B: dark green.

The presence of bpytz radicals are supported by the crystallographic structural changes observed in the tetrazine core through the elongation of the azo N-N bond distances from 1.32 Å to 1.36 Å. Although unexpected due to the absence of a reducing agent, the reduction of tetrazine-based ligands upon coordination in different synthetic conditions has been previously shown in the literature.[12b,17] This reduction is likely to occur due to the presence of higher electron density in the four nitrogen atoms of the 1,2,4,5-tetrazine core that results in a very low-lying π* orbital and electron deficiency at carbon atoms in the 3 and 6 position of the ring . These two effects are likely responsible for the facile reduction of the ring and the possible formation of a stable radical.[11a]

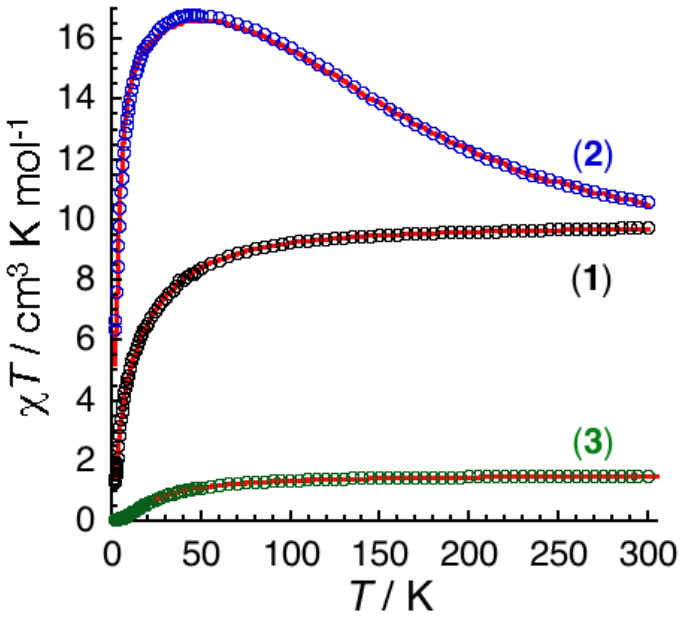

Figure 3.5. Variable-temperature dc magnetic susceptibility (χ = *M/H* per mole of compounds) data for **1** (black), **2** (blue) and **3** (green) shown as a plot of χT *vs T*, collected under an applied field of 0.1 T from 300 to 1.8 K. The solid line is the best fit obtained with the fitting parameters explained in the text.

In order to elucidate the strength and the nature of the magnetic interactions between the spin carriers, direct current (dc) magnetic susceptibility (χ) of all three compounds were

measured in an applied field of 1000 Oe and can be seen as χT *vs. T* in Figure 3.5. For compound **1**, as the temperature decreases from 300 to 1.8 K, the χT decreases gradually from 10.2 cm^3Kmol^{-1} to reach a minimum value of 1.43 cm^3Kmol^{-1} indicative of dominant antiferromagnetic interactions between the high-spin (HS) Co(II) (Since the Co metal ions $3d^7$ are placed in a octahedral geometry the expected total spin are S = 3/2 which is high-spin state with maximum amount of unpaired electrons or the opposite, low-spin S = ½. If the theoretical magnetic susceptibility χ = S(S+1)/2 is calculated using S=1/2, the magnetic susceptibility is not even close to the experimental values, while when calculated using high-spin state, the value is in good agreement with the experimental values at room temperature. Therefore, this system is a high-spin Co(II) with five electrons at T_{2g} state and two at e_g state) centers leading to a singlet ground state. The observed χT value at 300 K is higher than the expected spin-only value of 7.5 cm^3Kmol^{-1} for four non-interacting HS Co(II) ions. However, this is commonly observed for octahedral HS Co(II) species due to unquenched 1st order orbital angular momentum of d^7 Co(II).[18]

To quantify the exchange interactions between the spin carriers, the experimental data (χT *vs. T* and *M* vs. *H* simultaneously) were fitted using the program *PHI*.[19] Using the simplified Hamiltonian, $H = -2J(S_1 \cdot S_2 + S_2 \cdot S_3 + S_3 \cdot S_4 + S_1 \cdot S_4)$ (assuming the diagonal dipole-dipole contribution to be negligible) the following parameters J/hc = -0.64(5) cm^{-1}, g = 2.33(5) and D = +14.81(5) cm^{-1} were obtained. It is noteworthy that during the fit, the *g* factor and the axial zero-field splitting parameter (*D*) were allowed to vary. The obtained small negative $J_{Co\text{-}Co}$ value is indicative of weak antiferromagnetic exchange interaction *via* the central non-reduced tetrazine motif of the bpytz ligand, thus confirming previous reports by Dunbar and co-workers. [20]

Although the tetrazine ligand in its non-reduced form seems to be a poor mediator for magnetic exchange interactions, recent studies on reduced tetrazine indicate that it acts as a highly delocalized radical anion that strongly mediates exchange coupling with the metal spins.[12] As such, by fine-tuning the reaction conditions (i.e., use of benzoate metal salts instead of BF_4^-) complex **2** with bridging $bpytz^{\bullet-}$ radical anion was isolated. The dc susceptibility studies on **2** (Figure 3.5) exhibit a drastic change in the magnetic behavior; the χT product continuously increases (from 10.5 cm^3 K mol^{-1} at 300 K) with decreasing

temperature to reach a maximum value of 16.8 cm^3 K mol^{-1} at 46 K before decreasing rapidly to reach a minimum value of 6.4 cm^3 K mol^{-1} at 1.85 K. To probe the nature and the strength of the magnetic interactions between the spin carriers, *PHI* was employed with a simple Hamiltonian that takes in to account only one $J_{rad\text{-}Co}$ and assumed the Co···Co exchange parameter to be negligible (as seen in **1**). As in the case of **1**, we also included *D* and *g* parameters of the Co(II) ions to vary while fixing g_{rad} to 2.00. The best fits afforded a large $J_{rad\text{-}Co}$ value of -118(1) cm^{-1}, g_{Co} = 2.46(5) and D = + 8.5(3) cm^{-1}. This large negative *J* value is indicative of strong antiferromagnetic exchange between the radicals and the Co(II) ions, thus leading to an S = 4 spin ground state for **2**. Surprisingly, this $J_{rad\text{-}Co}$ value is two fold larger than the one reported recently for bptz radical bridged [Co_4] square.[12c] This is likely due to shorter Co-N_{rad} distances (average distance of 2.02 Å) in **2** compared to 2.06 Å in the reported example, thus affording better orbital overlap and larger coupling constants.[21] The simulation good fit of the χT *vs. T* and *M vs. H* (Figure 3.6) data reinforces the accuracy of the parameters values.

To further validate the presence of the radical in **2** and probe the possible exchange interaction between the radicals, we investigated the magnetic properties of the [Zn_4] analogue (**3**). The χT product of 1.48 cm^3Kmol^{-1} at 300 K is consistent with the presence of four uncoupled S = ½ spins residing on the tetrazine radicals. Upon decrease of the temperature, the χT product remains constant down to 50 K, below which a rapid decrease can be observed with a minimum value of 0.06 cm^3 K mol^{-1} at 1.8 K. Such behavior is indicative of antiferromagnetic interactions between the tetrazine radicals with a singlet ground state for the square complex. Fitting of the data using Kambe's coupling method yielded a coupling constant of $J_{rad\text{-}rad}/hc$ = -15.9(5) cm^{-1} and a g_{rad} value of 1.99(5). It is noteworthy that this observed $J_{rad\text{-}rad}$ value indicates that the interactions between radicals through the diamagnetic Zn metal ions in **3** are stronger than the interactions occurring between the Co(II) ions in **1**.

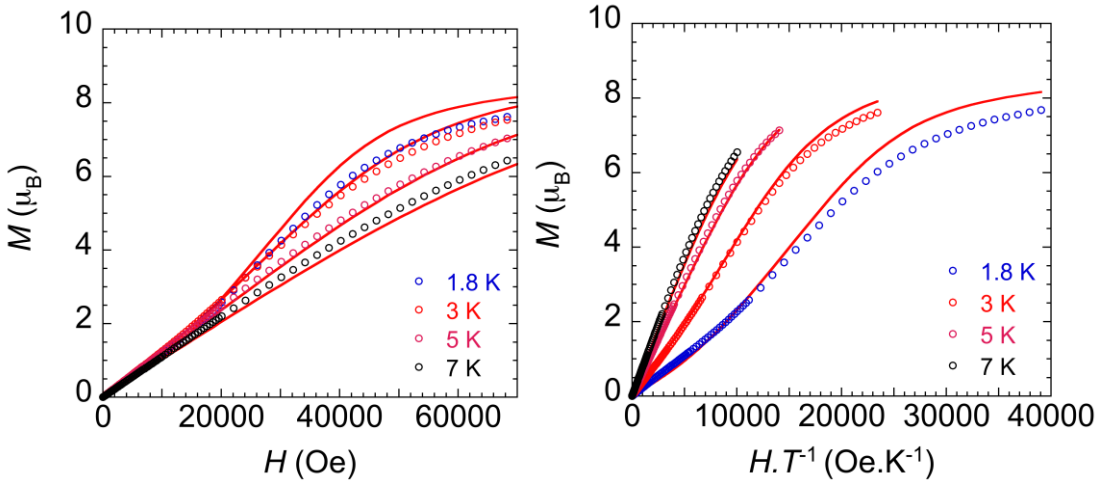

Figure 3.6. Field dependence of the magnetization plots as *M vs. H* and *M vs. HT*$^{-1}$ for **1**.

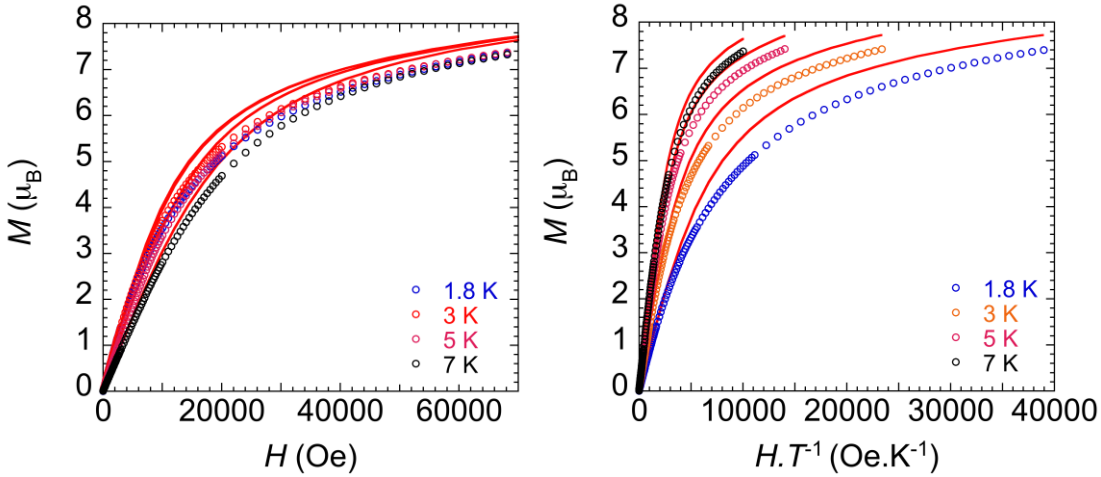

Figure 3.7. Field dependence of the magnetization plots as *M vs. H* and *M vs. HT*$^{-1}$ for **2**.

3.5. Conclusion

In summary, the presented results highlight the merits of using appropriate co-ligands and counter ions in the supramolecular approach to control the redox property of the bpytz ligand. Remarkably, the reported compounds were isolated under aerobic conditions using non-dried solvents, hydrated metal salts and, more importantly, without the employment of a reducing agent. The analysis of magnetic properties demonstrates that a strong radical-Co(II) exchange coupling can be achieved through the use of the highly delocalized $bpytz^{\bullet-}$ radical anion. The lessons learned from this versatile air stable coordination chemistry of reduced tetrazine cores will allow us to envision new air stable, strongly coupled, polynuclear complexes that act as one single entity with a giant spin ground state at room temperature.

3.6. References

1 R. S. Forgan, J. P. Sauvage, J. F. Stoddart, *Chem. Rev.*, 2011, **111**, 5434-5464.

2 R. Chakrabarty, P. S. Mukherjee, P. J. Stang, *Chem. Rev.*, 2011, **111**, 6810-6918.

3 L. M. Greig, D. Philp, *Chem. Soc. Rev.*, 2001, **30**, 287-302.

4 K. K. Turoverov, I. M. Kuznetsova and V. N. Uversky, *Prog Biophys Mol Biol*, 2010, **102**, 73-84.

5 V. Receveur-Brechot, J. M. Bourhis, V. N. Uversky, B. Canard, S. Longhi, *Proteins: Struct., Funct., Bioinf.*, 2006, **62**, 24-45.

6 (a) R. Vilar, *Angew. Chem. Int. Ed.,* 2003, **42**, 1460-1477. (b) H. T. Chifotides, I. D. Giles, K. R. Dunbar, *J. Am. Chem. Soc.*, 2013, **135**, 3039-3055. (c) D. M. Wood, W. Meng, T. K. Ronson, A. R. Stefankiewicz, J. K. M. Sanders, J. R. Nitschke, *Angew. Chem. Int. Ed*., 2015, **54**, 3988-3992.

7 X. C. Huang, J. P. Zhang, X. M. Chen, *J. Am. Chem. Soc.*, 2004, **126**, 13218-13219.

8 C. P. Li, M. Du, *Chem. Comm.*, 2011, **47**, 5958-5972.

9 X. C. Huang, D. Li, X. M. Chen, *CrystEngComm*, 2006, **8**, 351-355.

10 W. Wang, Y. X. Wang, H. B. Yang, *Chem. Rev. Soc.*, 2016, **45**, 2656-2693.

11 (a) W. Kaim, *Coord. Chem. Rev.*, 2002, **230**, 127-139. (b) B. L. Schottel, H. T. Chifotides, K. R. Dunbar, *Chem. Soc. Rev*., 2008, **37**, 68-83. (c) H. T. Chifotides, K. R. Dunbar, *Acc. Chem. Res*., 2013, **46**, 894-906. (d) D. A. Safin, A. Pialat, A. A. Leitch, N. A. Tumanov, I. Korobkov, Y. Filinchuk, J. L. Brusso, M. Murugesu, *Chem. Comm.*, 2015, **51**, 9547-9550. (e) B. S. Dolinar, S. Gómez-Coca, D. I. Alexandropoulos, K. R. Dunbar, *Chem. Commun*., 2017, **53**, 2283-2286.

12 (a) T. J. Woods, M. F. Ballesteros-Rivas, S. M. Ostrovsky, A. V. Palii, O. S. Reu, S. I. Klokishner, K. R. Dunbar, *Chem. Eur. J.*, 2015, **21**, 10302-10305. (b) M. A. Lemes, G. Brunet, A. Pialat, L. Ungur, I. Korobkov, M. Murugesu, *Chem. Commun*, 2017, **53**, 8660-8663. (c) D. I. Alexandropoulos, B. S. Dolinar, K. R. Vignesh, K. R. Dunbar, *J. Am. Chem. Soc*. 2017, **139**, 11040-11043. (d) T. J. Woods, H. D. Stout, B. S. Dolinar, K. R. Vignesh, M. F. Ballesteros-Rivas, C. Achim, K. Dunbar, *Inorg. Chem*. 2017, DOI**:** 10.1021/acs.inorgchem.7b01812.

13 (a) N. G. R. Hearns, K. E. Preuss, J. F. Richardson, S. Bin-Salamon, *J. Am. Chem. Soc*., 2004, **126**, 9942-9943. (b) L. Norel, F. Pointillart, C. Train, L-M. Chamoreau, K. Boubekeur, Y. Journaux, A. Brieger, D. J. R. Brook, *Inorg. Chem*., **2008**, 47, 2396-2403. (c) D. J. R. Brook, C. J. Richardson, B. C. Haller, M. Hundley, G. T. Yee, *Chem. Commun*. 2010, **46**, 6590. (d) J. D. Rinehart, M. Fang, W. J. Evans, J. R. Long, *J. Am. Chem. Soc*. 2011, **133**, 14236-14239. (e) S. Fortier, J. J. Le Roy, C-H. Chen, V. Vieru, M. Murugesu, L. F. Chiboratu, D. J. Mindiola, K. G. Caulton, *J. Am. Chem. Soc.,* 2013, **135**, 14670-14678. (f) S. Demir, I-R. Jeon, J. R. Long, T. D. Harris, *Coord. Chem. Rev*., 2015, **289**, 149-176. (g) J. A. DeGayner, I-R. Jeon, T. D. Harris, *Chem. Sci*., 2015, **6**, 6639-6648.

14 J. Tong, S. Demeshko, M. John, S. Dechert, F. Meyer, *Inorg. Chem.*, 2016, **55**, 4362-4372.

15 (a) R. Feyerherm, A. Loose, T. Ishida, T. Nogami, J. Kreitlow, D. Baabe, F. J. Litterst, S. Sullow, H. H. Klauss, K. Doll, *Phys. Rev. B*, 2004, **69**, 8. (b) N. Brener, F. Ben Amar, P. Bidaud, *Int. J. Rob. Res.*, 2008, **27**, 279-297. (c) A. Dey and E. Pidcock, *CrystEngComm*, 2008, **10**, 1258-1264. (d) R. W. Hogue, S. Dhers, R. M. Hellyer, J. Luo, G. S. Hanan, D. S. Larsen, A. L. Garden, S. Brooker, *Chem. Eur. J.,* 2017, **23**, 14193 – 14199.

16 S. Sharma, M. Chauhan, A. Jamsheera, S. Tabassum, F. Arjmand, *Inorg. Chim. Acta.*, 2017, **458**, 8-27.

17 (a) M. Schwach, H. D. Hausen, W. Kaim, *Inorg. Chem.*, 1999, **38**, 2242- 2243. (b) M. Glockle, K. Hubler, H. J. Kummerer, G. Denninger, W. Kaim, *Inorg. Chem.*, 2001, **40**, 2263-2269. (c) K. Parimal, S. Vyas, C. H. Chen, C. M. Hadad, A. H. Flood, *Inorg. Chim. Acta*, 2011, **374**, 620-626. (d) S. K. Tripathy, M. van der Meer, A. Sahoo, P. Laha, N. Dehury, S. Plebst, B. Sarkar, K. Samanta, S. Patra, *Dalton Trans.*, 2016, **45**, 12532-12538.

18 (a) J. Vallejo, I. Castro, R. Ruiz-García, J. Cano, M. Julve, F. Lloret, G. De Munno, W. Wernsdorfer, E. Pardo, *J. Am. Chem. Soc*., 2012, **134**, 15704-15707. (b) Y-Y. Zhu, C. Cui, J-H. Jia, X. Guo, C. Gao, K. Qian, S-D. Jiang, B-W. Wang, Z-M. Wang, S. Gao, *Chem. Sci*. 2013, **4**, 1802-1806. (c) J. O. Moilanen, N. F. Chilton, B. M. Day, T. Pugh, R. A. Layfield*, Angew. Chem. Int. Ed.,* 2016, **55**, 5521-5525. (d) D.

Schweinfurth, S. Demeshko, M. G. Sommer, S. Dechert, F. Meyer, B. Sarkar, *Eur. J. Inorg. Chem.* 2016, **15**, 2581-2585.

19 N. F. Chilton, R. P. Anderson, L. D. Turner, A. Soncini, K. S. Murray, *J. Comput. Chem*., 2013, **34**, 1164-1175.

20 C. S. Campos-Fernandez, R. Clérac, J. M. Koomen, D. H. Russell, K. R. Dunbar, *J. Am. Chem. Soc*., 2001, **123**, 773-774.

21 (a) M. Kato, Y. Muto, *Coord. Chem. Rev*., 1988, **92**, 45-83. (b) J. A. McCleverty, M. D. Ward, *Acc. Chem. Res*., 1998, **31**, 842-851. (c) Y-F. Zeng, X. Hu, F-C. Liu, X-H. Bu, *Chem. Soc. Rev*., 2009, **38**, 469-480.

Chapter 4

Intramolecular pancake bonding in an unprecedented air-stable {Dy_2} single-molecule magnet

4.1. Abstract

A planar easily reducible 3,6-bis(3,5-dimethyl-pyrazolyl)-1,2,4,5-tetrazine (bpytz) lead to the formation of a dinuclear $[Dy^{III}_2(bpytz)(\mu\text{-TMHD})_6]\cdot 4(C_6H_6)$ (**1**) and its unprecedented congener $[Dy^{III}_2(\mu\text{-bpytz}^{\bullet-})_2(TMHD)_4]$ (**2**) (TMHD = 2,2,6,6-tetramethyl-3,5-heptanedionate). In **2**, two $bpytz^{\bullet-}$ radical anions are strongly antiferromagnetically coupled (-4388 cm^{-1}) to form a unique pancake bond. Both complexes exhibit SMM behaviour under an applied dc field of 600 Oe. As a result of the above investigation, a manuscript has been prepared and will be published soon: Lemes, M. A.; Zhang, Y.; Gabidullin, B.; Moilanen, J.; Brusso, J.; Murugesu, M.*, Manuscript in preparation*, **2019**.

4.2. Introduction

Sharing of electrons is the fundamental principle behind the formation of covalent bonds. The resulting single or multiple bonds are commonly encountered while π-radical bonds, namely pancake bonds are unusual. When planar closed shell aromatic molecules form π-stacks, the distances between the interacting molecules tend to be larger than the van der Waals radii. Whereas when open-shell planar aromatic molecules interact through non-covalent interactions, pancake bonded π-radical dimers are likely to form. Kertesz[1] defines pancake bonding as part of the π-stacking interaction group where such contact occurs between planar and aromatic structures with the interactions being parallel and strong. In this way, the characteristics that better describe such unusual intermolecular interaction are presented by: (a) radical structures in which their interactions occur through the highly delocalized π-electrons in their single occupied molecular orbitals (SOMO). (b) The distances of the interactions are shorter than the van der Waals contact. (c) The stabilization of the bond is attributed to the mix of the SOMO orbitals that results in a direct and strong overlap of preferential atom-to-atom interaction (strongly directional). (d) This kind of interaction contain characteristic similar to covalent bond (the electrons are shared

between the radicals).[1] Therefore, the resultant high electron density frameworks are interesting molecular-based materials for spintronics in which its tunability may disclose exceptional physical properties in molecules that behave as single-molecule magnets (SMM).[1,2]

The fine-tuning of magnetic properties in molecular-based magnets, known as SMMs remain a significant challenge.[3] Through different approaches scientists have shown that minimal modification in the crystal field symmetry,[4] coordination environment,[5] and electronic structure[6] can greatly affect SMM performance. In particular, most of the strategies have targeted magnetic anisotropy to achieve large effective energy barriers to the relaxation of the magnetization (U_{eff}). However, most of the designs fail due to the occurrence of fast relaxation processes. Thus, applying radical-bridge ligands to promote strong magnetic exchange coupling represents a potential model to minimize fast relaxation of magnetization and achieve substantial anisotropy barriers.[7]

In this way, tetrazine-based frameworks represent ideal candidates as multi-redox ligand bridges for improving magnetic communication between paramagnetic units, i.e. spins carriers. Their capacity to uptake an electron upon coordination can afford a variety of polymetallic air-stable radical complexes. These frameworks are interesting not only because of their ability to accommodate multiple metal ions but also due to their fascinating electronic structures.[8]

The electronic properties of such ligands arise from the presence of four electronegative N atoms in the 1,2,4,5-tetrazine (Tz) ring and a low-lying π* orbital. Recently we have demonstrated the efficiency of Tz anions for obtaining stable radical complexes and enhancing magnetic exchange coupling in *d*-block complexes.[8,9] With this in mind, we replicated this same approach to design and synthesize 4*f*-element based complexes containing tetrazine-derived ligands. While 4*f* systems do not exhibit the same magnitude of exchange coupling as *d*-block metal complexes, the diffuse nature of the radical orbitals compensated for the shielded 4*f* electrons and therefore promoted significant electronic communication.[7,9,10]

Therefore, we judiciously chose the nitrogen-rich molecule bpytz as a bridging ligand for two lanthanide metal ions. Based on our previous results, this framework has

demonstrated its tendency to form bimetallic complexes, while facilitating effortless one electron reductions (with or without a reducing agent), under aerobic conditions.[9b,I] Herein we describe a dinuclear lanthanide complex with intramolecular π-dimerization and field induced SMM behaviour. To the best of our knowledge this is the first metal complex exhibiting intramolecular pancake bond in coordination compounds. Single crystal X-ray diffraction, SQUID magnetometry along with theoretical studies elucidated the physical properties of this unprecedented molecule in terms of assembly and electronic structure. [5]

4.3. Experimental

4.3.1. Materials

Except for the reaction of complex **2**, all manipulations were carried out under aerobic/ambient conditions. Chemicals were purchased from TCI, Alfa Aesar, and Stream Chemicals, and used without further purification.

4.3.2. Synthesis

3,6-bis(3,5-dimethyl-pyrazolyl)-1,2,4,5-tetrazine (bpytz):

The ligand was prepared according to the literature (For more information, please see Reference 27 in the Chapter 1).

Synthesis of [Dy^{III}_2(μ-bpytz)$(TMHD)_6$]·4(C_6H_6) (1)

The synthesis of **1** was carried out by combining bpytz (0.125 mmol, 34 mg) and $Dy(TMHD)_3$ (0.125 mmol, 84 mg) in benzene (6 mL). The brownish suspension formed after few minutes stirring was slow diffused with CH_3CN. Dark red crystals suitable for single crystal X-ray crystallography of **1** were obtained after 24h. Yield = 85%. Selected IR (cm^{-1}): 3233.69 (s), 1653.55 (s), 1580.16 (m), 1497.71 (m), 1436.65 (m), 1378.44 (s), 1251.30 (m), 1204.48 (m), 1118.05 (s), 1076.52 (m), 1040.94 (w), 780.98 (m), 682.95 (m), 671.21 (m). Anal. Calc. for $C_{102}H_{152}Dy_2N_8O_{12}$: C, 61.03%; H, 7.63%; N, 5.58%; Found: C, 60.07%; H, 7.48%; N, 5.50%.

Synthesis of [Dy^{III}_2(μ-bpytz$^{\bullet-}$)$_2$$(TMHD)_4$] (2)

Synthesis of **2** was performed under inert atmosphere in a glovebox. All the starting materials were previously dried, and the solvents degassed. The reaction was carried out

by mixing bpytz (0.125 mmol, 34 mg), $CoCp_2$ (0.125 mmol, 21 mg) and, $Dy(TMHD)_3$ (0.125 mmol, 84 mg) in benzene (6 mL). The green suspension was left to stir for several minutes and the resulting solution was slow diffused with CH_3CN. Crystals suitable for single crystal X-ray crystallography of **1** were collected after two days. Yield = 80%. Selected IR (cm^{-1}): 2745.26 (m), 1584.65 (s), 1497.12 (s), 1459.78 (m), 1442.21 (m), 1419.73 (m), 1375.12 (s), 1282.93 (s), 1095.83 (w), 1049.98 (b), 983.94 (m), 835.33 (m), 784.19 (m), 593.24 (w), 588.65 (m). Anal. Calc. for $C_{68}H_{104}Dy_2N_{16}O_8$: C, 51.09%; H, 6.56%; N, 14.02%; Found: C, 51.10%; H, 6.61%;N, 14.12%.

4.3.3. Physical measurements

X-ray crystallography

Suitable crystals were mounted on a glass fiber. A Bruker APEX-II CCD device was used to collect unit cell and intensity data using graphite Mo Kα radiation (λ = 0.71073). The data reduction included a correction for Lorentz and polarization effects, with an applied multiscan absorption correction (SADABS). The crystal structure was solved and refined using the SHELXTL v.6.12 program suite.[11] Direct methods yielded all non-hydrogen atoms, which were refined with anisotropic thermal parameters. All hydrogen atom positions were calculated geometrically and were riding on their respective atoms.

Spectroscopy analysis

Solid-state infrared spectra were obtained on a Varian 640 FT-IR spectrometer in the 400-4000 cm^{-1} range.

4.4. Results and discussion

The reaction of $[Dy^{III}_2(bpytz)(\mu\text{-}TMHD)_6]\cdot 4(C_6H_6)$ (**1**) was carried out under aerobic conditions by mixing equimolar amounts of $Dy(TMHD)_3$ and bpytz in benzene. The resultant dark brown solution was left in an CH_3CN bath where suitable orange block-like single crystals were obtained in 85% yield. It is important to note that the same reaction was performed for **1** under anaerobic conditions and yields the same product. Under inert atmosphere, an equimolar combination of bpytz (0.125 mmol, 34 mg), $CoCp_2$ (0.125

mmol, 21.1 mg) and Dy(TMHD)$_3$ (0.125 mmol, 84 mg) in benzene (6 mL) results in a dark-green solution (Scheme 4.1). Crystallization from CH_3CN diffusion yields small green block-like crystals of the complex [Dy^{III}_2(μ-bpytz$^{\bullet-}$)$_2$(TMHD)$_4$] (**2**) in 80% yield.

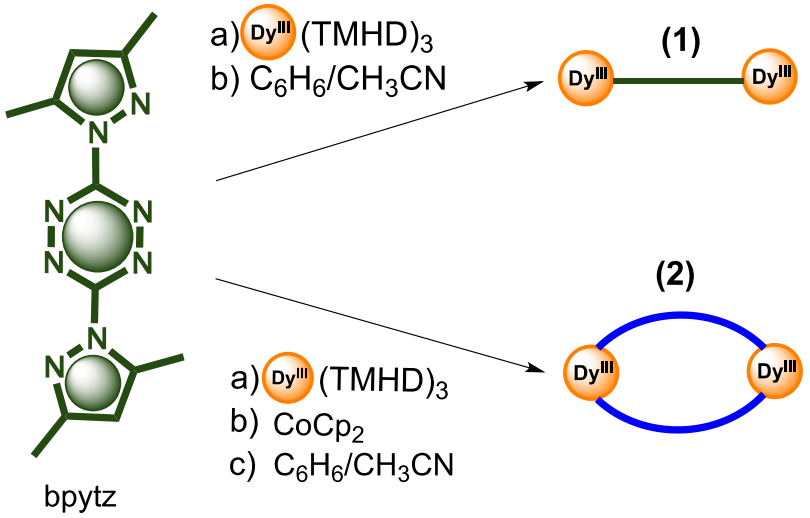

Scheme 4.1. Synthesis of **1** and **2**. The green line indicates the neutral ligand bpytz and blue lines the anion bpytz$^{\bullet-}$.

Table 4.1. Crystallography data of the complex **1** and **2**

	1	**2**
Empirical formula	$C_{102}H_{152}Dy_2N_8O_{12}$	$C_{68}H_{104}Dy_2N_{16}O_8$
Formula weight	2007.31	1598.67
Crystal system	Trigonal	Trigonal
Space group	$P\bar{1}$	$P3_221$
a/Å	12.166(8)	17.4409(13)
b/Å	13.986(10)	17.4409(11)
c/Å	16.878(12)	22.8542(13)
α/ °	101.799(9)	90
β/ °	96.760(9)	90
γ/ °	103.238(9)	120
V/ Å^3	2695(3)	5814.5(10)
Z	1	3
T/K	200(2)	201(2)
Radiation	Mo-K$_\alpha$	Mo-K$_\alpha$
Wavelength/ Å	0.71073	0.71073
Dc/mg m^{-3}	1.237	1.370
μ/mm^{-1}	1.433	13.121
Reflections collected	97331	92658
Goodness-of-fit on F^2	1.020	1.024
R1,wR2 (>2σ(I))[a]	0.0593, 0.0978	0.0381, 0.0668

[a] $R_1 = \Sigma||F_0| - |F_c||/\Sigma|F_0|$. $wR_2 = (\Sigma[w(F_0^2 - F_c^2)^2]/\Sigma[w(F_0^2)^2])^{1/2}$.

Table 4.2. Selected bond lengths (Å) for **1** and **2**.

1		**2**	
C(6)-N(3)	1.334(5)	Dy(1)-O(1)	2.277(3)
C(6)-N(4)	1.342(5)	Dy(1)-O(4)	2.286(3)
C(6)-N(2)	1.382(5)	Dy(1)-O(3)	2.292(4)
Dy(1)-O(6)	2.275(3)	Dy(1)-O(2)	2.307(3)
Dy(1)-O(4)	2.278(3)	Dy(1)-N(3)	2.516(3)
Dy(1)-O(3)	2.285(3)	Dy(1)-N(1)	2.553(4)
Dy(1)-O(1)	2.290(3)	Dy(1)-N(6)#1	2.556(4)
Dy(1)-O(2)	2.296(3)	Dy(1)-N(8)#1	2.569(4)
Dy(1)-O(5)	2.334(3)	N(1)-N(2)	1.375(5)
Dy(1)-N(3)	2.658(4)	N(3)-N(4)	1.386(6)
Dy(1)-N(1)	2.678(4)	N(5)-N(6)	1.396(5)
N(1)-N(2)	1.382(4)	N(6)-Dy(1)	2.556(4)
N(3)-N(4)	1.320(5)	N(7)-N(8)	1.382(6)
N(4)-C(6)	1.342(5)	N(8)-Dy(1)	2.569(4)

Table 4.3. Selected angles (°) for **1** and **2**.

1		**2**	
O(6)-Dy(1)-O(2)	78.43(11)	O(1)-Dy(1)-N(3)	128.31(12)
O(4)-Dy(1)-O(2)	82.35(12)	O(4)-Dy(1)-N(3)	77.23(12)
O(3)-Dy(1)-O(2)	83.49(12)	O(3)-Dy(1)-N(3)	115.67(13)
O(1)-Dy(1)-O(2)	72.64(12)	O(2)-Dy(1)-N(3)	152.81(14)
O(6)-Dy(1)-O(5)	73.56(10)	O(1)-Dy(1)-N(1)	81.82(13)
O(4)-Dy(1)-O(5)	75.93(11)	O(4)-Dy(1)-N(1)	109.37(13)
O(3)-Dy(1)-O(5)	114.50(11)	O(3)-Dy(1)-N(1)	75.21(14)
O(1)-Dy(1)-O(5)	137.68(10)	O(2)-Dy(1)-N(1)	144.02(14)
O(2)-Dy(1)-O(5)	145.31(11)	N(3)-Dy(1)-N(1)	62.61(13)
O(2)-Dy(1)-N(3)	147.57(10)	O(1)-Dy(1)-O(4)	153.54(13)
O(5)-Dy(1)-N(3)	66.30(10)	O(1)-Dy(1)-O(3)	86.82(13)
O(6)-Dy(1)-N(1)	84.02(11)	O(4)-Dy(1)-O(3)	73.71(12)
O(4)-Dy(1)-N(1)	149.81(11)	O(1)-Dy(1)-O(2)	73.29(13)
O(3)-Dy(1)-N(1)	121.76(11)	O(4)-Dy(1)-O(2)	84.99(12)
O(1)-Dy(1)-N(1)	65.79(11)	O(3)-Dy(1)-O(2)	77.82(15)
O(2)-Dy(1)-N(1)	123.25(12)	O(1)-Dy(1)-N(3)	128.31(12)
O(5)-Dy(1)-N(1)	73.90(11)	O(4)-Dy(1)-N(3)	77.23(12)
N(3)-Dy(1)-N(1)	60.15(11)	O(3)-Dy(1)-N(3)	115.67(13)
C(2)-N(1)-Dy(1)	131.3(3)	O(2)-Dy(1)-N(3)	152.81(14)
N(2)-N(1)-Dy(1)	118.9(2)	O(1)-Dy(1)-N(1)	81.82(13)
N(4)-N(3)-Dy(1)	118.7(2)	O(4)-Dy(1)-N(1)	109.37(13)
C(6)-N(3)-Dy(1)	122.6(3)	O(3)-Dy(1)-N(1)	75.21(14)
C(11)-O(1)-Dy(1)	134.9(3)	N(3)-Dy(1)-N(6)	62.70(11)
C(13)-O(2)-Dy(1)	135.0(3)	N(3)-Dy(1)-N(1)	62.61(13)

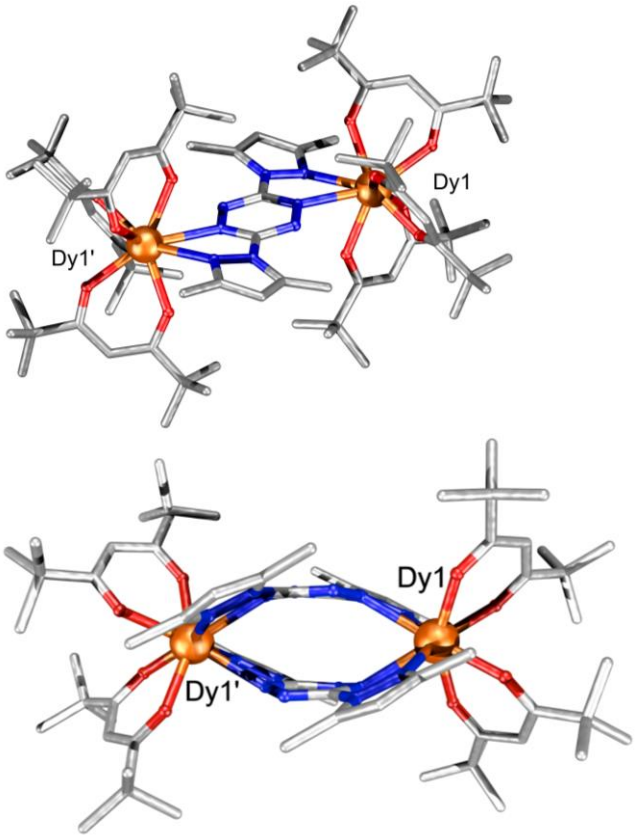

Fig. 4.1. Molecular structure of **1** (top) and **2** (bottom). Solvent molecule and hydrogen atoms were omitted for clarity. Color code. Dy (orange), C (gray), N (blue), O (red).

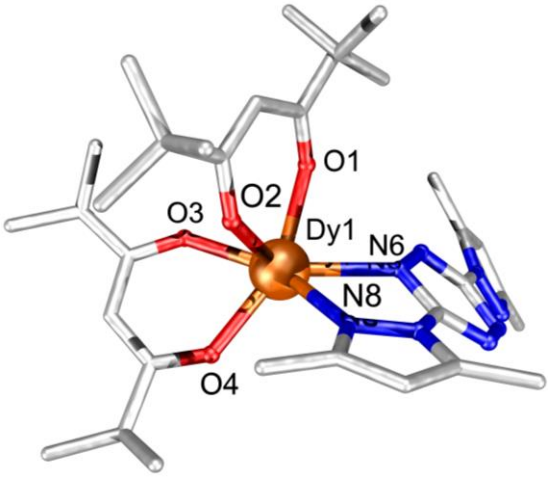

Figure 4.2. Asymmetric unit of **2** highlighting the coordinating environment of Dy(III) ion. Color code: Dy (orange), N (blue), O (red), C (grey). Hydrogen atoms and solvent molecules were omitted for clarity.

Single-crystal X-ray diffraction reveals that **1** crystallizes in the triclinic $P\bar{1}$ space group and **2** crystallizes in the trigonal $P3_221$ space group (Table 4.1; For bond distance and angles, see Tables 4.2 and 4.3). The asymmetric unit of **1** is comprised of one Dy metal ion, one bpytz, three TMHD and two benzene solvent molecules, while **2** shows one crystallographically independent Dy(III) ion, bpytz$^{\bullet-}$, and two TMHD co-ligands (Fig. 4.2). The complete molecular structure of **1** (Fig. 4.1 top) has only one bridging bpytz ligand (neutral) and six TMHD co-ligands. Likewise, the octacoordinated metal ions present in both complexes are placed in a square antiprismatic geometry as confirmed by Shape analysis (CSh),[12] with TMHD and bpytz contributing O and N donor atoms respectively. The central bpytz ligand of **1** is designated as neutral, based on charge balance considerations and inspection of the N-N bond distance in the tetrazine core (1.32 Å which is in agreement with the N-N bond length in the free ligand).[9a,b,e,f] The complete structure of **2** is a two-fold symmetric molecule formed by two Dy metal ions being bridged by two reduced bpytz ligands with four terminal TMHD co-ligands (Fig. 4.1 bottom). Each lanthanide in **2** is coordinated to four O donor atoms provided by the TMHD and four N atom donors from the radical-bridge ligands. Notably, the Dy1-N6-N3 angle of 147.23° exposes the flexibility of the tetrazine ring (Tz), most likely due to the presence of an additional electron. The relatively small N6'-Dy1-N3 angle of 62.62° formed by the assembly of the two bpytz ligands allows the Tz rings to face each other at a distance around 2.73 Å while the Dy···Dy intramolecular distance observed is 7.10 Å (Fig. 4.3 and 4.4). The Tz···Tz interplanar separation is smaller than those showing π-stacking interaction and larger than a typical covalent bond (Fig. 4.4). Thus, such structural and electronic arrangement indicate unprecedented intramolecular pancake bonding which potentially contributes to the overall magnetic communication in **2**.[1,2,13] Close inspection of the packing arrangement displays short intermolecular Dy···Dy distances of 12.11 Å, which could possibly prevent any dipolar magnetic interactions.[13c]

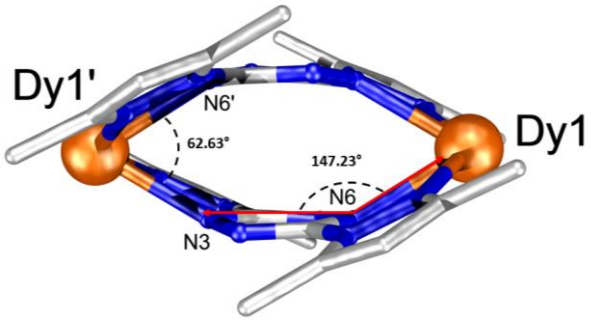

Figure 4.3. Molecular structure of **2** highlighting the angles N6'-Dy1'-N3 and Dy1-N6-N3 in the $(bpytz^{\bullet-})_2$ bridge. TMHD co-ligands, hydrogen atoms and solvent molecules were omitted for clarity. Color code: C (grey), N (blue), Dy(orange).

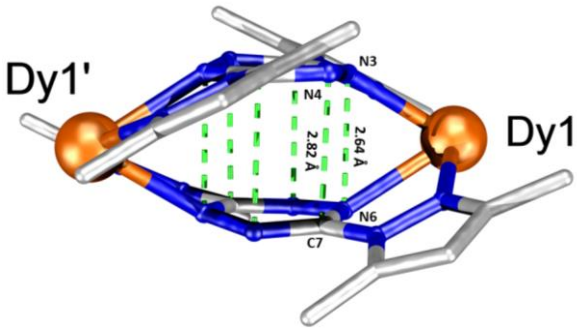

Figure 4.4. Intramolecular distances between the two reduced tetrazine rings in **2**. All C···N and N···N distances (green dashed lines) are 2.82 Å and 2.64 Å respectively. TMHD coligands, hydrogen atoms and solvent molecules were omitted for clarity. Color code: C (grey), N (blue), Dy (orange).

In an attempt to isolate **1** with a reduced ligand, several syntheses were performed, however no success was achieved. We believe the bpytz topology and the presence of bulky co-ligands (TMHD) prevent the formation of the single anion ligand bridge. The arrangement of the pyrazolyl and TMHD would end up shielding the tetrazine core, thus precluding any electrostatic interaction with a neighbouring counter ion that could balance the overall complex charge.[9a,c]

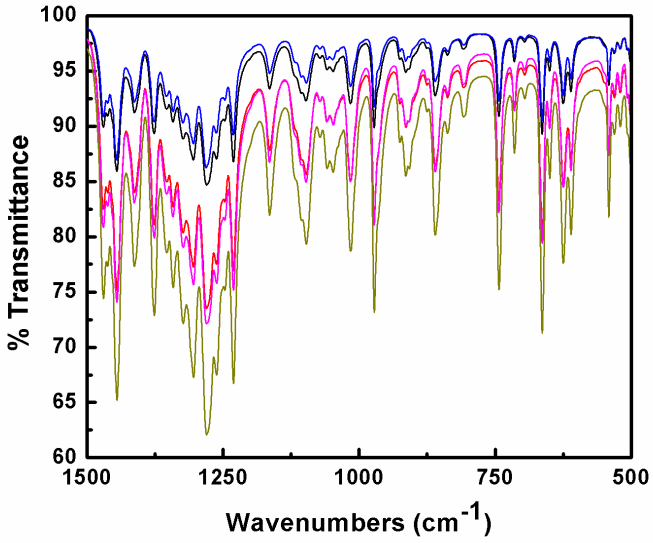

Figure 4.5. Solid-state infrared spectra of **2** measured over a period of 20 days.

The reduction of bpytz ligands in **2** is confirmed first by charge balance considerations. Since the four TMHD co-ligands contribute with total charge of 4–, the additional charge to stabilize the 6+ metal ions is provided by the two reduced bpytz ligands with a 1– charge each. Furthermore, the crystallographic changes observed in the tetrazine core through the elongation of the azo N-N bond distances from 1.32 Å to 1.36 Å endorse the additional negative charge on the Tz.[9] The air-stability of **2** was confirmed by a qualitative analysis of the solid-state infrared spectra (IR). Under aerobic conditions, IR spectra of compound **2** were collected over 20 days and no drastic change in the overall absorption peaks were observed (Fig. 4.5).

To further analyse the nature of the pancake bond within complex **2**, broken symmetry density functional theory (BS-DFT)[14] and complete active space self-consistent field (CASSCF) calculations[15] were carried out for two yttrium model systems **3** and **4** (see computational details, section 4.6). The substitution of paramagnetic Dy(III) ions for diamagnetic Y(III) ions enables the investigation of rad-rad interaction between two bpytz$^{\bullet-}$ radicals without the need to consider plausible bpytz$^{\bullet-}$-Dy(III) and Dy(III)-Dy(III) interactions and spin-orbit coupling effects arising from Dy(III) ions.

Although two pairing radicals with each having an unpaired electron can form a triplet or singlet state system depending on the ferromagnetic or antiferromagnetic coupling of their spins, respectively, the ground state of a system showing a pancake bond is typically a singlet.[1] The singlet state is favoured over triplet because the single occupied molecular orbitals (SOMOs) of radical ligands forming the pancake bond strongly overlap with each other: when radical units have identical SOMOs, their overlap automatically favours an antiferromagnetic interaction of spins at shorter rad···rad distances due to the symmetry of SOMOs.[16] The wave function of the singlet state pancake bonded system contains usually a considerable amount of a singlet diradical character.[1] The singlet diradical is a molecular entity in which two electrons occupy two (nearly) degenerate molecular orbitals.[17] The wave function of such a system is a multiconfigurational and cannot be described by the single Slater determinant based methods such as the restricted Hartree-Fock theory but multiconfigurational based approaches like CASSCF are needed to describe it. In strict sense the basic formalism of DFT is also a single determinant approach but it is able to treat small to moderate amount of the singlet diradical character, and, thus it is also an applicable computational method to model the pancake bond within the model complexes **3** and **4**.

To confirm the ground state multiplicity of the yttrium model systems, we first calculated the energies of their singlet and triplet states using the CAM-B3LYP/def2-TZVP level of theory.[18,18] For both yttrium model systems, BS-DFT calculations predict the triplet state to be ~ 2200 cm^{-1} higher in energy than the singlet state confirming that the singlet state is the ground state for **3** and **4** (Tab. 4.4).

Fig. 4.6 shows the highest occupied molecular orbitals (HOMO) and lowest unoccupied molecular orbital (LUMO) obtained at the CAM-B3LYP/def2-TZVP[18,19] level of theory for the singlet state of **3**. As can be seen from Fig. 4.8, the $bpytz^{\bullet-}$ radicals within complex are π-dimerized through an orbital interaction that resembles a covalent type bonding interaction. The spin density distribution is also presented in Fig. 4.6, and it shows a strong localization of spin density on the central rings of two $bpytz^{\bullet-}$ as well as almost equal distribution for α and β spin density. To

quantify the orbital interaction better in **3** and **4**, we calculated the rad-rad coupling constant ($J_{rad\text{-}rad}$) within **3** and **4** using the BS-DFT formalism and the Yamaguchi projection[20] as well as evaluated the singlet diradical character, unpaired electron density,[21] and formal bond order (p_{NO})[22] of **4** utilizing natural orbital occupation numbers (NOONs) from CASSCF calculations (see section 4.6 for details).

By substituting the energies and expectation values of the $\hat{S}^2$ operator of the singlet and triplet state obtained from CAM-B3LYP/def2-TZVP calculations to the Yamaguchi projection, the $J_{rad\text{-}rad}$ values of -3938 cm^{-1} and -3981 cm^{-1} were obtained for **3** and **4**, respectively. The obtained values are in line with values reported for other π-dimerized radical systems and indicate that spins of bpytz$^{\bullet-}$ radicals are strongly antiferromagnetically coupled.[16]

NOONs are the eigenvalues of the one-particle electron density matrix and they converge towards values that they adopt in the exact wave function when enough high level of theory is used.[23] Because of this NOONs at the CASSCF level of theory can be used as a benchmark of the singlet diradical character: In a perfect diradical two natural orbitals are each occupied exactly by one electron. Thus, a suitable index for diradical character is obtained by comparing the occupation number of the acceptor orbital n_{ACC} (formally the LUMO in case of **4**) to the reference value of one electron (n_{ACC} /1.00) × 100%. Despite the size of active space, the investigation of NOONs reveal that ~0.4–0.5 electrons are transferred from the formally HOMO to LUMO which corresponds to 40–50 % of the singlet diradical character. Only a small amount of electron density is distributed from the other formally occupied π-orbitals to unoccupied π-orbitals that all have relatively small NOONs (Tab. 4.5). The results proof that the wave function of **4** contains a notably amount of the singlet diradical character and the formally HOMO and LUMO contribute most to the formation of the pancake bond between π-dimerized bpytz$^{\bullet-}$ radicals. NOONs can be also used to evaluate the p_{NO} and unpaired electron density between bpytz$^{\bullet-}$ radicals. The latter measures the separation of an electron pair into different spatial regions.[21] By using the occupation numbers of the frontier natural orbitals (the formally HOMO and LUMO) of **4** from the CASSCF calculations, the p_{NO} value of 0.5–0.6 is obtained for **4**. The unpaired electron density is measured by calculating

the total number of effectively unpaired electrons (N_u) between bpytz$^{\bullet-}$ ligands. The calculated value of N_u for **4** deviates between 0.79 and 1.25 depending on the size of active space used in the CASSCF calculations but most importantly such high values reflect the notably diradical character of complex **4** (Tab. 4.6).[22,24] Both, the p_{NO} and N_u, values obtained for **4** are in a good agreement with values reported for other systems containing a single pancake bond.

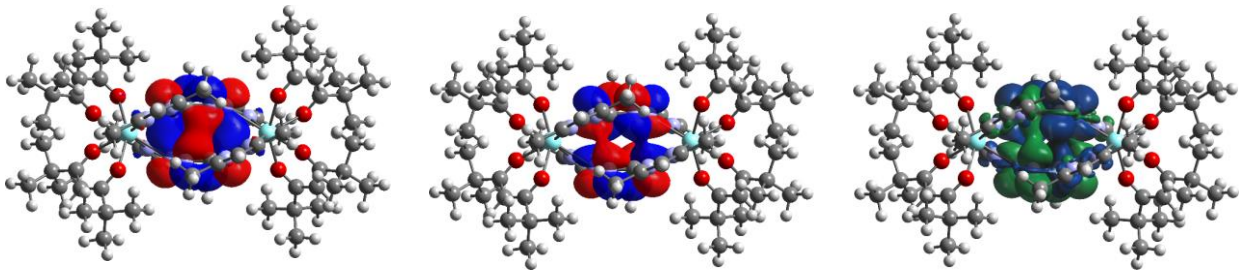

Figure 4.6. Highest occupied molecular orbitals (HOMO) and lowest unoccupied molecular orbitals (LUMO) as well as the spin density distribution (blue = α spin density; green = β spin density) for **3**. **4** has similar HOMO, LUMO and spin density distribution than **3**.

In sum, the BS-DFT and CASSCF calculations indicate that the interaction of between bpytz$^{\bullet-}$ radical ligands resembles more a covalent bond than a weak antiferromagnetic exchange interaction. In this respect, the π-dimerized bpytz$^{\bullet-}$ radicals function as a diamagnetic linker between two Dy(III) ions within complex **2** that very likely prevents a strong exchange coupling between Dy(III) ions and "unpaired" electron of each bpytz$^{\bullet-}$ radical ligands.

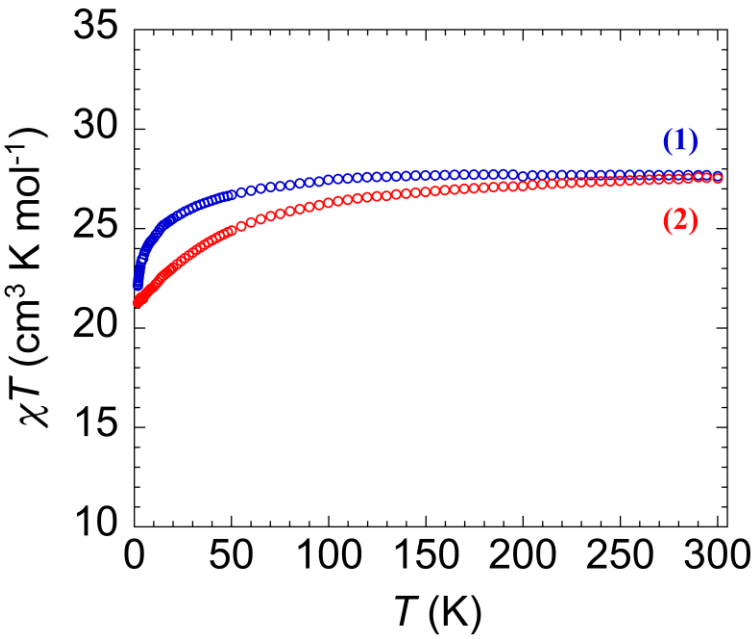

Figure 4.7. Variable-temperature dc magnetic susceptibility data, where $\chi = M/H$ normalized per mole, for **1** (blue) and **2** (red) obtained under applied field of 1000 Oe from 300 to 1.8 K.

Direct current (dc) measurements were performed using a SQUID magnetometer in order to investigate the magnetic susceptibility in **1** and **2**. Overall, the dc susceptibility data obtained at 1000 Oe in the temperature range of 1.8 – 300 K display similar shapes for both complexes (Fig. 4.7). The χT products remain constant at high temperatures with a smooth decrease around 100 K. At room temperature the magnetic susceptibility is 27.64 cm^3 K mol^{-1} for **1** and 27.53 cm^3 K mol^{-1} for **2**. These experimental values are in agreement with the theoretical χT estimated for two non-interacting Dy(III) ions (S = 5/2; $^6H_{15/2}$; L = 5; g = 4/3; χT = 14.17 cm^3 K mol^{-1}). The dc susceptibility at 300 K found for **1** and the similar curve with the radical complex **2** is a significant indication of strong $bpytz^{\bullet-}$–$bpytz^{\bullet-}$ interaction and ineffective Dy–$bpytz^{\bullet-}$ coupling.[9c] The drop observed in the curve to 22.13 cm^3 K mol^{-1} and 20.10 cm^3 K mol^{-1} at 1.8 K for **1** and **2** respectively, is attributed to the thermal depopulation of the excited states.[7a,25c]

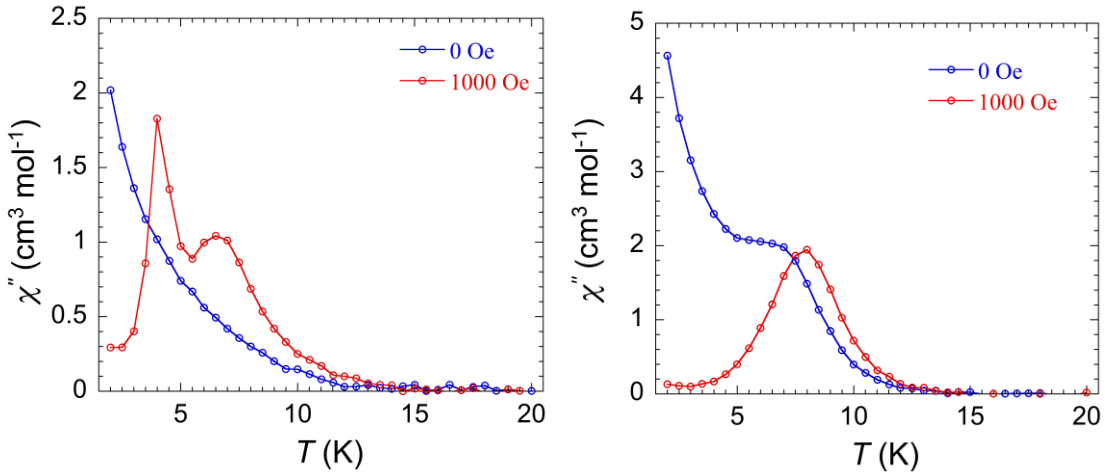

Figure 4.8. ac susceptibility measurement performed at variable temperature under zero and applied dc field of 1000 Oe for **1** (left) and **2** (right).

In addition, the field dependence of the magnetization (*M vs*. *H*/*T*) data collected with fields up to 7 T, as expected, shows no saturation and no superimposition of the isotherms (See section 4.6 Fig. 4.18). Moreover, the shape of the curves displayed in the plots are attributed to the significant magnetic anisotropy resulting from the large spin-orbit coupling contribution of Dy(III) metal ion.[25]

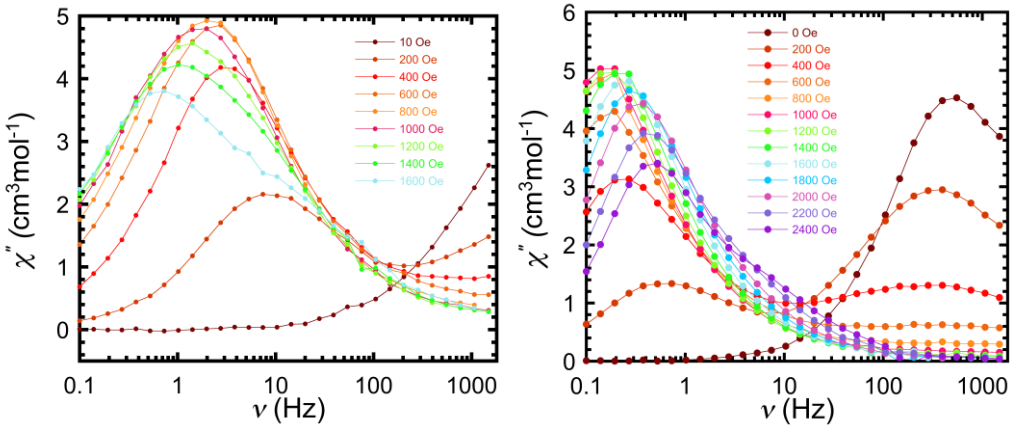

Figure 4.9. ac susceptibility measurements performed at 2 K and magnetic field ranging from 0 to 1800 Oe for **1** (left) and **2** (right).

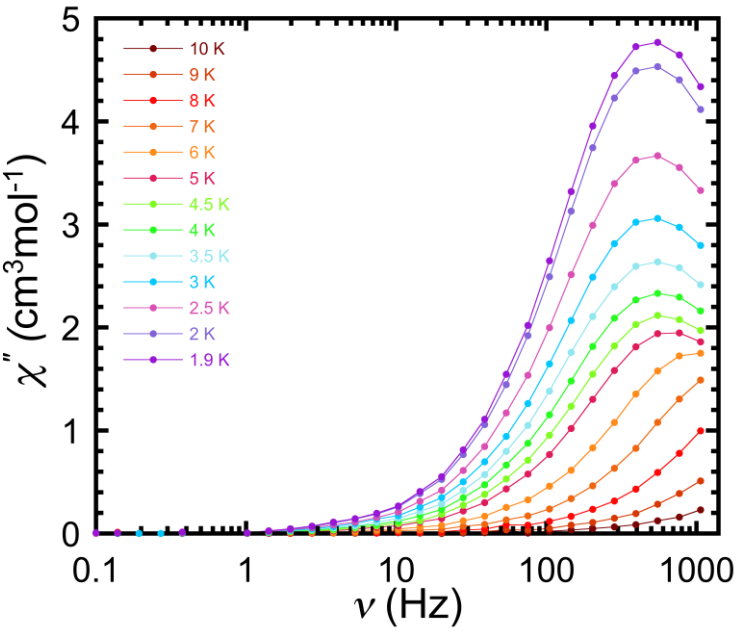

Figure 4.10. Frequency dependence of ac susceptibility (χ") under zero field and variable temperature for **2**.

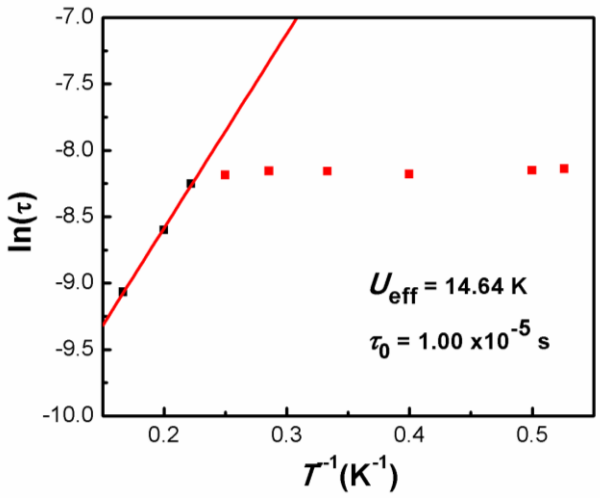

Figure 4.11. Plot of the relaxation time of the magnetization using ac data (χ" *vs*. ν at zero Oe) for **2**. The solid red line indicates the Arrhenius fit.

In order to confirm SMM behaviour we performed ac measurements for both complexes under dc applied fields of 0 and 1000 Oe. At low temperatures (below 12 K) and zero-field, while complex **1** shows only a tail, complex **2** displays a shoulder followed by a tail in the out-of-phase component (χ"). However, for both systems a relaxation process (full peak) is only observed when a strong static field (1000 Oe) is applied (Fig. 4.8). Such behaviour is commonly indicative of the mixing of M_J energy levels in the ground state which can be minimized by applying a small static field (optimum field).[25c] Therefore, the optimal field was assigned through an ac susceptibility measurement carried out under 2 K and a variable static field (up to 2400 Oe) for complexes **1** and **2**. The results plotted in Fig. 4.9 show that under zero-field a peak (tail in the case of **1**) is observed at high frequencies. In fact, no full out-of-phase signal was observed for **1** when ac measurements were performed under zero applied field and variable temperature. The same was not true for **2,** where significant peaks shifting at high frequencies were observed. Upon further analysis of the χ" *vs*. frequency data for **2** (Fig. 4.10) using an Arrhenius fit ($\tau = \tau_0 \, exp \, (U_{eff}/K_B T)$) the parameters obtained suggest the relaxation process does not occur through Orbach mechanism (Fig. 4.11).[25d] However, when higher dc fields (above 200 Oe) are applied, clear peaks are observed at low frequencies for both complexes (Fig. 4.9). In the case of **2**, a second relaxation process is also observed at high frequencies under applied dc fields of 200 and 400 Oe. Nevertheless, as displayed in Fig. 4.11, a clear single ac signal at low frequencies is observed only when the applied dc field is higher than 600 Oe. Hence, in this case a minimal applied dc field is satisfactory in order to give more insight to the magnetic dynamics in these complexes.

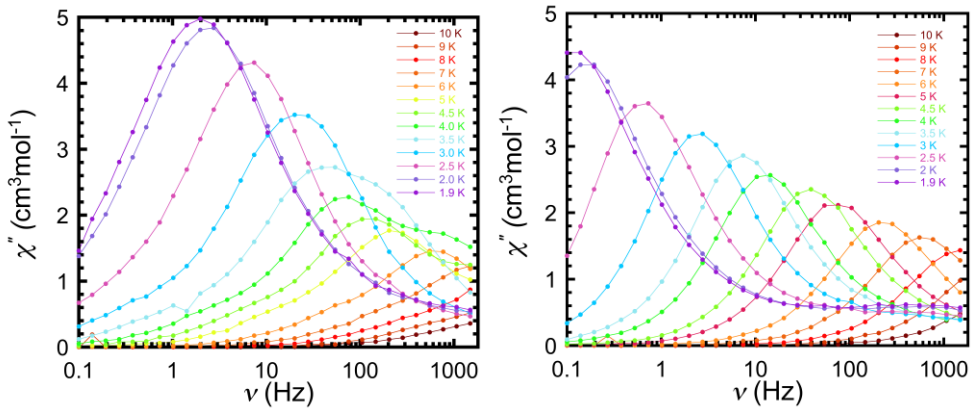

Figure 4.12. Frequency (ν) *vs.* ac susceptibility (χ") measurements performed at 600 Oe and temperature ranging from 1.9 to 10 K for complex **1** (right) and **2** (left).

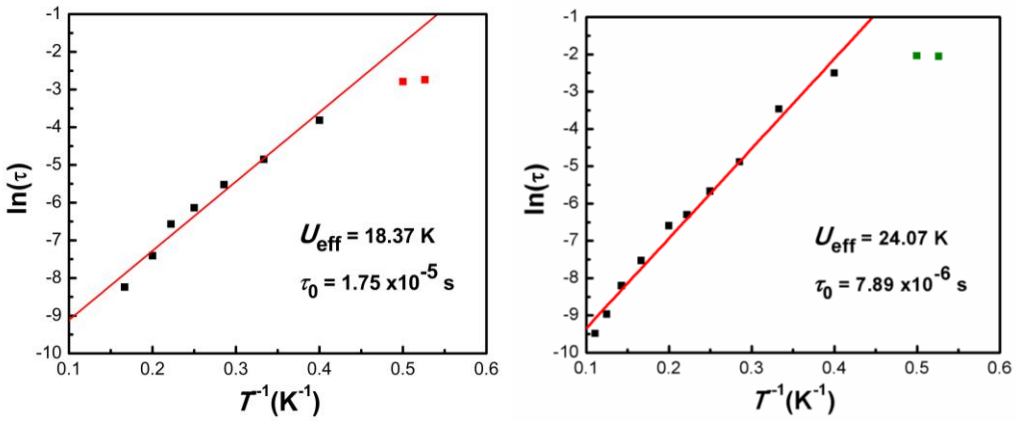

Figure 4.13. Plot of the relaxation time of the magnetization using ac data (χ" *vs.* ν at 600 Oe) for **1** (left) and **2** (right). The solid red line indicates the Arrhenius fit.

Therefore, to validate the nature of SMM behaviour, frequency dependence of the ac susceptibility was measured under an optimum dc field of 600 Oe and variable temperature (1.8 – 10 K) for **1** and **2**. The results in the out-of-phase (χ") plots in Fig. 4.12 show that by increasing the temperature the ac susceptibility decreases toward high frequencies (up to 1000 Hz), which indicates a thermally induced relaxation mode.[26] From these results, the shifting peak maxima is fitted using Arrhenius equation (*vide supra*) where parameters such as the anisotropy barrier (U_{eff}) and the relaxation time (τ_0) can be

estimated. The fitting of the out-of-phase component in Fig. 4.13 using the Arrhenius approach gives U_{eff} = 18.37 (**1**), 24.07 K (**2**) and τ_0 = 1.75 × 10^{-5} (**1**), 7.89 × 10^{-6} s (**2**).

To further obtain information of the relaxation mechanism contributions in both

$$\tau^{-1} = \tau_0^{-1} e^{-U_{eff}/K_B T} + CT^n + \tau_{QTM}^{-1} \qquad (1)$$

complexes, we have used equation (1) to model the data in the τ^{-1} vs. T plot (Fig. 4.14).[27] The best fit was obtained when Orbach ($\tau_0^{-1} e^{-U_{eff}/K_B T}$), Raman ($CT^n$) and QTM ($\tau_{QTM}^{-1}$) terms are applied. Thus, fitting the data gives the following parameters: τ_0 = 4.22 × 10^{-6} s, U_{eff} = 25.38 K, C = 1.31 $K^{-4.12}S^{-1}$, n = 4.12 and QTM = 0.09 s for **1**. Similar values were also obtained for **2**; τ_0 = 1.22 × 10^{-6} s, U_{eff} = 37.20 K, C = 0.67 $K^{-4.49}S^{-1}$, n = 4.49 and QTM = 0.09 s. It is noteworthy that the values found for the Orbach process agrees with those found when the Arrhenius approach is applied, and it is shown to be dominant in both systems at higher temperatures. Attempts to fit the data using terms for a direct process resulted in unrealistic parameter values, the same was observed when a Raman term was applied to fit separately.

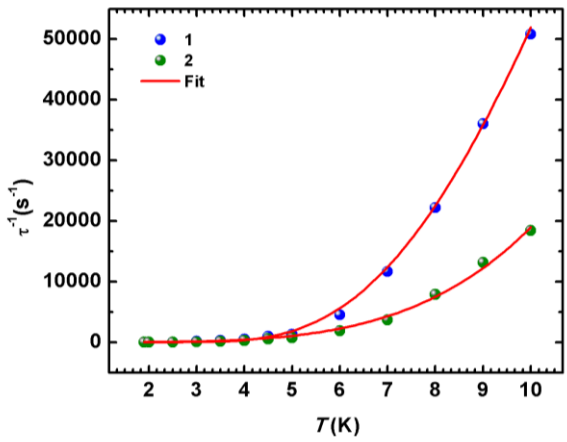

Figure 4.14. Plot of the τ^{-1} *vs*. *T* with the fit (red line) using eq. 1.

In light of above results the magnetic properties of complexes **1** and **2** arise mainly from two non-interacting Dy(III) ions because within complexes **1** and **2** Dy(III) ions are linked via the diamagnetic bridging ligand(s). Thus, we carried out the standard CASSCF/SO-RASSI calculations followed by SINGLE_ANISO[28] and POLY_ANISO[29] routines as implemented in Molcas[30] for **1** and **2** to investigate their magnetic properties in more detail (see section 4.6 for details). The CASSCF/SO-RASSI calculations revealed that the principal magnetic axes of the ground Kramers doublet (KD) are oriented to 91° and 86° angle with respect to the line connecting two Dy(III) ions in **1** and **2**, respectively (Fig. 4.15). In both complexes, the angles between the magnetic axes of the ground doublet and the excited doublets vary significantly from ~16° to 170°, and none of them are parallel to the main magnetic axes of the ground KD doublet (Tab. 4.7 and Tab. 4.8). Both complexes show also non-negligible transverse components in their ***g***-tensor of the ground KD (**1**: g_x = 0.048, g_y = 0.084, g_z = 19.375; **2**: g_x = 0.035, g_y = 0.037, g_z = 18.667) and deviates from the ideal values of highly axial ***g***-tensor ($g_x = g_y = 0.0$, $g_z \approx 20.0$).

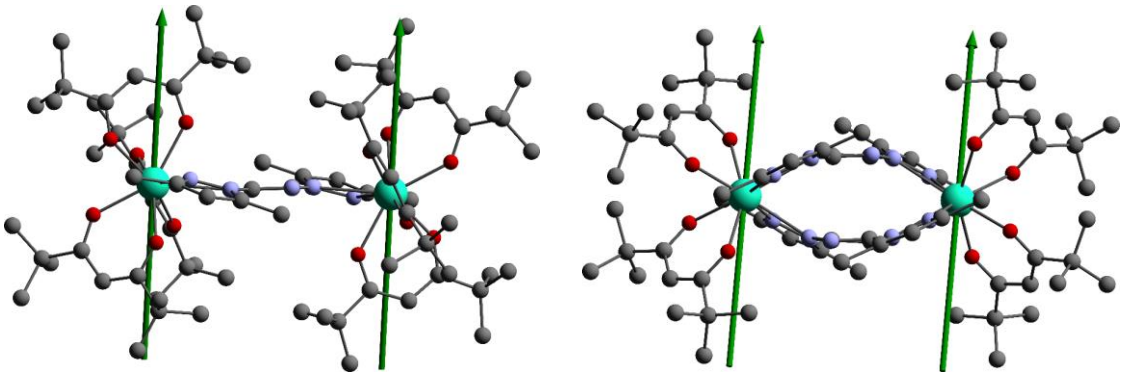

Figure 4.15. Orientations of the main axes of the **g**-tensors in the ground Kramers' doublets of **1** (left) and **2** (right). Hydrogen atoms were omitted for clarity.

The percentage composition of the SO-RASSI wave-functions of the sixteen lowest states are presented in Tab. 4.9 and Tab. 4.10 for **1** and **2**, respectively. As can be seen from Tab. 4.9, the ground doublet within **1** is mainly composed of M_J = ±15/2 states, that is usual for Dy(III) SMMs. The higher lying doublets of **1** are considerably more mixed than the ground doublet and cannot be uniquely defined

by a single M_J state. Surprisingly, the ground doublet of **2** is not pure $M_J = \pm 15/2$ state but contains significant mixing from $M_J = \pm 13/2$ (4 %) and $M_J = \pm 11/2$ states (12 %) as well as smaller contributions from several higher lying states (Tab. 4.10). As expected, also the higher lying doublets are strongly mixed within **2** (Tab. 4.10). Taken into account all above mentioned data, it can be concluded that the low symmetry environment of Dy(III) ions effectively diminishes the axiality of KDs and leads to the strong mixing of states in both complexes.

The diamagnetic nature of bridging bpytz ligands should mediate only weak exchange interaction between Dy(III) ions in both complexes.[31] To test this hypothesis, we fitted calculated $\chi_M T(T)$ and $M(H)$ to the experimental data and modelled the exchange interaction between Dy(III) ions using the Lines model.[32] For both complexes, the calculated plots are presented in Fig. 4.20, and they were obtained by using a small exchange parameters 0.007 cm^{-1} and 0.016 cm^{-1} for **1** and **2**, respectively. Such small values of exchange parameters indicate a very weak exchange interaction between Dy(III) ions in both complexes.[31]

The low axial ***g***-tensors of the ground KDs as well as the weak exchange interaction between Dy(II) ions usually promote the QTM within ground KD.[31] To further study the relaxation of magnetism in both complexes, the qualitive energy barrier for complexes were constructed by plotting the energies of the lowest lying states with respect their magnetic moments and calculating the transition magnetic moment matrix elements between the states, *i.e.*, transition probabilities. The calculated transition probabilities for both complexes show a rather large value for a matrix element connecting the two components of the ground KD: for **1** the value is 0.022, whereas for **2** it is 0.012 (Fig. 4.16). Such high values are usually associated with efficient QTM within the ground KD.[31a] The computational result are fully in line with experimental findings; **1** and **2** show the relaxation of magnetization only when the QTM within KD is suppressed by applied dc field.

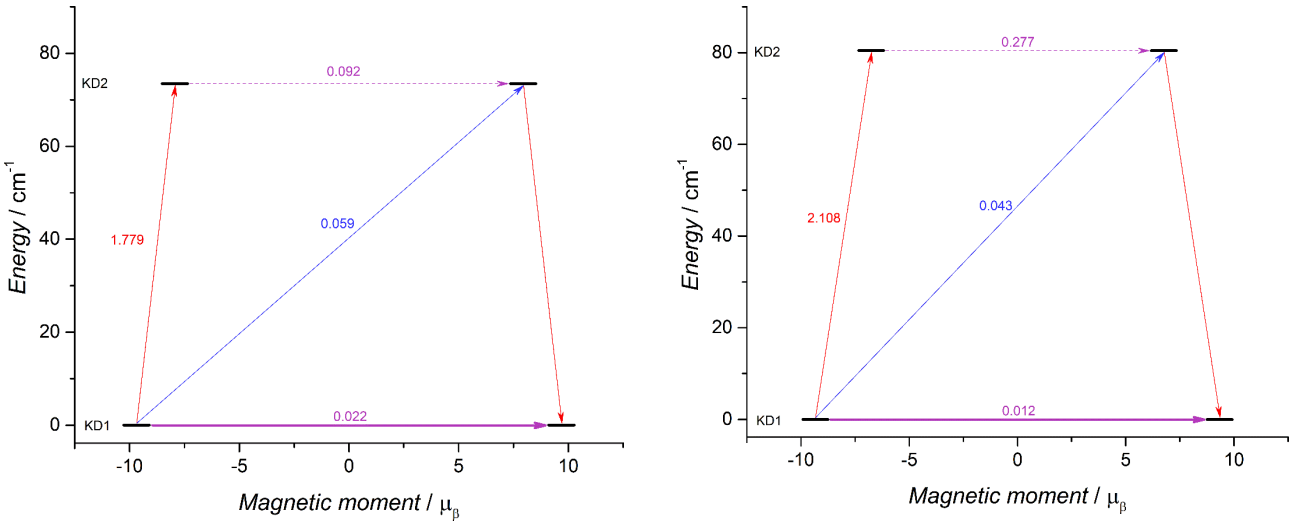

Figure 4.16 Qualitative relaxation barrier for **1** (left) and **2** (right). The numbers show the transition probabilities between KDs. Red, blue, and purple lines show the transition probabilities for the direct vertical transitions, Orbach process, and QTM, respectively. The most plausible relaxation pathways for the studied systems are presented by the solid bold purple arrow.

4.5. Conclusion

In conclusion, we have reported a new complex containing two reduced tetrazine based ligands that form an unusual intramolecular pancake bond. The topology and electronic properties of the bpytz ligand along with TMHD bulky characteristics play a significant role in the assembly and stabilization of the complex. The similarity of χT products observed for **1** and **2**, suggests the two Tz rings are strongly coupled (> -4000 cm^{-1}) which makes the $(bpytz^{\bullet-})_2$ bridge a diamagnetic framework. While no anisotropy barrier was obtained for **1** at zero applied field, complex **2** exhibits a barrier of U_{eff} = 14.64 K. Nevertheless, under an applied field of 600 Oe both complexes exhibit frequency dependence with energy barriers of 25.38 K (**1**) and 37.20 K (**2**). The results found in this ongoing project will be helpful for future strategies on designing new lanthanide-based complexes containing tetrazine-derived radicals in the pursuit to exploit Ln-$Tz^{\bullet-}$ direct exchange coupling.

4.6. Computational details.

The geometries of **1** and **2** were extracted from the crystal structures and the geometry of smaller model system $\mathbf{2_{small}}$ was derived from the geometry of **2** by replacing *tert*-butyl groups of acac ligands with hydrogen atoms (Fig. 4.17). In all studied systems, the positions of hydrogen atoms were optimized at PBE/def2-TZVP level of theory,[35,364] and the core electrons of Y ions were modelled by effective core potential (ECP).[37] The positions of heavier elements were kept frozen during optimization. To avoid convergence problems in optimizations, Dy(III) ions were replaced with Y(III) ions. This operation to

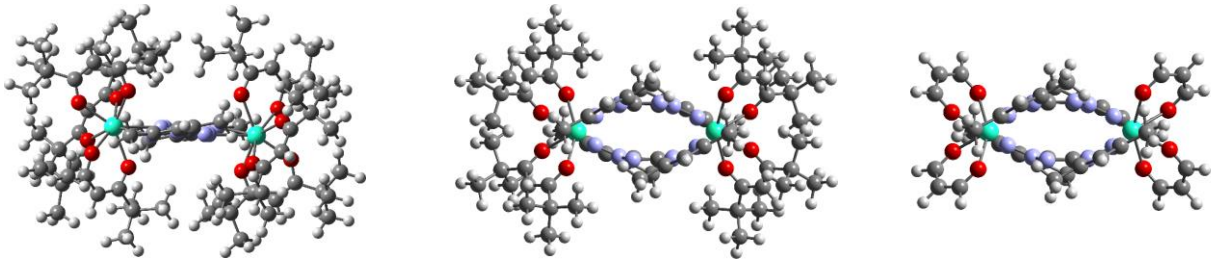

1 **2** $\mathbf{2_{small}}$

Figure 4.17 Geometries of **1**, **2** and $\mathbf{2_{small}}$.

optimize the position of hydrogens is advantageous since the procedure to converge to lowest energy solution is easier for close shell systems (Y(III)) than open shell (Dy(III)).

A singlet diradical character, unpaired electron density, formal bond order (p_{NO}) and radical-radical exchange coupling constant ($J_{rad\text{-}rad}$) in **2**, were evaluated performing the unrestricted broken symmetry DFT (BS-DFT)[38–40,41] calculations for the two yttrium model systems, **3** and **4**, at the CAM-B3LYP/def2-TZVP[42] level of theory as well as carrying out the complete active space self-consistent field CASSCF/def2-TZVP calculations for **4**.[43-45] The geometry of **3** and **4** were extracted from the geometries of **2** and **2small,** respectively, by replacing Dy(III) ions with Y(III) ions. By replacing Dy(III) ions with Y(III) ions the $J_{rad\text{-}rad}$ can be estimated without the need to consider a plausible rad-Dy(III) and Dy(III)-Dy(III) couplings and spin-orbit effects arising from the Dy(III) ions. The $J_{rad\text{-}rad}$ was calculated using the Yamaguchi projection.[47] This approach is a generalized molecular orbital theory developed by Yamaguchi and co-workers applying similar method to calculate the spin-spin interaction using the spin-Hamiltonian approach. Such theory was proposed in order to calculate magnetic interactions between organic molecules. However, the theory described by Yamaguchi employs *ab initio* symmetry-projected unrestricted Hartree-Fock (PUHF) approximation for the calculation of the Hamiltonian in terms of high-spin and low-spin states of the system (Eq. 4.1). (For more theoretical details, please see references 46-48)

$$J_{rad-rad} = E_S - E_T \approx \frac{2(E_{LS}-E_{HS})}{\langle S^2\rangle_{HS}-\langle S^2\rangle_{LS}}, \quad (4.1)$$

In which E_s, E_T, E_{LS} and E_{HS} are the energies of the singlet, triplet, low spin (LS) and high spin (HS) state, respectively, and $\langle S^2\rangle_{HS}$ and $\langle S^2\rangle_{LS}$ are the expectation values of the $\hat{S}^2$ operator evaluated in the Kohn-Sham determinant.[46-48]

The CASSCF/def2-TZVP calculations were carried out for **4** by using eight different active space: CAS(2,2), CAS(4,4), CAS(6,6), CAS(8,8), CAS(10,10), CAS(12,12), CAS(14,14) and CAS(16,16), that is, the size of active space was systematically increased by including more π-orbitals of π-dimerized bpytz$^{\bullet-}$ radicals into the active space. The π-orbital orbitals were chosen into the active space based on their

natural orbital occupation numbers (NOONs) that were obtained at the second-order Møller-Plesset perturbation theory level. NOONs are the eigenvalues of the one-particle electron density matrix and they converge towards values that they adopt in the exact wave function when enough high level of theory is used.[49,50] Because of this NOONs at the CASSCF level of theory can be used as a benchmark of the singlet diradical character: In a perfect diradical two natural orbitals are each occupied exactly by one electron. Thus, a suitable index for the singlet diradical character (SDR) is obtained by comparing the occupation number of the acceptor orbital n_{ACC} to the reference value of one electron:

$$SDR = \frac{n_{acc}}{1} \times 100\%. \quad (4.2)$$

The p_{NO} was computed employing following Eq. 4.3.

$$p_{NO} = \frac{NEBO-NEABO}{2}, \quad (4.3)$$

where NEBO and NEABO are the NOONs of the frontier bonding and antibonding orbitals, respectively.[51] The total number of effectively unpaired electrons (N_u) between monomers was obtained with the following Eq. 4.4.

$$N_U = \sum_{i=1}^{N} n_i^2(2-n_i)^2, \quad (4.4)$$

in which n_i refers to the i-th NOON and N to the number of natural orbitals.[52,53] N_u measures the total number of effectively unpaired electrons between radical ligands and it can be used as a benchmark for the singlet diradical character like the equation 2 at the CASSCF level. All above mentioned calculations were performed with Turbomole,[54] Gaussian[55] and Orca[56] quantum chemistry codes.

To calculate the magnetic properties of complexes **1** and **2**, the multi-reference *ab inito* calculations were performed for them using the standard CASSCF/SO-RASSI methodology as implemented in the Molcas quantum chemistry program package versions 8.2 and 8.0.[57] The spin-orbit states of each Dy(III) ions were calculated separately while other one was replaced with Y(III) ion. Due to the inversion symmetry Dy(III) ions are equivalent, the CASSCF/SO-RASSI calculations were performed only for one Dy(III) ion in both complexes. ANO-RCC-VTZP basis set for Dy(III) ion and ANO-RCC-VDZP basis

set for all other atoms (H, C, N, O, F, Y) were used in the CASSCF/SO-RASSI calculations.[58,59] In case of **1**, the ANO-RCC-VDZP basis set of H was replaced with the ANO-RCC-VDZ basis due to the basis set limit of Molcas. The scalar relativistic effects were treated employing the exact two component (X2C) transformation.[60-62] The Cholesky decomposition was used for two electron integrals with the threshold value of 10^{-8} to speed up the calculations. In the SA-CASSCF calculations all 21 sextet, 224 quartet and 490 doublet states, originating from the active space of 9 electrons and seven 4*f*-orbitals, were solved. From these states, the lowest 21 spin sextets, 128 spin quartets and 130 spin doublets (corresponding to an energy cut-off of 50 000 cm^{-1}) were mixed by spin-orbit coupling using the SO-RASSI method.[63] The local magnetic properties (***g***-tensors, transition magnetic moments, and orientation of magnetic axis) were extracted from the RASSI wave functions using the SINGLE_ANISO routine.[31,64,65] The exchange interaction between Dy(III) ions was modelled using the Lines model as implemented in the POLY_ANISO routine.[66,67] For both complexes, the exchange coupling parameter was obtained by fitting the calculated susceptibility and magnetization data to the experimental data. In the fitting procedure, the exchange parameter was increased in increments of 0.001 cm^{-1}, and 2 spin-orbit eigenstates were included in the exchange interaction.

Table 4.4 Calculated energies for high (E_{HS}) and broken symmetry low (E_{LS}) states of **3** and **4** as well as calculated coupling constants for radical-radical coupling ($J_{rad\text{-}rad}$) at CAM-B3LYP/def2-TZVP level of theory.

	E_{HS} [au]	E_{BS} [au]	$J_{rad\text{-}rad}$ [cm^{-1}][a]
3	-4208.18	-4208.19	-3938
4	-2950.44	-2950.45	-3981

a) obtained by using the equation 1.

Table 4.5 Calculated NOONs at the CASSCF/def2-TZVP level of theory for **4**.

NO	CAS(2,2)	CAS(4,4)	CAS(6,6)	CAS(8,8)	CAS(10,10)	CAS(12,12)	CAS(14,14)	CAS(16,16)
220	-	-	-	-	-	-	-	1.96
221	-	-	-	-	-	-	1.99	1.96
222	-	-	-	-	-	1.99	1.96	1.96
223	-	-	-	-	1.96	1.96	1.96	1.96
224	-	-	-	1.99	1.96	1.96	1.96	1.96
225	-	-	1.98	1.96	1.96	1.96	1.96	1.93
226	-	1.96	1.97	1.96	1.96	1.96	1.96	1.92
227	1.57	1.61	1.62	1.61	1.57	1.60	1.63	1.51
228	0.43	0.41	0.39	0.40	0.43	0.40	0.38	0.50
229	-	0.03	0.02	0.03	0.04	0.04	0.04	0.08
230	-	-	0.01	0.03	0.04	0.04	0.04	0.07
231	-	-	-	0.03	0.04	0.04	0.04	0.05
232	-	-	-	-	0.04	0.04	0.04	0.04
233	-	-	-	-	-	0.00	0.02	0.04
234	-	-	-	-	-	-	0.01	0.04
235	-	-	-	-	-	-	-	0.03

Table 4.6 Calculated p_{NO} and N_u for **4**. The values for p_{NO} and N_u for are obtained by using equations 3 and 4, respectively and NOONs from CASSCF/def2-TZVP calculations.

	CAS(2,2)	CAS(4,4)	CAS(6,6)	CAS(8,8)	CAS(10,10)	CAS(12,12)	CAS(14,14)	CAS(16,16)
p_{NO}	0.57	0.60	0.61	0.60	0.57	0.60	0.62	0.51
N_u	0.90	0.83	0.79	0.83	0.96	0.87	0.82	1.25

Table 4.7 Calculated energies and ***g***-tensors for the eight lowest KDs in **1** as well as the angle (θ) between the principal magnetic axes of ground KD and each excited KD.

KD	E / cm^{-1}	g_x	g_y	g_z	θ
1	0.000	0.048	0.084	19.376	-
2	73.744	0.203	0.289	16.965	20.595
3	174.177	1.371	1.558	13.844	171.351
4	240.734	3.245	5.167	9.488	166.670
5	323.009	2.836	5.136	10.549	90.538
6	430.867	0.885	1.891	16.138	77.806
7	549.580	0.318	0.732	16.219	96.655
8	653.053	0.112	0.319	18.324	86.709

Table 4.8 Calculated energies and ***g***-tensors for the eight lowest KDs in **2** as well as the angle (θ) between the principal magnetic axes of ground KD and each excited KD.

KD	E / cm^{-1}	g_x	g_y	g_z	θ
1	0.000	0.035	0.037	18.667	-
2	80.468	0.326	1.083	14.099	16.504
3	126.562	2.834	4.529	12.407	100.448
4	171.838	2.553	3.076	8.264	65.464
5	249.809	0.184	0.229	12.036	70.011
6	367.991	0.204	0.266	14.208	74.897
7	451.513	0.242	0.258	17.471	115.515
8	522.905	0.038	0.054	19.150	75.185

Table 4.9 Percentage composition of the SO-RASSI wave functions for each M_J state of the ground multiplet (J = 15/2) in **1**.

M_J	KD1		KD2		KD3		KD4		KD5		KD6		KD7		KD8	
-15/2	0.0	91.1	1.5	0.0	6.0	0.0	0.0	0.6	0.0	0.4	0.2	0.0	0.1	0.0	0.0	0.0
-13/2	0.0	0.1	69.1	0.1	20.4	0.2	2.1	2.6	2.7	1.0	0.0	1.0	0.6	0.2	0.1	0.0
-11/2	0.0	8.4	12.7	0.0	49.6	0.1	0.4	14.3	0.4	7.0	4.2	0.4	1.6	0.2	0.6	0.1
-9/2	0.0	0.1	14.8	0.0	2.6	0.4	13.0	38.8	15.5	0.1	4.0	4.6	2.7	1.7	0.9	0.8
-7/2	0.0	0.2	0.7	0.0	14.7	0.0	0.4	3.5	12.0	36.2	7.4	12.3	7.3	2.1	1.1	2.0
-5/2	0.0	0.1	0.4	0.0	3.0	0.2	2.4	9.4	5.7	0.7	40.1	4.5	20.1	6.2	1.3	5.9
-3/2	0.0	0.1	0.3	0.0	1.2	0.3	1.7	7.0	2.9	3.1	1.1	10.9	15.8	29.4	3.2	23.0
-1/2	0.0	0.0	0.3	0.0	0.5	0.7	1.2	2.7	0.8	11.3	5.8	3.6	9.5	2.6	36.8	24.2
1/2	0.0	0.0	0.0	0.3	0.7	0.5	2.7	1.2	11.3	0.8	3.6	5.8	2.6	9.5	24.2	36.8
3/2	0.1	0.0	0.0	0.3	0.3	1.2	7.0	1.7	3.1	2.9	10.9	1.1	29.4	15.8	23.0	3.2
5/2	0.1	0.0	0.0	0.4	0.2	3.0	9.4	2.4	0.7	5.7	4.5	40.1	6.2	20.1	5.9	1.3
7/2	0.2	0.0	0.0	0.7	0.0	14.7	3.5	0.4	36.2	12.0	12.3	7.4	2.1	7.3	2.0	1.1
9/2	0.1	0.0	0.0	14.8	0.4	2.6	38.8	13.0	0.1	15.5	4.6	4.0	1.7	2.7	0.8	0.9
11/2	8.4	0.0	0.0	12.7	0.1	49.6	14.3	0.4	7.0	0.4	0.4	4.2	0.2	1.6	0.1	0.6
13/2	0.1	0.0	0.1	69.1	0.2	20.4	2.6	2.1	1.0	2.7	1.0	0.0	0.2	0.6	0.0	0.1
-15/2	91.1	0.0	0.0	1.5	0.0	6.0	0.6	0.0	0.4	0.0	0.0	0.2	0.0	0.1	0.0	0.0

Table 4.10 Percentage composition of the SO-RASSI wave functions for each M_J state of the ground multiplet (J = 15/2) in **2**.

M_J	KD1		KD2		KD3		KD4		KD5		KD6		KD7		KD8	
-15/2	0.0	79.8	0.0	0.6	3.9	0.1	0.1	5.4	0.3	2.6	2.1	0.2	0.0	4.6	0.0	0.3
-13/2	0.0	4.1	1.3	52.1	0.5	5.1	9.2	0.3	6.6	2.6	4.2	1.7	0.4	11.2	0.4	0.2
-11/2	0.0	11.8	0.0	0.9	3.7	1.6	6.4	13.8	15.5	9.4	5.3	12.5	1.9	16.1	0.7	0.6
-9/2	0.0	1.7	0.6	22.3	0.6	1.3	0.1	0.0	11.6	1.7	10.3	19.5	4.3	19.0	2.9	4.2
-7/2	0.0	1.0	0.2	11.7	5.3	1.7	7.6	13.4	2.4	0.8	2.5	11.1	10.0	10.3	19.4	2.6
-5/2	0.0	1.2	0.1	0.4	24.0	4.3	0.6	9.5	14.6	3.1	0.2	0.8	2.6	8.5	17.6	12.4
-3/2	0.0	0.3	0.8	6.2	6.6	7.6	24.6	3.3	0.9	8.3	2.1	10.1	0.3	5.9	20.8	2.2
-1/2	0.1	0.0	0.3	2.4	17.7	16.2	1.9	3.8	3.6	16.0	8.2	9.3	1.7	3.3	4.1	11.4
1/2	0.0	0.1	2.4	0.3	16.2	17.7	3.8	1.9	16.0	3.6	9.3	8.2	3.3	1.7	11.4	4.1
3/2	0.3	0.0	6.2	0.8	7.6	6.6	3.3	24.6	8.3	0.9	10.1	2.1	5.9	0.3	2.2	20.8
5/2	1.2	0.0	0.4	0.1	4.3	24.0	9.5	0.6	3.1	14.6	0.8	0.2	8.5	2.6	12.4	17.6
7/2	1.0	0.0	11.7	0.2	1.7	5.3	13.4	7.6	0.8	2.4	11.1	2.5	10.3	10.0	2.6	19.4
9/2	1.7	0.0	22.3	0.6	1.3	0.6	0.0	0.1	1.7	11.6	19.5	10.3	19.0	4.3	4.2	2.9
11/2	11.8	0.0	0.9	0.0	1.6	3.7	13.8	6.4	9.4	15.5	12.5	5.3	16.1	1.9	0.6	0.7
13/2	4.1	0.0	52.1	1.3	5.1	0.5	0.3	9.2	2.6	6.6	1.7	4.2	11.2	0.4	0.2	0.4
-15/2	79.8	0.0	0.6	0.0	0.1	3.9	5.4	0.1	2.6	0.3	0.2	2.1	4.6	0.0	0.3	0.0

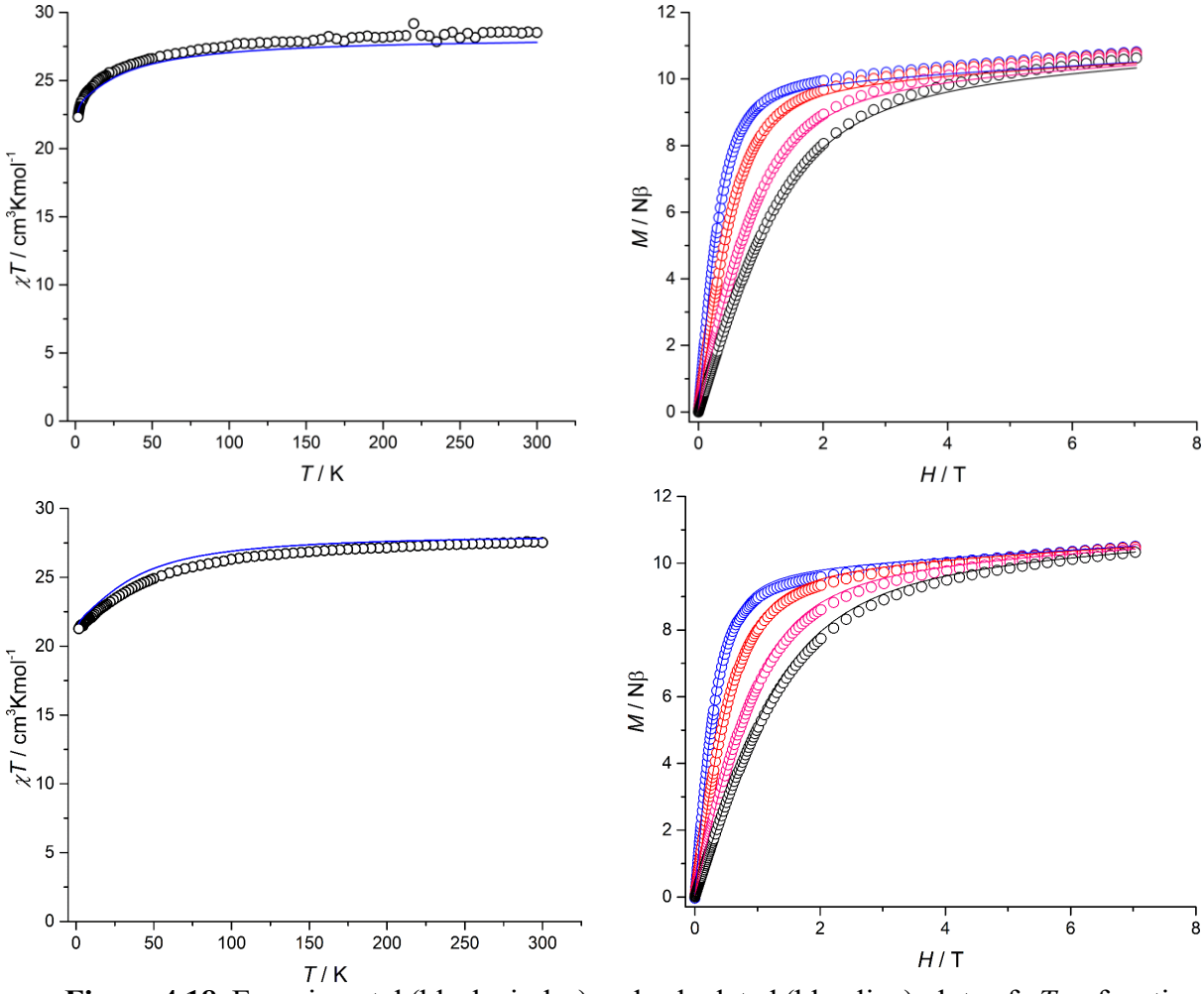

Figure 4.18. Experimental (black circles) and calculated (blue line) plots of χT as function of temperature for **1** (up, left) and **2** (down, left). The plots of M as a function of magnetic field at 1.8 K (blue), 3 K (red), 5 K (pink) and 7 K (black) for **1** (up, right; circles = experimental values, lines = calculated data, lines + circles = scaled data) and **2** (down, right; circles = experimental values, lines = calculated data). Calculated plots were obtained by including 2 spin-orbit eigenstates in the exchange interaction and using the Lines parameter 0.005 cm^{-1} and 0.016 cm^{-1} for **1** and **2**, respectively.

References

1 M. Kertesz, *Chem. Eur. J*., 2018, doi.org/10.1002/chem.201802385 (b) Z.-H. Cui, H. Lischka, H. Z. Beneberu and M. kertesz*, J. Am. Chem. Soc.* 2014, **136**, 12958.

2 K. V. Raman, A. M. kamerbeek, A. Mukherjee, N. Atodiresei, T. K. Sen, P. Lazić, V. Caciuc, R. Michel, D. Stalke, S. K. Mandal, S. Blugel, M. Münzenberg and J. S. Moodera, *Nature*, 2013, **493**, 509. (b) Y. Morita, S. Suzuki, K. Sato and T. Takui, *Nature*, 2011, **3**, 197.

3 Y. Horii, S. Kishiue, M. Damjanović, K. Katoh, B. K. Breedlove, M. Enders and M. Yamashita, *Chem. Eur. J*., 2018, **24**, 4320. (b) K. Zhang, V. Montigaud, O. Cador, G.-P. Li, B. le Guennic, J.-K. Tang and Y.-Y. Wang, *Inorg. Chem*., 2018, **57**, 8550. (c) K. L. M. Harriman, I. Korobkov and M. Murugesu, *Organometallics*, 2017, **36**, 4515. (d) J.-Y. Ge, L. Cui, J. Li, F. Yu, Y. Song, Y.-Q. Zhang, J.-L. Zuo and M. Kurmoo, *Inorg*. *Chem*., 2017, **56**, 336.

4 F.-S. Guo, B. M. Day, Y.-C. Chen, M-L. Tong, A. Mansikkamäki and R. A. Layfield, *Angew. Chem. Int. Ed*., 2017, **56**, 11445. (b) S. K. Langley, D. P. Wielechowiski, V. Vieru, N. F. Chilton, B. Moubaraki, B. F. Abrahams, L. F. Chiboratu and K. S. Murray, *Angew. Chem. Int. Ed.,* 2013, **52**, 12014. (c) C.-M. Liu, D.-Q. Zhang and D.-B. Zhu, *Sci. Rep*., 2017, **7**, 1. (d) R. Mitsuhashi, K. S. Pedersen, T. Ueda, T. Suzuki, J. Bendix and M. Mikuriya, *Chem. Commun*., 2018, DOI: 10.1039/C8CC04756A. (e) J. J. Le Roy, L. Ungur, I. Korobkov, L. F. Chiboratu and M. Murugesu, *J. Am. Chem. Soc*., 2014, **136**, 8003. (f) J.-L. Liu, Y.-C. Chen and M.-L. Tong, *Chem. Soc*. *Rev*., **47**, 2431.

5 F. Habib, G. Brunet, V. Vieru, I. Korobkov, L. F. Chiboratu and M. Murugesu, *J. Am. Chem. Soc*., 2013, **135**, 13242. (b) Y. Peng, V. Mereacre, A. Baniodeh, Y. Lan, M. Schlageter, G. E. Kostakis and A. K. Powell, *Inorg. Chem*., 2015, **55**, 68. (c) G. Huang, X. Yi, J. Jung, O. Guillou, O. Cador, F. Pointillart, B. L. Guennic and K. Bernot, *Eur. J. Inorg. Chem.*, 2018, 326. (d) A. Rasamsetty, C. Das, E. C. Sañudo, M. Shanmugam and V. Baskar, *Dalton Trans*., 2018, **47**, 1726.

6 S. Fortier, J. J. Le Roy, C.-H. Chen, V. Vieru, M. Murugesu, L. F. Chiboratu, D. J. Mindiola and K. G. Caulton, *J. Am. Chem. Soc.*, 2013, **135**, 14670.

7 (a) J. D. Rinehart, M. Fang, W. J. Evans and J. R. Long, *J. Am. Chem. Soc.*, 2011, **133**, 14236. (b) S. Demir, I.-R. Jeon, J. R. Long and T. D. Harris, *Coord. Chem. Rev.*, 2015, **289**, 149. (c) D. Gatteschi and R. Sessoli, *Angew. Chem. Int. Ed.,* 2003, **42**, 268. (d) F. Liu, D. S. Krylov, L. Spree, S. M. Avdoshenko, N. A. Samoyolova, M. Rosenkranz, A. Kostanyan, T. Greber, A. U. B. Wolter, B. Büchner and A. A. Popov, *Nat. Commun.,* 2017, **8**, 1.

8 W. Kaim, *Coord. Chem. Rev.*, 2002, **230**, 127.

9 T. J. Woods, M. F. Ballesteros-Rivas, S. M. Ostrovsky, A. V. Palii, O. S. Reu, S. I. Klokishner and K. R. Dunbar, *Chem. Eur. J.*, 2015, **21**, 10302. (b) M. A. Lemes, G. Brunet, A. Pialat, L. Ungur, I. Korobkov and M. Murugesu, *Chem. Commun*, 2017, **53**, 8660. (c) D. I. Alexandropoulos, B. S. Dolinar, K. R. Vignesh and K. R. Dunbar, *J. Am. Chem. Soc*. 2017, **139**, 11040. (d) T. J. Woods, H. D. Stout, B. S. Dolinar, K. R. Vignesh, M. F. Ballesteros-Rivas, C. Achim and K. Dunbar, *Inorg. Chem*. 2017, **56**, 12094. (e) M. Schwach, H. D. Hausen and W. Kaim, *Inorg. Chem.*, 1999, **38**, 2242. (f) M. Glockle, K. Hubler, H. J. Kummerer, G. Denninger and W. Kaim, *Inorg. Chem.*, 2001, **40**, 2263. (g) K. Parimal, S. Vyas, C. H. Chen, C. M. Hadad and A. H. Flood, *Inorg. Chim. Acta*, 2011, **374**, 620. (h) S. K. Tripathy, M. van der Meer, A. Sahoo, P. Laha, N. Dehury, S. Plebst, B. Sarkar, K. Samanta and S. Patra, *Dalton Trans.*, 2016, **45**, 12532. (i) M. A. Lemes, H. N. Stein, B. Gabidullin, K. Robeyns, R. Clérac and M. Murugesu, *Chem. Eur. J.,* 2018, **24**, 4259.

10 D. N. Woodruff, R. E. P. Winpenny and R. A. Layfield, *Chem. Rev.*, 2013, **113**, 5110. (b) J. M. Frost, K. L. M. Harriman and M. Murugesu, *Chem. Sci.*, 2016, **7**, 2470.

11 Sheldrick, G. M. *Acta Crystallographica Section A*, **2008**, 64, 112-122.

12 D. Casanova, M. Llunell, P. Alemany, S. Alvarez, *Chem. Eur. J.*, **2005**, 11, 1479 – 1494.

13 C. N. Carlson, C. J. Kuehl, R. E. Da Re, J. M. Veauthier, E. J. Schelter, A. E. Milligan, B. L. Scott, E. D. Bauer, J. D. Thompson, D. E. Morris and K. D.

John, *J. Am. Chem. Soc*., 2006, **128**, 7230. (b) K. E. Preuss, *Polyhedron*, 2014, **79**, 1. (c) G. Brunet, E. Sebastiao, T. G. Witkowski, I. Korobkov, B. Gabidullin and M. Murugesu, *Dalton Trans*., 2018, DOI: 10.1039/C8DT00146D.

14 (a) L. Noodleman, *J. Chem. Phys.*, 1981, **74**, 5737–5743. (b) L. Noodleman and E. R. Davidson, *Chem. Phys.*, 1986, **109**, 131–143. (c) L. Noodleman, J. G. Norman, J. H. Osborne, A. Aizman and D. A. Case, *J. Am. Chem. Soc.*, 1985, **107**, 3418–3426. (d) W. Koch and M. C. Holthausen, *A Chemist's Guide to Density Functional Theory*, Wiley-VCH Verlag GmbH, Weinheim, FRG, 2001.

15 (a) P. Siegbahn, A. Heiberg, B. Roos and B. Levy, *Phys. Scr.*, 1980, **21**, 323–327. (b) B. O. Roos, P. R. Taylor and P. E. M. Si≐gbahn, *Chem. Phys.*, 1980, **48**, 157–173. (7) B. O. Roos, R. Lindh, P. Å. Malmqvist, V. Veryazov and P.-O. Widmark, *Multiconfigurational Quantum Chemistry*, John Wiley & Sons, Inc., Hoboken, NJ, USA, 2016.

16 A. Mansikkamäki and H. M. Tuononen, *J. Phys. Chem. Lett.*, 2018, **9**, 3624–3630.

17 (a) J. Gräfenstein, E. Kraka, M. Filatov and D. Cremer, *Int. J. Mol. Sci.*, 2002, **3**, 360–394. (b) T. Bally and W. T. Borden, 2007, pp. 1–97.

18 T. Yanai, D. P. Tew and N. C. Handy, *Chem. Phys. Lett.*, 2004, **393**, 51–57.

19 (a)F. Weigend and R. Ahlrichs, *Phys. Chem. Chem. Phys.*, 2005, **7**, 3297–3305. (b) D. Andrae, U. Häußermann, M. Dolg, H. Stoll and H. Preuß, *Theor. Chim. Acta*, 1990, **77**, 123–141.

20 (a) K. Yamaguchi, T. Tsunekawa, Y. Toyoda and T. Fueno, *Chem. Phys. Lett.*, 1988, **143**, 371–376. (b) K. Yamaguchi, H. Fukui and T. Fueno, *Chem. Lett.*, 1986, **15**, 625–628. (c) K. Yamaguchi, F. Jensen, A. Dorigo and K. N. Houk, *Chem. Phys. Lett.*, 1988, **149**, 537–542.

21 (a) M. Head-Gordon, *Chem. Phys. Lett.*, 2003, **372**, 508–511. (b) M. Head-Gordon, *Chem. Phys. Lett.*, 2003, **380**, 488–489.

22 Z. Cui, H. Lischka, H. Z. Beneberu and M. Kertesz, *J. Am. Chem. Soc.*, 2014, **136**, 12958–12965.

23 M. S. Gordon, M. W. Schmidt, G. M. Chaban, K. R. Glaesemann, W. J. Stevens and C. Gonzalez, *J. Chem. Phys.*, 1999, **110**, 4199–4207.

24 (a) H. Z. Beneberu, Y.-H. Tian and M. Kertesz, *Phys. Chem. Chem. Phys.*, 2012, **14**, 10713. (b) Z. Cui, H. Lischka, T. Mueller, F. Plasser and M. Kertesz, *ChemPhysChem*, 2014, **15**, 165–176.

25 R. Sessoli, A. K. Powell, *Coord. Chem. Rev*., 2009, **253**, 2328. (b) L. Ungur, L. F. Chiboratu, *Inorg. Chem.,* 2016, **55**, 10043. (c) F. Habib and M. Murugesu, *Chem. Soc. Rev*., 2013, 42, 3278. (d) T. Lacelle, G. Brunet, R. J. Holmberg, B. Gabidulin and M. Murugesu, *Cryst. Growth Des*. 2017, **17**, 5044.

26 E. M. Fatila, M. Rouzières, M. C. Jennings, A. J. Lough, R. Clérac and K. E. Preuss, *J. Am. Chem. Soc*., 2013, **135**, 9596. (b) P.-H. Lin, W.-B. Sun, M.-F. Yu, G.-M. Li, P.-F. Yan and M. Murugesu, *Chem. Commun*., 2011, **47**, 10993.

27 E. Colacio, J. Ruiz, E. Ruiz, E. Cremades, J. Krzystek, S. Carretta, J. Cano, T. Guidi, W. Wernsdorfer and E. K. Brechin, *Angew. Chem. Int. Ed*., 2013, **52**, 9130. (b) T. Pugh, N. F. Chilton and R. A. Layfield, *Angew. Chem. Int. Ed.,* 2016, **55**, 11082. (c) J. D. Hilgar, M. G. Bernbeck, B. S. Flores and J. Rinehart, *Chem. Sci*., 2018, DOI: 10.1039/C8SC01361F.

28 (a) L. F. Chibotaru and L. Ungur, *J. Chem. Phys.*, 2012, **137**, 064112. (b) L. Ungur and L. F. Chibotaru, *Chem. - A Eur. J.*, 2017, **23**, 3708–3718. (c) L. Ungur, M. Thewissen, J.-P. Costes, W. Wernsdorfer and L. F. Chibotaru, *Inorg. Chem.*, 2013, **52**, 6328–6337.

29 (a) L. F. Chibotaru, L. Ungur and A. Soncini, *Angew. Chemie Int. Ed.*, 2008, **47**, 4126–4129. (b) L. Ungur, W. Van den Heuvel and L. F. Chibotaru, *New J. Chem.*, 2009, **33**, 1224.

30 F. Aquilante, J. Autschbach, R. K. Carlson, L. F. Chibotaru, M. G. Delcey, L. De Vico, I. Fdez. Galván, N. Ferré, L. M. Frutos, L. Gagliardi, M. Garavelli, A. Giussani, C. E. Hoyer, G. Li Manni, H. Lischka, D. Ma, P. Å. Malmqvist, T. Müller, A. Nenov, M. Olivucci, T. B. Pedersen, D. Peng, F. Plasser, B. Pritchard, M. Reiher, I. Rivalta, I. Schapiro, J. Segarra-Martí, M. Stenrup, D. G. Truhlar, L. Ungur, A. Valentini, S. Vancoillie, V. Veryazov, V. P.

Vysotskiy, O. Weingart, F. Zapata and R. Lindh, *J. Comput. Chem.*, 2016, **37**, 506–541.

31 (a) B. S. Dolinar, D. I. Alexandropoulos, K. R. Vignesh, T. James and K. R. Dunbar, *J. Am. Chem. Soc.*, 2018, **140**, 908–911. (b) J. O. Moilanen, A. Mansikkamäki, M. Lahtinen, F.-S. Guo, E. Kalenius, R. A. Layfield and L. F. Chibotaru, *Dalt. Trans.*, 2017, **46**, 13582–13589.

32 M. E. Lines, *J. Chem. Phys.*, 1971, **55**, 2977–2984.

33 J. J. Perdew, K. Burke and M. Ernzerhof, *Phys. Rev. Lett.*, 1996, **77**, 3865–3868.

34 J. P. Perdew and Y. Wang, *Phys. Rev. B*, 1992, **45**, 13244–13249.

35 F. Weigend, *J. Comput. Chem.*, 2008, **29**, 167–175.

36 F. Weigend and R. Ahlrichs, *Phys. Chem. Chem. Phys.*, 2005, **7**, 3297–3305.

37 D. Andrae, U. Häußermann, M. Dolg, H. Stoll and H. Preuß, *Theor. Chim. Acta*, 1990, **77**, 123–141.

38 L. Noodleman and E. R. Davidson, *Chem. Phys.*, 1986, **109**, 131–143.

39 L. Noodleman, J. G. Norman, J. H. Osborne, A. Aizman and D. A. Case, *J. Am. Chem. Soc.*, 1985, **107**, 3418–3426.

40 L. Noodleman, *J. Chem. Phys.*, 1981, **74**, 5737–5743.

41 W. Koch and M. C. Holthausen, *A Chemist's Guide to Density Functional Theory*, Wiley-VCH Verlag GmbH, Weinheim, FRG, 2001.

42 T. Yanai, D. P. Tew and N. C. Handy, *Chem. Phys. Lett.*, 2004, **393**, 51–57.

43 P. Siegbahn, A. Heiberg, B. Roos and B. Levy, *Phys. Scr.*, 1980, **21**, 323–327.

44 B. O. Roos, P. R. Taylor and P. E. M. Sibahn, *Chem. Phys.*, 1980, **48**, 157–173.

45 B. O. Roos, R. Lindh, P. Å. Malmqvist, V. Veryazov and P.-O. Widmark, *Multiconfigurational Quantum Chemistry*, John Wiley & Sons, Inc., Hoboken, NJ, USA, 2016.

46 K. Yamaguchi, T. Tsunekawa, Y. Toyoda and T. Fueno, *Chem. Phys. Lett.*, 1988, **143**, 371–376.

47 K. Yamaguchi, H. Fukui and T. Fueno, *Chem. Lett.*, 1986, **15**, 625–628.

48 K. Yamaguchi, F. Jensen, A. Dorigo and K. N. Houk, *Chem. Phys. Lett.*, 1988, **149**, 537–542.

49 D. Doehnert and J. Koutecky, *J. Am. Chem. Soc.*, 1980, **102**, 1789–1796.

50 M. S. Gordon, M. W. Schmidt, G. M. Chaban, K. R. Glaesemann, W. J. Stevens and C. Gonzalez, *J. Chem. Phys.*, 1999, **110**, 4199–4207.

51 Z. Cui, H. Lischka, H. Z. Beneberu and M. Kertesz, *J. Am. Chem. Soc.*, 2014, **136**, 12958–12965.

52 M. Head-Gordon, *Chem. Phys. Lett.*, 2003, **372**, 508–511.

53 M. Head-Gordon, *Chem. Phys. Lett.*, 2003, **380**, 488–489.

54 TURBOMOLE V7.3 2018, a development of University of Karlsruhe and Forschungszentrum Karlsruhe GmbH, 1989-2007, TURBOMOLE GmbH, since 2007; available from http://www.turbomole.com.

55 Gaussian 09, Revision D.01, M. J. Frisch, G. W. Trucks, H. B. Schlegel, G. E. Scuseria, M. A. Robb, J. R. Cheeseman, G. Scalmani, V. Barone, B. Mennucci, G. A. Petersson, H. Nakatsuji, M. Caricato, X. Li, H. P. Hratchian, A. F. Izmaylov, J. Bloino, G. Zheng, J. L. Sonnenberg, M. Hada, M. Ehara, K. Toyota, R. Fukuda, J. Hasegawa, M. Ishida, T. Nakajima, Y. Honda, O. Kitao, H. Nakai, T. Vreven, J. Montgomery, J. A., J. E. Peralta, F. Ogliaro, M. Bearpark, J. J. Heyd, E. Brothers, K. N. Kudin, V. N. Staroverov, R. Kobayashi, J. Normand, K. Raghavachari, A. Rendell, J. C. Burant, S. S. Iyengar, J. Tomasi, M. Cossi, N. Rega, J. M. Millam, M. Klene, J. E. Knox, J. B. Cross, V. Bakken, C. Adamo, J. Jaramillo, R. Gomperts, R. E. Stratmann, O. Yazyev, A. J. Austin, R. Cammi, C. Pomelli, J. W. Ochterski, R. L. Martin, K. Morokuma, V. G. Zakrzewski, G. A. Voth, P. Salvador, J. J. Dannenberg, S. Dapprich, A. D. Daniels, Ö. Farkas, J. B. Foresman, J. V. Ortiz, J. Cioslowski and D. J. Fox, Gaussian, Inc., Wallingford CT, 2016.

56 F. Neese, Wiley Interdiscip. *Rev. Comput. Mol. Sci*., 2012, **2**, 73–78.

57 B. O. Roos, R. Lindh, P.-Å Malmqvist, V. Veryazov and P.-O. Widmark, *J. Phys. Chem. A*, 2004, **108**, 2851–2858.

58 B. O. Roos, R. Lindh, P.-Å. Malmqvist, V. Veryazov, P.-O. Widmark and A. C. Borin, *J. Phys. Chem. A*, 2008, **112**, 11431–11435.

59 W. Kutzelnigg and W. Liu, *J. Chem. Phys.*, 2005, **123**, 241102.

60 D. Peng and M. Reiher, *Theor. Chem. Acc.*, 2012, **131**, 1081.

61 M. Filatov, *J. Chem. Phys.*, 2006, **125**, 107101.

62 P. Å. Malmqvist, B. O. Roos and B. Schimmelpfennig, *Chem. Phys. Lett.*, 2002, **357**, 230–240.

63 L. Ungur and L. F. Chibotaru, *Chem. - A Eur. J.*, 2017, **23**, 3708–3718.

64 L. Ungur, M. Thewissen, J.-P. Costes, W. Wernsdorfer and L. F. Chibotaru, *Inorg. Chem.*, 2013, **52**, 6328–6337.

65 L. F. Chibotaru and L. Ungur, *J. Chem. Phys.*, 2012, **137**, 064112.

66 L. F. Chibotaru, L. Ungur and A. Soncini, *Angew. Chemie Int. Ed.*, 2008, **47**, 4126–4129.

67 L. Ungur, W. Van den Heuvel and L. F. Chibotaru, *New J. Chem.*, 2009, **33**, 1224.

Chapter 5

Magnetic exchange coupling in lanthanide cubane complexes with peripheral tetrazine-based radical

5.1. Abstract

Polymetallic complexes incorporating radical-bridging ligands are interesting for fundamental studies and magnetic applications, but their synthesis often requires strong reducing agents and stringent air and moisture-free conditions. In this chapter, three new air-stable polymetallic lanthanide cubanes $[Ln_4(\mu_3\text{-}OH)_4(bpytz^{\bullet-})_2(OAc)_2(acac)_4]\cdot n$THF (Ln = Gd, n = 1 (**1**), Dy, n = 1 (**2**) and Lu, n = 0 (**3**) are presented. The complexes were isolated in good yields through bench-top synthesis without the use of reducing agent. Analysis performed using single crystal EPR, microSQUID and theoretical calculations were employed to probe the presence of the reduced tetrazine radical, quantify the magnetic exchange coupling between the paramagnetic units (radical-radical, radical-metal and metal-metal) and to verify spin canting. The results of this work were presented at 100th Canadian Society for Chemistry (CSC): Lemes, M. A.; Frost, J.; Pialat, A.; Vieru, V.; Gabidullin, B.; Lan, Y.; Iwahara, N.; Kobera, L.; Komijani, D.; Bryce, D.; Hill, S.; Wernsdorfer, W.; Chiboratu, L. F. and Murugesu, M.

5.2. Introduction

The development of polymetallic lanthanide complexes bridged by radical ligands has attracted significant attention in the field of molecular magnetism.[1] A major goal in the development of new single-molecule magnets (SMMs) is designing systems with large anisotropic energy barriers to the reversal of magnetization (U_{eff}), with minimal through-barrier relaxation. SMMs have garnered much attention over the past two decades due to the desire to understand the fundamental processes behind their magnetic relaxation, and the potential for applications in high-density information storage and quantum computing.[2] The Evans and Long groups previously demonstrated that incorporating a radical-bridging

motif into a polymetallic lanthanide system significantly improves the magnetic properties, with the highest reported hysteresis temperature at the time of T_B = 13.9K.[3,4]

This increased magnetic performance is thought to originate from the radical ligands' diffuse orbitals, which can penetrate the lanthanide centres' buried 4*f* orbitals and inhibit quantum tunneling relaxation pathways.[1] However, these systems are generally synthesized using strong reducing agents such as cobaltocene (Cp_2Co) or potassium graphite (KC_8) under inert atmospheres, and the resultant complexes are often air and moisture sensitive. Their poor stability hinders the investigation of these systems and limits their potential applications.

In fact, lanthanide single-ion magnets and dinuclear radical-bridged have been attracted more attention in molecular magnetism community than polymetallic complexes (nuclearity > 2).[5] Those systems represent the ideal model to understand and also to fine-tune the magnetic properties. However, the approach that is a tackle in here is that the progresses in this field will inevitable focus on strategies to design and synthesize polymetallic systems containing radical-bridging lanthanides.

In developing air-stable radical-bridged polymetallic SMMs, our group has demonstrated the potential of systems based on the 1,2,4,5-tetrazine motif.[6,7] The tetrazine ring acts as an electron reservoir, and substitution at the 3 and 6 positions allows the steric and electronic properties to controlled. Moreover, reduced tetrazine-based ligands have been demonstrated to mediate strong exchange coupling in transition metal complexes. [8]

Despite this potential, the tetrazine system has been underused in coordination chemistry, with few examples of polymetallic complexes seen in literature. Kaim and co-workers explored the redox properties of such frameworks 30 years ago, aiming to synthesize complexes containing electron-rich transition metals such as Ru(II), Au(III), Cu(I), and Cu(II).[6] They demonstrated that the low-lying π^* LUMO in the tetrazine core facilitates the facile ligand reduction, and successive reductions and ring-opening reactions are challenging to predict or control. Our group have reported similar ring-opening reactions when investigating the coordination of Fe(III) and Hg(II) with tetrazines.[7b,c] To explain why some reactions resulted in a radical-tetrazine and others a ring-opened ligand, we investigated the effects of solvent on the resultant complexes. We demonstrated that reactions carried out in protic solvents tend to collaborate in isolating complexes with ring-

opening, whereas reactions in aprotic solvents give the unopened radical tetrazine ligand.[7,9-13] Furthermore, we have demonstrated that the choice of co-ligands also contributes to the electronic structure of the resultant tetrazine-based complexes.[7d]

Therefore, in this chapter magnetic characterization of a new series of discrete air stable lanthanide cubane containing reduced tetrazine-based ligand is described. The complexes were isolated and the general formula $[Ln^{III}_4(\mu_3\text{-}OH)_4(bpytz^{\bullet-})_2(OAc)_2(acac)_4]\cdot n$THF (Ln = Gd, n = 1 (**1**), Dy, n = 1 (**2**) and Lu, n = 0 (**3**), $bpytz^{\bullet-}$ = radical ligand form of 3,6-bis(3,5-dimethylpyrazol-1-yl)-1,2,4,5-tetrazine) was obtained through crystallographic analysis. The air-stable complexes were obtained in good yield and prepared under aerobic conditions without previous treatment of starting materials or employing a reducing agent. The magnetic characterization results consist of measurements from micro-SQUID to probe single-molecule magnetic properties in **2**, confirm spin canting, and investigate the nature and the strength of the magnetic exchange coupling in these systems. Finally, to support the experimental findings, computational methods such as DFT (Density functional theory) were performed to confirm the magnitude and behavior of the $bpytz^{\bullet-}$-$bpytz^{\bullet-}$ interactions in **3,** and fitting of the magnetic susceptibility data using a simplified spin-Hamiltonian was carried out to evaluate the Gd-Gd and Gd-$bpytz^{\bullet-}$ magnetic coupling.

5.3. Experimental

Materials

All manipulations were carried out under ambient conditions. Chemicals were purchased from TCI, Alfa Aesar, and Stream Chemicals, and used without further purification. The ligand was prepared according to a procedure and exhibit spectral data identical to a previous report.[14]

$[Gd_4(\mu_3\text{-}OH)_4(bpytz^{\bullet-})_2(OAc)_2(acac)_4]\cdot$THF (1):

$Gd(acac)_3\cdot x H_2O$ (0.50 mmol, 227 mg) and $Gd(OAc)_3\cdot x H_2O$ (0.25 mmol, 83.5 mg) were combined in a mixture of CH_2Cl_2/THF (1:1, 5 mL) and added to a solution of bpytz in 5 ml CH_2Cl_2 (0.25 mmol, 68 mg). The suspension was stirred for a day, after which it

formed a clear-green solution. The solution was filtered and placed in an NMR tube and layering with hexanes. Dark green block-shaped crystals were obtained after a week at room temperature (73% yield) and analyzed with single-crystal X-ray diffraction (Figure 5.1). Selected IR for **1** (cm^{-1}): 3617. (w), 2925 (w), 1601 (m), 1567 (s), 1517 (s), 1390 (s), 1311 (m), 1262 (s), 1186 (w), 1116 (s), 1047 (w), 1014 (m), 984 (m), 920 (m), 854 (w), 774 (w), 758 (m), 642 (m), 615 (m). Elemental analysis expected: C 32.9%, H 3.80%, N 12.79%. Found: C 32.1%, H 3.74, N 12.56%.

[Dy_4(μ_3-OH)$_4$(bpytz$^{\bullet-}$)$_2$(OAc)$_2$(acac)$_4$]·THF (2) and [Lu_4(μ_3-OH)$_4$(bpytz$^{\bullet-}$)$_2$(OAc)$_2$(acac)$_4$] (3):

The synthesis of **2** follows the same general procedure as for 1, replacing $Gd(acac)_3.xH_2O$ and $Gd(OAc)_3.xH2O$ for their dysprosium equivalents.(Figure 5.2). Selected IR data for **2** (cm^{-1}): 3617.61 (w), 3184.41 (w), 1566.36 (s), 1518.60 (s), 1386.16 (s), 1262.89 (s), 1187.03 (w), 1119.26 (m), 1056.63 (w), 1013.70 (s), 984.43 (w), 951.37 (w), 921.63 (s), 764.61 (m), 679.61 (s), 642.24 (s), 613.97 (s). Elemental analysis expected: C 32.51%, H 3.75%, N 12.64%. Found: C 31.9%, H 3.68%, N 12.48% (Yield = 76%). Selected IR data for **3** (cm^{-1}): 3629.15 (w), 2926.91 (w), 1608.61 (m), 1569.23 (s), 1520.16 (s), 1397.05 (s), 1266.80 (s), 1187.78 (w), 1121.49 (s), 1064.16 (w), 1038.45 (w), 1016.21 (m), 984.50 (m), 922.96 (m), 856.97 (w), 813.68 (w), 775.81 (w), 707.98 (s), 674.93 (w), 645.46 (s), 617.49 (m), 536.95 (w). Elemental analysis expected: C 31.62%, H 3.65%, N 12.29%. Found: C 31.46%, H 3.56%, N 12.22% (Yield = 73 %).

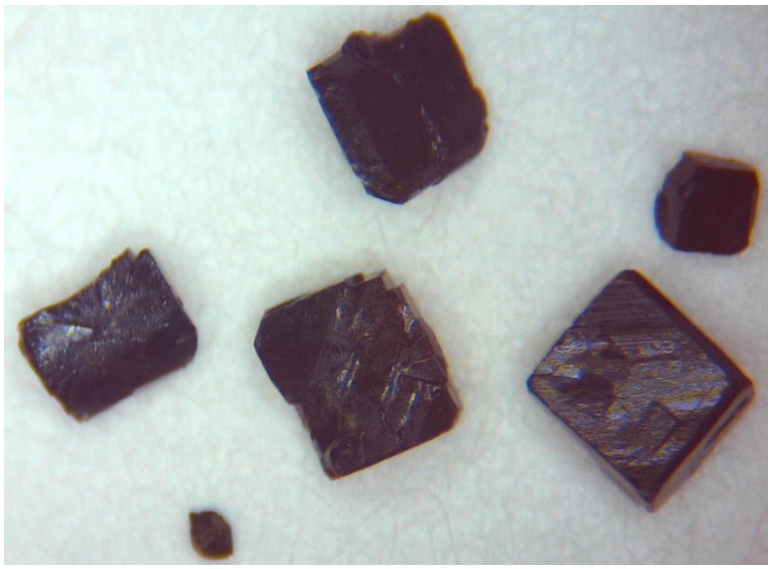

Figure 5.1. Single-crystals samples of **1.**

Single Crystal X-ray Crystallography

Suitable crystals were mounted on a glass fiber. A Bruker APEX-II CCD device was used to collect unit cell and intensity data using graphite Mo Kα radiation (λ = 0.71073). The data reduction included a correction for Lorentz and polarization effects, with an applied multiscan absorption correction (SADABS). The crystal structures were solved and refined using the SHELXTL v.6.12 program suite.[15] Direct methods yielded all non-hydrogen atoms, which were refined with anisotropic thermal parameters. All hydrogen atom positions were calculated geometrically and were riding on their respective atoms.

Elemental Analysis

Elemental analysis was carried out at Laboratoire d'analyse élémentaire de Université de Montréal.

Magnetic measurements

Variable temperature magnetic susceptibility and magnetization measurements were performed on a crushed polycrystalline sample of **1** - **3** using a Quantum Design MPMS-XL7 SQUID magnetometer equipped with a 7 T dc magnet, in the temperature range 1.8 - 300 K for dc applied fields up to 7 T. An *M vs*. *H* measurement was performed at 100 K to confirm the absence of ferromagnetic impurities. Diamagnetic corrections were applied to the sample holder and to the observed paramagnetic susceptibility of **1** - **3** using Pascal constants. Alternating current (ac) magnetic susceptibility measurements were performed under zero applied dc field and an oscillating ac field of 3.7 Oe and ac frequencies up to 1488 Hz. Diamagnetic corrections were applied to the observed paramagnetic susceptibilities using Pascals constants, with the diamagnetism of the sample holder and vacuum grease also corrected for. Variable temperature and variable sweep-rate single crystal hysteresis loop measurements were performed on **1** - **3** using a custom-built micro-SQUID apparatus operating down to 30 mK. The field is applied in any direction of the micro-SQUID plane with precision greater than 0.1° by separately driving three orthogonal coils.[16]

Single Crystal EPR Spectroscopy

Angle-dependent single crystal high-field EPR measurements were carried out using a cavity perturbation technique at a temperature of 1.7 K using a 9-5-1 T vector magnet. A millimeter-wave vector network analyzer was employed as a tunable microwave source and detector.[17] Dark green block crystals of **3** were washed by drops of ice cold MeOH to clean the surface from any possible paramagnetic impurities. Field-swept EPR spectra were recorded for different magnetic field orientations.

FTIR spectroscopy

Infrared spectra were recorded for solid-state samples on a Varian 640 FT-IR spectrometer in the 400 - 4000 cm^{-1} range.

Ab Initio Calculations

CASSCF Calculations were carried out on an isolated unit of **2** in MOLCAS 8.0. Two basis set approximations were employed. The active space comprised the nine electrons of Dy(III) in seven 4*f* orbitals, with the resulting 21 sextet, 128 quartet and 130 doublet states mixed by spin-orbit coupling within SO-RASSI. The SINGLE_ANISO program was then used to calculate the *g*-tensors, magnetic axes and local susceptibilities of the resulting spin-orbit multiplets.

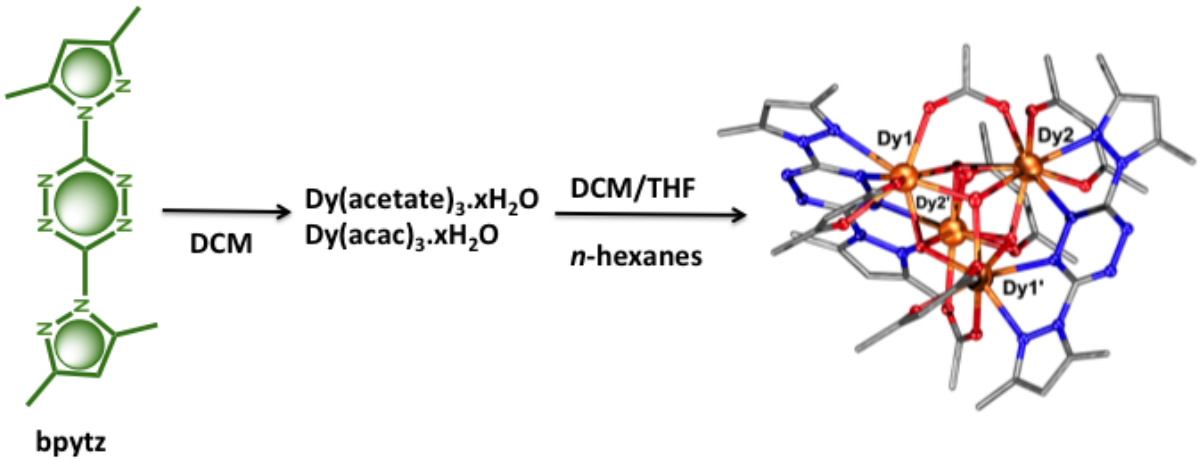

Figure 5.2. Reaction scheme for the synthesis of **2**. The same procedure is performed for **1** and **3**.

5.4. Results and discussion

Single-crystal X-ray studies revealed that **1** - **3** crystalize in the trigonal space group $R\bar{3}c$, in which the cubane core is formed by $[Dy_4(\mu_3\text{-}OH)_4]^{8+}$ (table 5.1). For the sake of simplicity only complex **2** will be fully described in this section (Figure 5.3). Because of the 2-fold axis in the centre of the cubane, the asymmetric unit of **2** is composed of two Dy(III) metal ions connected by two hydroxyl bridges and one reduced bpytz ligand. Additionally, two acetylacetonate and one terminally bound acetate co-ligands complete the asymmetric structure. The Dy-OH bond distances are in the range of 2.35 - 2.39 Å while the Dy-O-Dy angle is between 105.52 – 107.61°. Shape analysis reveals the coordination geometry of each Dy(III) metal ion is best described as biaugmented trigonal

prisms.[18] Close inspection of the packing arrangement reveals the closest intermolecular distance of ~ 9.3 Å (Dy…Dy) with non-covalent interactions being the dominant intermolecular contacts along of the crystal lattice (Figure 5.4).

Table 5.1. Crystallographic data of the complexes **1** - **3**.

	1	**2**	**3**
Formula	$C_{56}H_{82}Gd_4N_{16}O_{18}$	$C_{56}H_{82}Dy_4N_{16}O_{18}$	$C_{48}H_{66}Lu_4N_{16}O_{18}$
MW	1896.37	1917.38	1823.04
Temp. (K)	200(2)	200(2)	200(2)
Crystal system	trigonal	trigonal	trigonal
Space group	*R-3c*	*R-3c*	*R-3c*
a / Å	25.772(4)	25.7247(8)	25.6866(6)
b / Å	25.772(4)	25.7247(8)	25.6866(6)
c / Å	58.547(8)	58.0455(14)	57.5047(17)
α / °	90	90	90
β / °	90	90	90
γ / °	120	120	120
Vol / Å3	33676(10)	33266(3)	32858.5(18)
Z	18	18	18
D_c / mg m^3	1.683	1.723	1.658
μ / mm^{-1}	3.570	4.069	5.425
Reflections collected	132209	15769	188340
R1, wR2 (I > 2σ(I))	0.0433, 0.0712	0.0631, 0.1179	0.0518, 0.0650
Goodness-of-fit on F^2	1.070	1.120	1.085

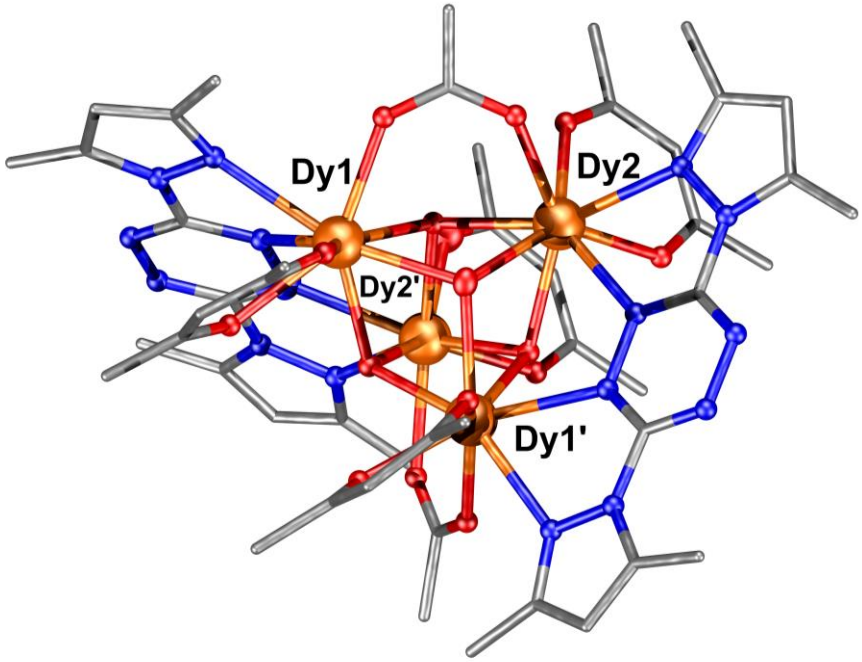

Figure 5.3. Molecular structure of complex **2**. Hydrogen atoms and solvent molecules were omitted for clarity. Color code: orange (Dy), red (O), blue (N), gray (C).

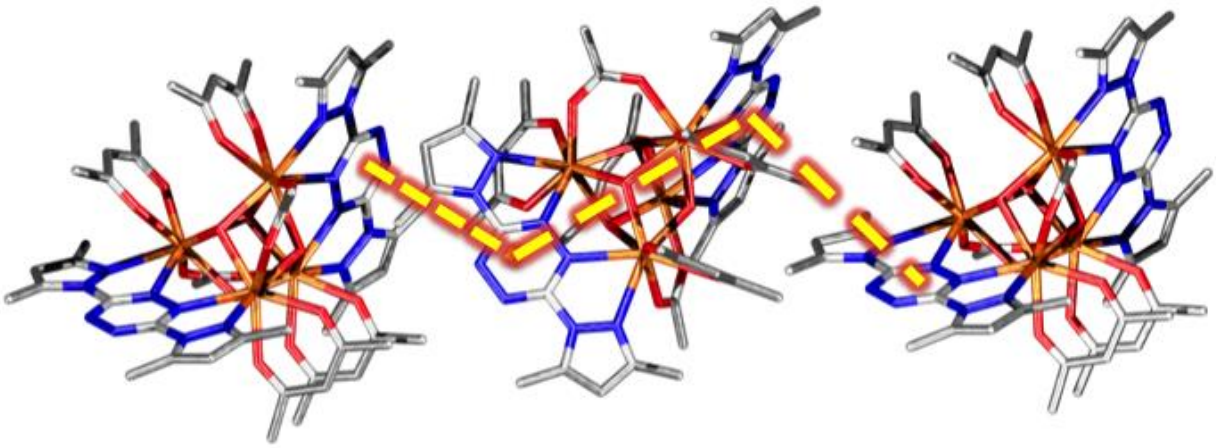

Figure 5.4. Closest distances between complexes **2**. The dashed lines highlight the shortest intramolecular distance between the reduced ligands (9.4 Å) and intermolecular distance (7.7 Å), while the intermolecular Dy…Dy is 9.3 Å. The same pattern is observed for **1** and **3**.

The reduction of bpytz ligands was evaluated through a combination of crystallographic analysis,[9e] charge balance and EPR studies. Table 5.2 summarizes the N-N and C-N bond distances of the tetrazine core in the free ligand and in **1**, **2** and **3**. The presence of the radical is supported by the crystallographic structural changes in the tetrazine core. The N-N elongation from 1.32 Å (free ligand) to 1.38 Å (complex) is strong evidence of tetrazine reduction.[9e] Single-crystal EPR measurements performed to corroborate the crystallographic analysis were carried out for **3**. The paramagnetic nature of the complex as a result of the presence of the radical was confirmed by the signal observed at g = 2.004 (Figure 5.5). Moreover, the weak angle-dependence observed is indicative of exchange interaction between the paramagnetic units, i.e., the reduced tetrazine.[19]

Overall, the observations confirm the reduction of the bpytz, however in terms of stability, attempts to perform solution-state NMR as well as Uv-vis spectroscopy were not successful, which lead us to believe that these compounds are not stable in solution. Nevertheless, the solid-state sample shows improved stability, as exposure to aerobic conditions and successive solid-state studies performed did not show any physical or chemical change in the crystalline sample.

Table 5.2. Comparison of bond distances (Å) in the tetrazine core of bpytz (free ligand) *vs.* bpytz in **1 (Gd), 2 (Dy)** and **3 (Lu)**.

	N-N	**C-N**	**C-N**
bpytz (free ligand)	1.324 (2)	1.330 (2)	1.340 (3)
	1.327 (2)	1.339 (3)	1.331 (2)
bpytz in **1**	1.387 (5)	1.311 (5)	1.308 (5)
	1.389 (4)	1.328 (5)	1.334 (4)
bpytz in **2**	1.386 (10)	1.304 (9)	1.314 (9)
	1.376 (7)	1.339 (8)	1.321 (8)
bpytz in **3**	1.396 (4)	1.312 (4)	1.314 (4)
	1.381 (3)	1.333 (4)	1.335 (3)

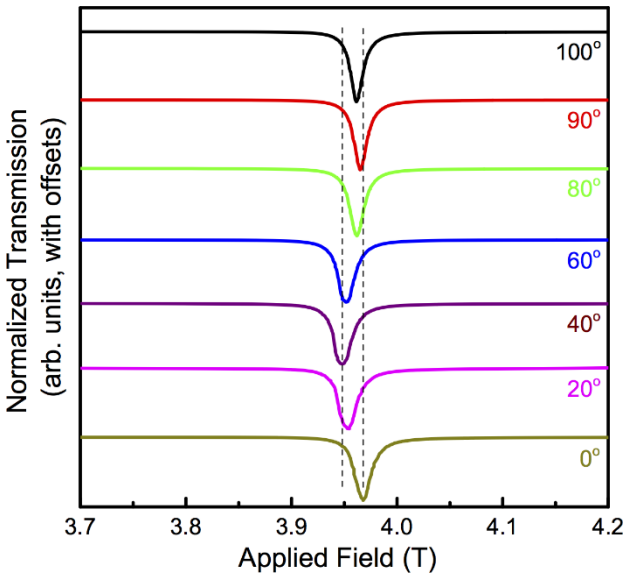

Figure 5.5. EPR spectra for complex **3** displaying peaks (center of the plot) that indicates paramagnetic signal originated from the reduced bpytz$^{\bullet-}$. The coordinates for these measurements are based on the laboratory references. The dashed lines indicate weak angle-dependence with *g*-value oscillating from 1.998(2) to 2.009(2). These results were obtained and plotted by Professor Stephen Hill.

In order to elucidate the magnetic properties of the complexes, direct current (dc) magnetic susceptibilities of **1** – **3** were measured between 1.9 -300 K under an applied dc field of 1000 Oe. The corresponding χT *vs.* T is presented in Figure 6. At 300 K the χT product of 57.17 cm^{3}Kmol^{-1} for **2** is in good agreement with the expected value of 57.41 cm^{3}Kmol^{-1} for four non-interacting Dy(III) ions (S = 5/2) and two bpytz$^{\bullet-}$ units (S = ½). Similarly, the room temperature χT product of **1** (32.09 cm^{3}Kmol^{-1}) and **3** (0.687 cm^3 K mol^{-1}) are in good agreement with the theoretical values (32.25 cm^3 K mol^{-1} and 0.75 cm^3 K mol^{-1}). In Figure 5.6, the curve of the magnetic susceptibility (χT) remains nearly constant between 300 K and 100 K for **1** and **2**. Below this temperature range a small decrease in the χT product is observed in both plots and can be attributed to thermal depopulation of the excited states. At very low temperatures (below 10 K), an upturn is observed followed by an abrupt decrease of χT. Such behavior has been previously observed in systems where metals ions are bridged by reduced ligands, and it has been attributed to high angular momentum in account of the presence of the radical.[1] The second

abrupt decrease of magnetic susceptibility suggests intra or inter antiferromagnetic interactions between the paramagnetic units and thermal depopulation of the crystal field excited states. For **3**, the magnetic susceptibility remains almost constant until 8 K, followed by a drop, which could be attributed to weak antiferromagnetic interaction between the reduced tetrazine ligands. To probe the nature and strength of the interactions between Ln – Ln and Ln- bpytz$^{\bullet-}$, the experimental χT product was fitted using the program *PHI*.[21] This calculation was performed using the isotropic Gd(III) analog (**1**), as the half-filled 4*f*-shell removes any orbital angular momentum contribution, allowing the magnetic exchange interaction between the paramagnetic units to be estimated. The best fit of **1**, using the 2 *J*s model, gives J_1 = -0.03 cm^{-1} and J_2 = -1.85 cm^{-1} (Scheme 5.1). Attempting to include a third *J* parameter does not add any meaningful results to the model.

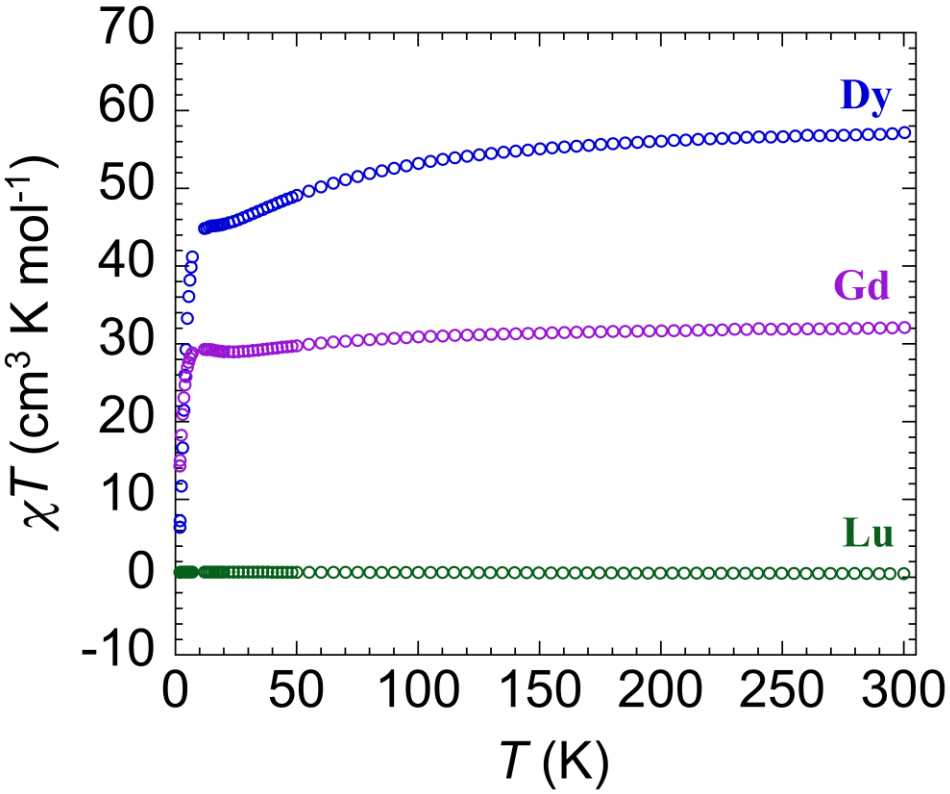

Figure 5.6. Variable-temperature dc magnetic susceptibility data, where $\chi = M/H$ normalized per mole, for **1** (purple), **2** (blue) and **3** (green) obtained under applied field of 1000 Oe and temperature from 300 to 1.8 K.

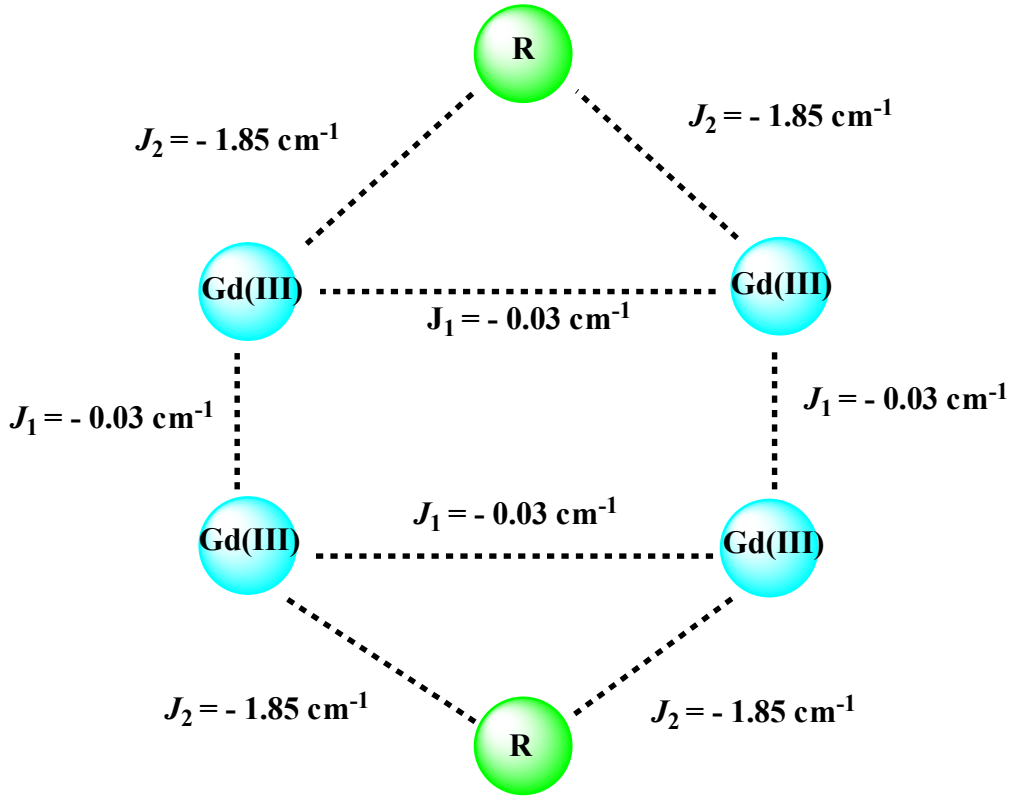

Scheme 5.1. Magnetic exchange coupling constants calculated for **1** using the appropriated spin-Hamiltonian: $\hat{H} = -2J_1(\widehat{Gd}_1.\widehat{Gd}_2 + \widehat{Gd}_1.\widehat{Gd}_3 + \widehat{Gd}_1.\widehat{Gd}_4 + \widehat{Gd}_2.\widehat{Gd}_3 + \widehat{Gd}_2.\widehat{Gd}_4 + \widehat{Gd}_3.\widehat{Gd}_4) - 2J_2(\widehat{Gd}_1.\hat{R}_1 + \widehat{Gd}_2.\hat{R}_1 + \widehat{Gd}_3.\hat{R}_2 + \widehat{Gd}_4.\hat{R}_2) + \sum_{i=1-6}\{\mu_B g\vec{B}.\hat{S}_i\}$. The dashed lines indicate the pathway for the magnetic communication. Color code: Radical ligand bpytz$^{\bullet-}$ (green).

Field dependence of magnetization, *M*, measurements for **1** and **2** performed under applied field up to 7 T display the anisotropic nature of the Dy(III) metal ions (Figure 5.7 and 5.8). After a rapid increase of the magnetic field at low magnitudes, the magnetization also increases linearly without saturation in **2**. Additionally, the non-superimposition of the isotherms in the *M vs.* HT^{-1} curves is also strong evidence of magnetic anisotropy. (Figure 5.8)

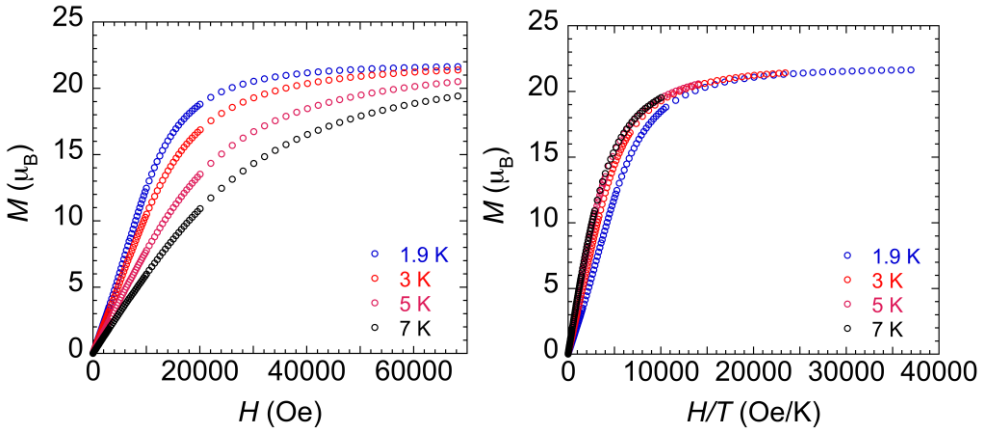

Figure 5.7. Field dependence of magnetization plots of **1** performed at different temperatures of 1.9, 3, 5 and 7 k.

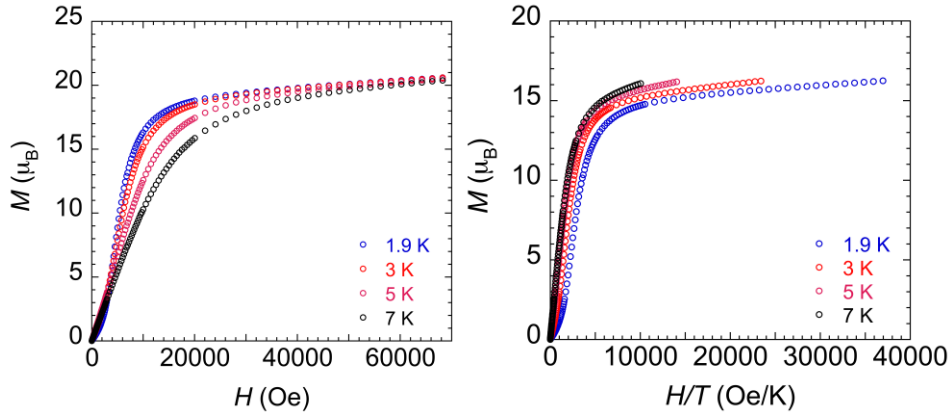

Figure 5.8. Field dependence of magnetization plots of **2** performed at different temperatures of 1.9, 3, 5 and 7 k.

Alternating current (ac) susceptibility measurements were performed for **2** in order to verify single-molecule magnet behavior (Figure 5.9). Unfortunately, the frequency dependency of the ac susceptibility results obtained under zero applied dc field display lack information to assign SMM behavior to complex **2**. The data shows a broad peak at low frequency and a shoulder at high frequency for measurements performed at low temperatures (1.9 - 2.1 K). Such observations indicate the presence of two relaxation processes, which could be attributed to the two sets of symmetry-equivalent metal centers in the cubane core. Attempts to fit the out-of-phase (χ'') component results in unrealistic

values to the energy barrier (U_{eff}) and relaxation time (τ) that can be explained by the lack of frequency dependence of the ac susceptibility as observed in Figure 5.9.

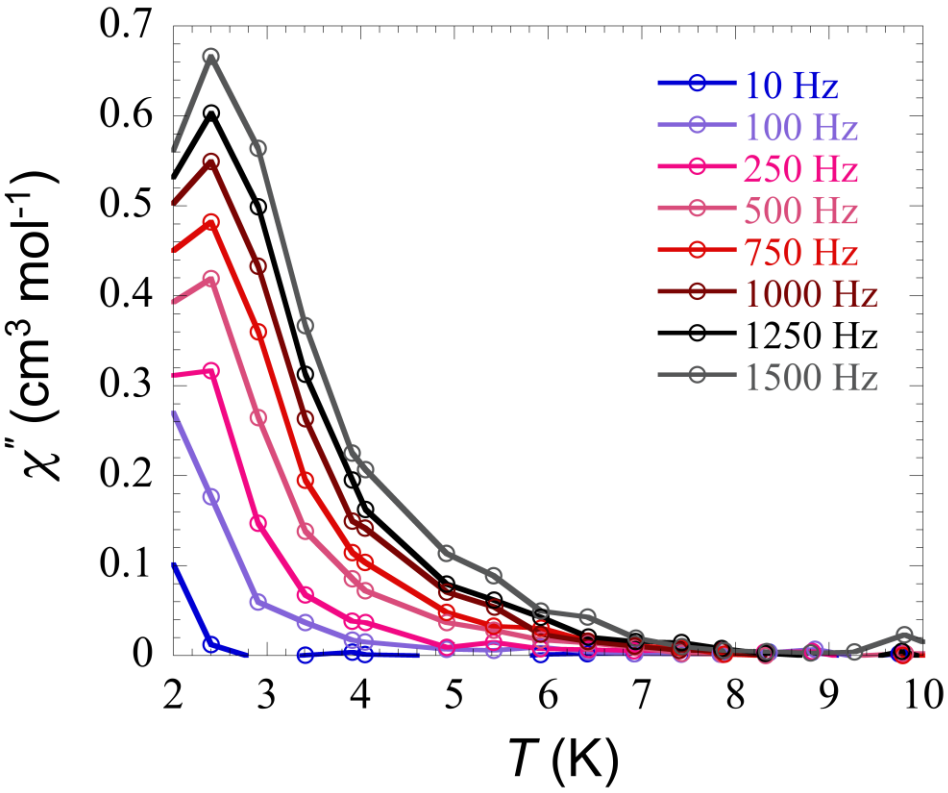

Figure 5.9. ac susceptibility (χ'') *vs*. Temperature plotted at different frequencies (ν)

In order to give more insight into the magnetic properties of this cubane system, hysteresis loop measurements were performed in a micro-SQUID apparatus in single crystals samples of **1** - **3** between 0.03-5 K (Figure 5.10 – 5.14). The results indicate the spin of the metal centers in **1** and **2** are tilted with respect to each other, i.e. they are canted. Consequently, a magnetic field cannot be applied along the main easy axis. To solve this problem, a transverse-field method was performed in order to detect the average antiferromagnetic and ferromagnetic projection between the spins.[22] Hysteresis loop measurements were carried out by applying a magnetic field along the two projections in **1** and **2**. The results presented in Figure 5.11 show that for both complexes a step-like loop is evident in all plots. Such behavior is attributed to the fast relaxation of magnetization or

quantum tunneling. SMM behavior was confirmed in **2**, as the hysteresis loops display temperature and sweep-rate dependence in the temperature range 1.6 – 0.03 K. The opening of the coercive field with the lowering of the temperature nearly to zero field is characteristic of the SMM system containing Dy(III) metal ions.[23] In this case parameters such as U_{eff} and τ can be extracted by the decay measurements of magnetization in the temperature from 1.3 to 0.03 K (Figure 5.12 and 5.13). Fitting the magnetization plot using the Arrhenius equation results in the following set of parameters: $U_{eff}/k_B \approx 12.4$ K (8.6 cm^{-1}) and $\tau_0 \approx 1.3 \times 10^{-6}$ s (ferromagnetic projection) and $U_{eff}/k_B \approx 9.8$ K (6.8 cm^{-1}) and $\tau_0 \approx 2.7 \times 10^{-5}$ s for (antiferromagnetic projection). The set of data obtained for the antiferromagnetic projection indicates the relaxation time is below that expected for SMMs, in which τ_0 usually ranges from $10^{-6} – 10^{-9}$.[24] Hysteresis loops for the Lu(III) analog (Figure 5.14), displays S-like behavior, which suggests weak antiferromagnetic interaction between the two reduced $bpytz^{\bullet-}$ ligands (S = ½) which is confirmed by fitting the data using a -2*J* Hamiltonian (g = ½ and S = ½) that gives J = - 0.177 cm^{-1}. Based on crystallographic observations, it is difficult to assign the origin of this exchange (intramolecular or intermolecular). A close inspection of the packing arrangement shows the closest distance between the two-tetrazine cores of 7.68 Å, while the intramolecular is 9.20 Å. Such observation is also true for **1** and **2**. In order to elucidate this, calculations using the Broken-symmetry (BS-DFT) method were employed on a discrete molecule of **3**. [25] The results obtained employing Yamaguchi's formula gives J = + 0.29 cm^{-1} for an intramolecular interaction (radical-radical).[26] Thus, a combination of the aforementioned results along with the hysteresis loop indicates that intra- and intermolecular magnetic communication is operational in complex **3**. Despite the limitation of DFT calculations to precisely estimate the nature of the magnetic exchange coupling in these systems,[27] the findings here indicate the coupling between the reduced bpytz ligands is weak, and thus, any magnetic contribution will be only observed at extremely low temperatures.

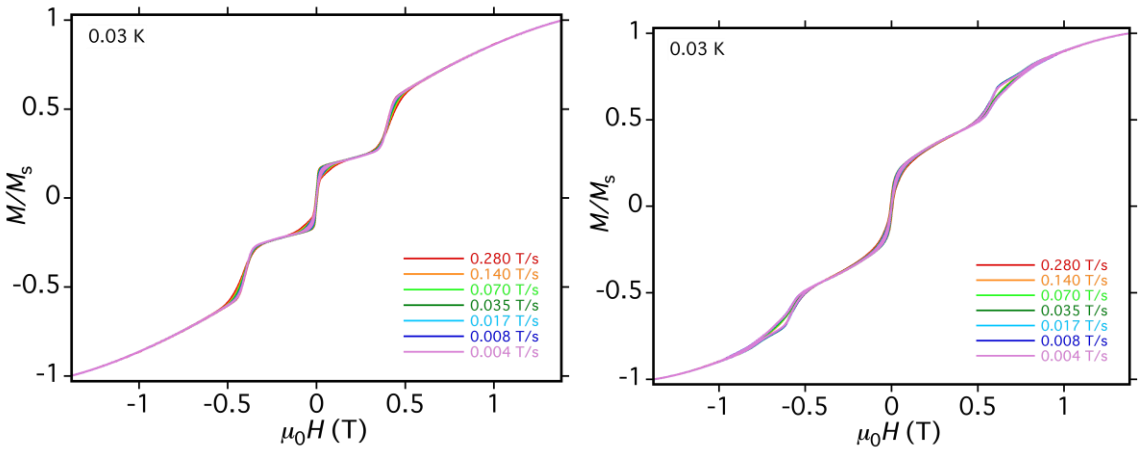

Figure 5.10. Hysteresis loop of **1** measured with magnetic field applied along of the ferromagnetic projection (left) and along of the antiferromagnetic projection (right). These results were obtained and plotted by Professor Wolfgang Wernsdorfer.

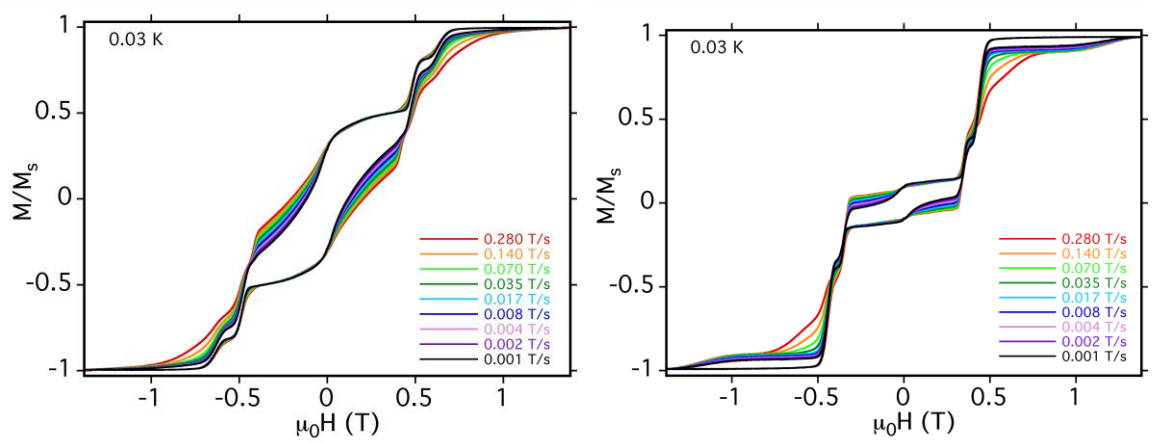

Figure 5.11. Hysteresis loop of **2** measured with magnetic field applied along of the ferromagnetic projection (left) and along of the antiferromagnetic projection (right). These results were obtained and plotted by Professor Wolfgang Wernsdorfer.

The observed spin canting in the complexes is relatively rare for discrete polymetallic systems[28] and only occurs under certain conditions, such as weak antiferromagnetic interactions or specific symmetries (absence of inversion center).[29] In the case of the cubane core of **1** and **2**, the 2-fold axis is placed in the center of the core and

no inversion center is operational in that system. These crystallographic observations validate the observed spin-canting in the experimental micro-SQUID measurements.

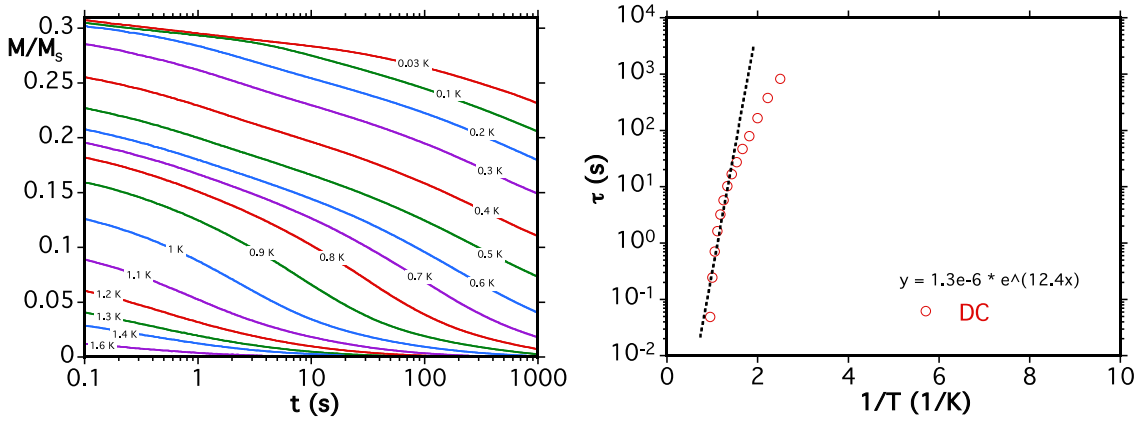

Figure 5.12. Magnetization decay measurements for complex **2** measured at different temperatures (left) and the relaxation time obtained from Arrhenius equation (right). For these measurements the magnetic field is applied along the average ferromagnetic projection. These results were obtained and plotted by Professor Wolfgang Wernsdorfer.

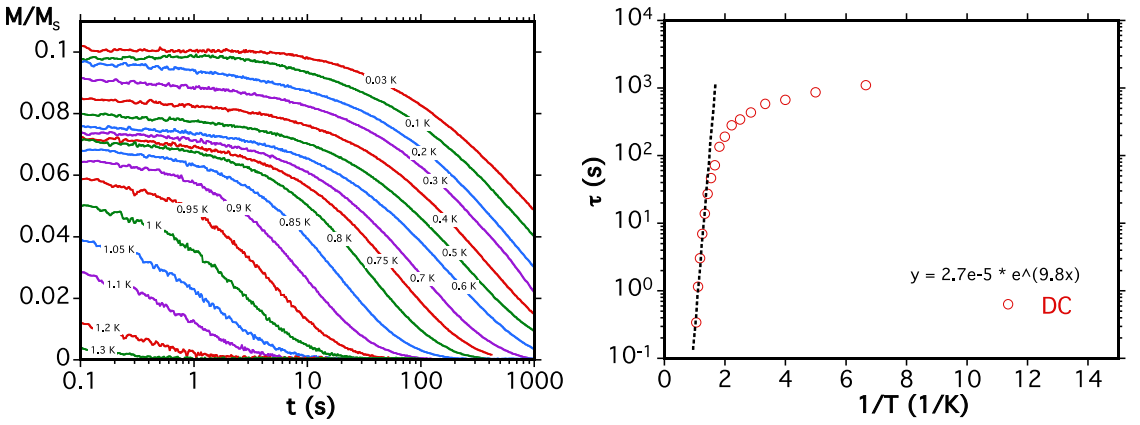

Figure 5.13. Magnetization decay measurements for complex **2** measured at different temperatures (left) and the relaxation time obtained from Arrhenius equation (right). For this measurement, the magnetic field is applied along the average antiferromagnetic projection. These results were obtained and plotted by Professor Wolfgang Wernsdorfer.

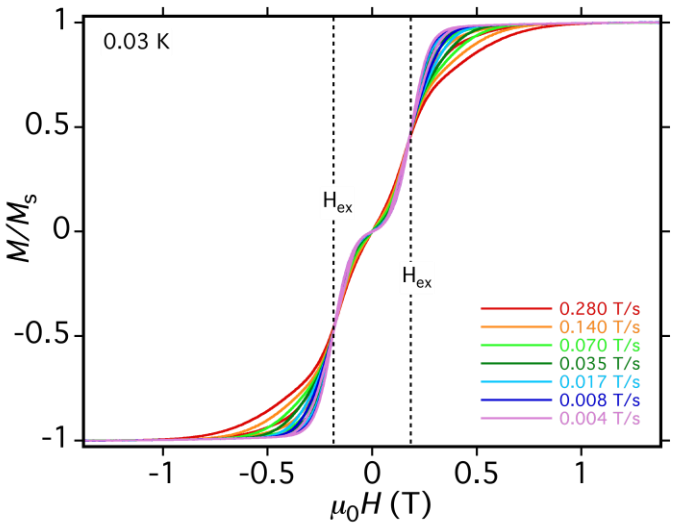

Figure 5.14. Hysteresis plot of magnetization (M) *vs*. field (H). The double S-shape loops indicate the antiferromagnetic interactions. The exchange field (H_{ex}) is located at approximately - 0.19, and 0.19 T, respectively. The magnetic exchange coupling constant J is calculated to be -0.177 cm^{-1} using $H_{ex} = 2JS/g\mu_B$ with $g = 2$, $S = 1/2$. These results were obtained and plotted by Professor Wolfgang Wernsdorfer.

5.5. Conclusion

With the recent advances in molecular magnetism, strategies to design and synthesize polymetallic systems with strongly magnetically coupled spins will inevitably take place in the future. Employing radical-bridged metal ions is a powerful approach to develop materials with such properties. Despite radical-based complexes being traditionally synthesized under inert conditions, here we have demonstrated a bench-top approach to obtain air-stable radical-bridged lanthanides complexes without the use of reducing agents. The exchange interactions estimated in the gadolinium analog (**1**) were relatively weak ($J_{bpytz^{\bullet}\text{--}Gd}$ = -1.85 cm^{-1} compared with the 26 cm^{-1} from Long *et al*[3]) and the energy barrier for **2** was small (U_{eff} = 8.6 cm^{-1} for the ferromagnetic and 6.8 cm^{-1} antiferromagnetic projection), but the novel approach and the studies performed are useful for the preparation of discrete polymetallic radical-bridged ligand complexes and microscopic investigation of multimetallic centers. Future work will focus on crystallizing compound **2** in different solvents to decrease the number of molecules in the unit cell (z parameter lower than 18), use a computational approach to evaluate the magnitude and nature of the $bpytz^{\bullet-}$-Dy and Dy-Dy interaction, and explain the step-like loop observed in the hysteresis plots.

References

1 Demir, S.; Jeon, I.-R.; Long, J. R.; Harris, T. D. *Coord. Chem. Rev.* 2015, 149.

2 Bogani, L.; Wernsdorfer, W. *Nat. Mat.* 2008, **7**, 179.

3 Rinehart, J. D.; Fang, M.; Evans, W. J.; Long, J. R. *J. Am. Chem. Soc.* 2011, **133**, 14236.

4 (a) Lees, A. M. J.; Platt, A. W. G. *Polyhedron* 2014, **67**, 368. (b) Chen, Y.-C.; Liu, J.L.; Ungur, L.; Liu, J.; Li, Q.-W.; Wang, L.-F.; Ni, Z.P.; Chibotaru-, L. F.; Chen, X.-M.; Tong, M.-L. *J. Am. Chem. Soc*. 2016, **138,** 2829.

5 (a) Woodruff, D. N.; Winpenny, E. P.; Layfield, R. A. *Chem. Rev.* 2013, **113**, 5110. (b) G. A. Craig, Murrie, M. *Chem. Soc. Rev*. 2015, **44**, 2135. (c) Gómez-Coca, S.; Aravena, D.; Morales, R.; Ruiz, E. *Coord. Chem. Rev*. 2015, **290**, 379. (d) Frost, J. M.; Harriman, K. L. M.; Murugesu, M. *Chem. Sci*. 2016, **7**, 2470.

6 (a) Kaim, W. *Coord. Chem. Rev*. **2002**, *230*, 127. (b) Clavier, G.; Audebert, P. *Chem. Rev*. **2010**, *110*, 3299. (c) Kaim, W.; Fees, J. *Z. Naturforsch*. 1995, **50b**, 123.

7 (a) Safin, D.; Pialat, A.; Leitch, A. A.; Tumanov, N. A.; Korobkov, I.; Filinchuk, Y.; Brusso, J. L.; Murugesu, M. *Chem. Commun.* 2015, **51**, 9547. (b) Lemes, M. A.; Pialat, A.; Steinmann, S. N.; Korobkov, I.; Michel. C.; Murugesu, M. *Polyhedron* 2015, **108**, 163. (c) Lemes, M. A.; Stein, H. N.; Gabidullin, B.; Steinmann, S. N.; Murugesu, M. *ACS Omega*, 2018, 3, 10273. (d) M. A. Lemes, H. N. Stein, B. Gabidulin, K. Robeyns, R. Clerac, M. Murugesu, *Chem. Eur. J*. 2018, **24**, 4259.

8 Woods, T. J.; Ballesteros-Rivas, M. F.; Ostrovsky, S. M.; Palii, A. V.; Reu, O. S.; Klokishner, S. I.; Dunbar, K. R. *Chem. Eur. J.* 2015, **21**, 10302.

9 (a) Kohlmann, S.; Ernst, S.; Kaim, W. *Angew. Chem. Int. Ed*. 1985, **24**, 684. (b) Kohlmann, S.; Kasack, V.; Roth, E.; Kaim, W. *J. Chem. Soc. Faraday Trans. 1* **1989**, *85*, 4047. (c) Kaim, W.; Kohlmann, S. *Inorg. Chem.* 1990, **29**, 1898. (d) Withersby, M. A.; Blake, A. J.; Champness, N. R.; Cooke, P. A.; Hubberstey, P.; Li, W.-S.; Schröder, M. *Inorg. Chem*. 1999, **38**, 2259. (e) Glöckle, M.; Hübler, K.; Kümmerer, H.-J.; Denninger, G.; Kaim, W. *Inorg. Chem*. 2001, **40**, 2263.

10 Dogan, A.; Schwederski, B.; Schleid, T.; Lissner, F.; Fiedler, J.; Kaim, W. *Inorg. Chem. Commun*. 2004, **7**, 220.

11 Panayiotidou, L.; Drouza, C.; Arabatzis, N.; Lianos, P.; Stathatos, E.; Viskadourakis, Z.; Giapintzakis, J.; Keramidas, A. D. *Polyhedron* 2013, **64**, 308.

12 Patra, S.; Miller, T. A.; Sarkar, B.; Niemeyer, M.; Ward, M. D.; Lahiri, G. K. *Inorg. Chem*. 2003, **42**, 4707.

13 Maji, S.; Sarkar, B.; Patra, S.; Fiedler, J.; Mobin, S. M.; Puranik, V. G.; Kaim, W.; Lahiri, G. K. *Inorg. Chem.* 2006, **45**, 1316.

14 Coburn, M. D.; Buntain, G. A.; Harris, B. W.; Hiskey, M. A.; Lee, K.-Y.; Ott, D. G. *J. Heterocyclic Chem*. 1991, **28**, 2049.

15 Sheldrick, G. M. *Acta Crystallogr.* 2008, **A64**, 112.

16 Wernsdorfer, W. *Supercond. Sci. Technol*. 2009, **22**, 064013.

17 (a) Mola, M.; Hill, S.; Goy, P.; Gross, M. *Rev. Sci. Inst.* 2000, **71**, 186. (b) Takahashi, S.; Hill, S. *Rev. Sci. Inst.* 2005, **76**, 023114.

18 Casanova, D.; Llunell, M.; Alemany, P.; Alvarez, S. *Chem. Eur. J.* 2005, **11**, 1479.

19 Winter, S. M.; Datta, S.; Hill, S.; Oakley, R. T. *J. Am. Chem. Soc.* 2011, **133**, 8126.

20 DeGayner, J. A.; Jeon, I.-R.; Harris, T. D. *Chem. Sci*. 2015, **6**, 6639.

21 Chilton, N. F.; Anderson, R. P.; Turner, L. D.; Soncini, A.; Murray, K. S. *J. Comput. Chem.* 2013, **34**, 2013.

22 Wernsdorfer, W.; Chakov, N. E.; Christou, C. *Phys. Rev. B.* 2004, 70, 132413.

23 (a) Li, M.; Ako, A. M.; Lan, Y.; Wernsdorfer, W.; Buth, G.; Anson, C. E.; Powell, A. K.; Wang, Z.; Gao, S. *Dalton Trans.* 2010, **39**, 3375. (b) Abbas, G.; La, Y.; Kostakis, G. E.; Wernsdorfer, W.; Anson, C. E.; Powell, A. K. *Inorg. Chem*. 2010, **49**, 8067.

24 (a) Aronica, C.; Pilet, G.; Chastanet, G.; Wernsdorfer, W.; Jacquot, J.-F.; Luneau, D. *Angew. Chem. Int. Ed*. 2006, **45**, 4659. (b) Lin, P.-H.; Burchell, T. J.; Ungur, L.; Chibotaru, L. F.; Wernsdorfer, W.; Murugesu, M. *Angew. Chem. Int. Ed*. 2009, **48**, 9489.

25 Neese, F. *Wiley Interdiscip. Rev.: Comput. Mol. Sci.* **2012**, *2,* 73.

26 Yamaguchi,K.; Takahara, Y.; Fueno, T. *In Applied Quantum Chemistry*; Smith, V. H., Jr., Schaefer, H. F., III, Morokuma, K., Eds.; Reidel: Boston, 1986, **155**.

27 (a) Brunold, T. C.; Tamura, N.; Kitajima, N.; Morooka-, Y.; Solomon, E. I. *J. Am. Chem. Soc.* 1998, **120**, 5674. (b) Binning Jr., R. C.; Bacelo, D. E. *J. Comput. Chem*. 2008, **29**, 716.

28 Gutschke, S. O. H.; Price, D. J.; Powell, A. K.; Wood, P. T. *Angew. Chem., Int. Ed.* 1999, **28**, 8.

29 Moriya, T. in Magnetism, Academic Press, London, 1963, **1**, 85.

Chapter 6

Conclusions

The field of molecular magnetism has shown tremendous advances towards the improvement of materials that behave as single-molecule magnets (SMM). The primary goal of this field it has been to bring to the real world SMMs that operate at reasonable temperatures or temperatures (blocking temperature T_B) in which the magnetic properties would be preserved in the electronic devices. In fact, the idea of applying such molecular magnets (monodomain) represent a potential approach to replace/improve the current systems, which utilize metal oxides that work as magnetic domains with millions of atoms to decode only single information. At early stages in this field, it was believed that the best strategy to achieve that it would be through the coupling of many paramagnetic metal ions aiming a large spin ground state. In other words, developing a polymetallic system in which at the low level of energy the ferromagnetic interactions would result in a large number of unpaired electrons that once magnetized would take a long time to the reversal of magnetization. After years following the spin ground state approach, it was realized by the molecular magnetism community that, in fact, local and global anisotropy play a significant role in the magnetic properties of polymetallic SMMs. Moreover, it was discovered that even if the system possesses large spin ground state, higher values of energy barrier and blocking temperature would not necessarily be achieved. In fact, this occurs because the interaction of many spins sites with different local symmetry diminishes the global anisotropy. Therefore, magnetic anisotropy and symmetry have become the focus in efforts to fine tuning SMMs properties.[1,2]

Recently, publications of Layfield and co-works[3] have demonstrated that unprecedented energy barrier and blocking temperature values for SMMs can be achieved by designing low coordinated and highly symmetrical lanthanide single-ion complexes. The strong and symmetrical crystal field interactions at the axial position of a single dysprosium metal ion contribute to the large anisotropy, which yields an extraordinary T_B of 80 K (slightly above the N_2 temperature). However, even though single-ion magnets show extraordinary anisotropy, the S = 5/2 spin ground state still not large enough

compared to those observed for polymetallic systems. In this way, there is a need in this field to reroute the focus towards developing new strategies to improve polymetallic SMMs targeting higher energy barriers and blocking temperatures. In this context, one approach that has been shown as a potential strategy to obtain high efficiently multinuclear SMMs is through radical-bridging metal ions. In terms of anisotropy, this approach is a powerful strategy to prevent or minimize mechanisms that contribute to the fast demagnetization of the spins. Such mechanisms known as quantum tunneling of the magnetization is responsible to diminish the energy barrier for the reversal of the spins. Thus, the strong direct electronic interaction provoked by the coupling of a radical and a metal ion can not only increase the energy for the time-reversal of the magnetic moment of the spins but also retain the magnetization at higher temperatures when compared to polymetallic systems containing diamagnetic ligands. In this way, tetrazine-based frameworks were employed in this project as non-innocent ligands aiming to design and synthesize radical-based complexes. As described early in this thesis, the electronic and structural properties of tetrazine-derived ligands shown to be suitable for the development of this project, in which the results were compiled in this thesis.

One of the most interesting point about the use of tetrazine-based ligands in this project was undoubtedly the versatility of the ligand. This has been highlighted in Chapter 2 and 3. In Chapter 2, the employment of the tetratopic bpymtz to template four metal ions strongly ferromagnetic coupled with a reduced tetrazine core results in a spin-ground state $S = 9/2$. Noteworthy, the reduction of the ligand was *in situ*, without any reducing agent. In this case, the large spin ground state observed does not reach the record of 83/2.[2] However, the presence of the radical with the interactions of the orthogonal magnetic orbital results in a maximum parallel alignment of the spins, which is unusual for polymetallic clusters.

The Chapter 3 describes the control of the bpytz ligand's oxidation state based on a careful selection of counter-ions. In this case, square radical-based complexes were isolated when reactions were performed utilizing carboxylate metal salts, while reactions with anionic BF_4^- metal salts result in complexes with diamagnetic bridging ligands. For that project, we investigated and probed the magnetic exchange interactions in such

architectures. Three analog square molecules were isolated with different electronic structures of their skeleton. Here, the role of the ligand was essential for the whole process of obtaining the desired molecules. At first, for the process of synthesizing complexes with specific geometry (square molecules). In this step, it was taking in account the fact that tetrazine-based frameworks allow extensive interactions (supramolecular interactions) with guest molecules which contribute to the self-assembly of the complexes in specific architecture.[6] Thus, diethyl ether and tetrafluoroborate were employed as guest molecules to template square architecture. Finally, the use of such non-innocence ligand was essential to isolated different paramagnetic square units in order to probe magnetic exchange coupling between M-M, M-R and R-R (M = metal, R = radical). In this case, the square molecules with magnetic coupling configuration of M-R (Co-bpytz$^{\bullet-}$), M-M (Co-Co) and R-R (bpytz$^{\bullet-}$-bpytz$^{\bullet-}$) were isolated based on the capability of bpytz to be reduced in the presence of specific counter-ions. The result of the dc susceptibility measurements combined with theoretical fit using the spin-Hamiltonian method were successful on elucidating the magnetic communication between the paramagnetic sites in each square molecule.

Designing a strategy to coordinate lanthanide ions with tetrazine-based ligands was another goal in this Ph.D. project. In fact, lanthanides are well known to be oxophilic, whereas the tetrazine-based frameworks contain no oxygen-donor. Therefore, the primary strategy to coordinate the *f*-elements with such N-rich ligand bpytz was by performing several amounts of reactions with different conditions looking for any pattern that could lead to a rational design to synthesize radical-bridged lanthanide complexes. The success of this approach is highlighted in Chapter 4 and 5. In Chapter 4, combining bulky auxiliary ligands, lanthanides metal ions and bpytz ligand was the key to obtain the dinuclear complexes. In this case, attempt to apply the same strategy described in Chapter 3, in order to obtain radical-bridged complexes, was not successful. To overcome this problem, the reducing agent cobaltacene ($CoCp_2$) was introduced to promote reduction in the ligand. Thus, a dinuclear complex with two reduced bpytz ligand making up a π-dimerization bridge was isolated. In this project, even though using bulky co-ligands as a strategy to obtain the desired dinuclear complexes was successful (such nuclearity represents a simple

model to understand the magnetic communication between lanthanides and highly delocalized radicals), such approach has demonstrated a drawback regarding magnetic properties. In fact, the low symmetry of the co-ligands results in the lowering of the axiality of the main magnetic axis of the complex, which ends up diminishing the efficiency of the system to hold the magnetization.

While laborious hours in the laboratory have shaped the strategies to obtain the compounds reported in this thesis, the methodology employed was kept intentionally simple. Besides the advantage of performing many series of reactions, this method contributes towards accelerating the process of obtaining radical-bridged metal ions targeting desired properties when compared with synthetic methods carried out under anaerobic atmosphere (Schlenk line or glove box). This process is highlighted in Chapter 5, which describes three novel polymetallic lanthanide complexes composed of a cubane-like core that is magnetically coupled with peripheral bpytz radical ligands. Investigations using EPR analysis and dc magnetic susceptibility performed in the Lu(III) complex have shown the presence of radical that was also confirmed by crystallographic studies. ac susceptibility was not able to verify SMM behavior in the Dy(III) complex and then being further probed by micro-SQUID measurements performed at temperatures below 1.9 K. An interesting point observed in this analysis was the confirmation that the spins were canted, and the hysteresis loop applied in the antiferromagnetic and ferromagnetic projection of the spins display step-like, which is associated to fast relaxation of the magnetization.

Although no unprecedented figure of merit, such as energy barrier, blocking temperature (U_{eff}, T_B; Currently record 2217 K and 80 K respectively[3]) or magnetic exchange coupling (J; Currently record: $J = 900$ cm^{-1} for transition metals[4] and $J = -27$ cm^{-1} for lanthanides[5]) were achieved, the results presented in this thesis have demonstrated and/or reinforced the versatility of tetrazine based ligands on designing strongly coupled magnetic systems. For future work, the optimization of the complexes reported in here will contribute to improve their magnetic properties and give more insights about the strategies to develop polymetallic systems with large magnetic anisotropy. Thus, instead of focus on

the reduction of tetrazine-based frameworks, the next step should tackle local symmetry in order to enhance global magnetic anisotropy. For this, some possibilities could be:

(1) Replacement of the transition metals in the coordination sites of the complex $[Ni^{II}_4(bpymtz^{\bullet-})Cl_6(DMF)_8]$ by lanthanides metal ions, and in the complexes of Chapter 3. Such modification would contribute to increase the local magnetic anisotropy and then potentially the SMM behavior can be observed.

(2) Employment of metal ions with low coordination and axial co-ligands. For example, cyclooctatetraene (COT) derivatives as auxiliary ligands. This approach could be useful to minimize the low symmetry presented in the complexes of Chapter 3.

(3) Recrystallize the lanthanide cubane complexes shown in Chapter 5, using different solvents in order to reduce the number of molecules in the unit cell. Such strategy would be helpful to an in-depth investigation of the magnetic properties observed experimentally. More precisely, to explain the step-like shape observed in the hysteresis loop by employing computational calculation in a few molecules instead of 18.

References

1 (a) R. Sessoli, D. Gatteschi, A. Caneschi, M. A Novak, *Nature*, 1993, **365**, 141. (b) R. Sessoli, H.-L. Tsai, A. R. Schake, S. Wang, J. B. Vicent, K. Folting, D. Gatteschi, G. Christou, D. N. Hendrickson, *J. Am. Chem. Soc.* 1993, **115**, 1804. (c) D. N. Woodruff, R. E. P. Winpenny, R. A. Layfield, *Chem. Rev*. 2013, **113**, 5110.

2 A. M. Ako, I. J. Hewitt, V. Mereacre, R. Clérac, W. Wernsdorfer, C. E. Anson, A. K. Powell, *Angew. Chem. Int. Ed*. 2006, **45**, 4926.

3 F.-S. Guo, B. M. Day, Y.-C. Chen, M.-L. Tong, A. Mansikkamäki, R. A. Layfield, *Science*, 2018, **362**, 1400.

4 I.-R. Jeon, J. G. Park, D. J. Xiao, T. D. Harris, *J. Am. Chem. Soc*. 2013, **135**, 16845.

5 J. D. Rinehart, M. Fang, W. J. Evans, J. R. Long, *J. Am. Chem. Soc.* 2011, **133**, 14236.

6 H. T. Chifotides, I. D. Giles, K. R. Dunbar, *J. Am. Chem. Soc.* 2013, **135**, 3039.